University of Huddersfield Repository

Li, Feng

Integrated tactile-optical coordinate measurement for the reverse engineering of complex geometry

Original Citation

Li, Feng (2014) Integrated tactile-optical coordinate measurement for the reverse engineering of complex geometry. Doctoral thesis, University of Huddersfield.

This version is available at http://eprints.hud.ac.uk/23725/

http://eprints.hud.ac.uk/

UNIVERSITY OF HUDDERSFIELD

Integrated Tactile-Optical Coordinate Measurement for the Reverse Engineering of Complex Geometry

by

FENG LI

A thesis submitted in partial fulfilment for the

degree of Doctor of Philosophy

in the

School of Computing and Engineering

Centre for Precision Technologies

November 2014

Copyright Statement

Abstract

Complex design specifications and tighter tolerances are increasingly required in modern engineering applications, either for functional or aesthetic demands. Multiple sensors are therefore exploited to achieve both holistic measurement information and improved reliability or reduced uncertainty of measurement data. Multi-sensor integration systems can combine data from several information sources (sensors) into a common representational format in order that the measurement evaluation can benefit from all available sensor information and data. This means a multi-sensor system is able to provide more efficient solutions and better performances than a single sensor based system. This thesis develops a compensation approach for reverse engineering applications based on the hybrid tactile-optical multi-sensor system.

In the multi-sensor integration system, each individual sensor should be configured to its optimum for satisfactory measurement results. All the data measured from different equipment have to be precisely integrated into a common coordinate system. To solve this problem, this thesis proposes an accurate and flexible method to unify the coordinates of optical and tactile sensors for reverse engineering. A sphere-plate artefact with nine spheres is created and a set of routines are developed for data integration of a multi-sensor system. Experimental results prove that this novel centroid approach is more accurate than the traditional method. Thus, data sampled by different measuring devices, irrespective of their location can be accurately unified.

This thesis describes a competitive integration for reverse engineering applications where the point cloud data scanned by the fast optical sensor is compensated and corrected by the slower, but more accurate tactile probe measurement to improve its overall accuracy. A new competitive approach for rapid and accurate reverse engineering of geometric features from multi-sensor systems based on a geometric algebra approach is proposed and a set of programs based on the MATLAB platform has been generated for the verification of the proposed method. After data fusion, the measurement efficiency is improved 90% in comparison to the tactile method and the accuracy of the reconstructed geometric model is improved from 45 micrometres to 7 micrometres in comparison to the optical method, which are validated by case study.

Acknowledgements

Contents

List of Figures

List of Tables

Abbreviations

B-Splines	Basis Splines
CAD	Computer-Aided Design
CAM	Computer-Aided Manufacturing
CCD	Charge-Coupled Device
CMM	Coordinate Measuring Machine
CNC	Computer Numerical Control
CT	Computed Tomography
DLP	Digital Light Processing
FE	Forward Engineering
FPP	Fringe Projection Profilometry
ICP	Iterative Closest Point
IGES	Initial Graphics Exchange Specification
ISO	International Standards Organisation
MPE_E	Maximum Permissible Error for Length Measurement
NURBS	Non Uniform Rational B-spline
PLM	Product Lifecycle Management
STEP	Standard for the Exchange of Product Model Data
STL	Stereo Lithography or Standard Triangulation Language
RMS	Root Mean Square
RMSR	Root Mean Square of Residuals
RP	Rapid Prototyping

Chapter 1

Introduction

1.1. Introduction

In many areas of industry, 3D point data measured from the surfaces of physical objects has been widely adopted in a variety of product development processes, such as product inspection, quality control, reverse engineering (RE), etc. In measurement applications, different sensing technologies are available for data acquisition, such as tactile probing, laser scanning, fringe projection, etc. It has been shown that each technique has its own characteristics and application. Complex design specifications and tighter tolerances are increasingly required in modern engineering applications, either for functional or aesthetic demands. The geometric specifications embedded in these parts such as shapes and surfaces, dimensions, geometrical tolerances, surface characteristics, surface material, etc. make it difficult to satisfy all the measurement requirements with only one single sensor in dimensional measurement. Multiple sensors are therefore exploited to achieve both holistic measurement information and improved reliability or reduced uncertainty of measurement data.

The basic motivation for multi-sensor data fusion is to improve the quality and usability of the measurement result, e.g. in a production process. Multi-sensor integration systems can combine data from several information sources (sensors) into a common representational format in order that the metrological evaluation can benefit from all available sensor information and data. This means a multi-sensor system is able to provide more efficient solutions and better performances than the single sensor based system. This additional metrological benefit may be termed multiple sensors synergy. Synergistic effects may improve the performance of a multi-sensor system in at least one of the following ways: increased spatial and temporal coverage and better resolution, increased robustness to sensor and algorithmic uncertainty, better noise suppression and improved accuracy [1]. Particular features of a workpiece can be measured with the most suitable sensor, and measurements with better accuracy can be used to correct data from other sensors which exhibit relevantly larger systematic errors but have a wider field of view or application range.

1.2. Motivation & scope

Traditionally, the development of industrial products begins with the goals expected of the product function. Design engineers conceptualise the components required in a product, and develop the product through the procedures of design, fabrication, inspection, and assembly. Each procedure requires detailed design drafts or process charts. Such a developing flow is called forward engineering (FE). In recent years, RE, the opposite of FE, has received increasing attention. Reverse engineering refers to the process of analysing the construction of

a product when there are no design documents available from its original production. RE serves many purposes including:

1)   Developing a similar or improved product/design.

2)   Creating adaptors or enclosures to the original product.

3)   Reproducing an existing part.

Existing tactile coordinate measuring machine (CMM) methods are widely used for industrial dimensional metrology [2], but the digitisation process on such systems is very time-consuming for the acquisition of the initial set of points on complex or freeform surfaces if applied to RE. Another disadvantage in the context of RE is that a predefined path must be specified in advance to cover all features of a workpiece that are to be probed. This requires a prior knowledge of the part, presenting an obstacle to future automatic RE strategies. An alternative approach is represented by non-contact digitisation of surfaces based on optical triangulation techniques [3]. Triangulation sensor usually can capture dense point clouds efficiently in terms of speed and required human intervention. Additionally, it offers the possibility of measuring surface points from multiple features via a single and relatively simple probing path. Therefore it has been widely used in RE applications and quality control methods of freeform surfaces. In general, optical methods are considered to be less accurate in comparison with tactile probing in measurements of geometric features [4].

To meet the requirement of both high speed and high accuracy 3D measurement for RE, multi-sensor measuring systems have been developed to measure, analyse and rebuild the CAD model of objects. Hybrid contact-optical coordinate measuring systems are each designed by Chan, et al. [5], Carbone, et al. [6], Shen, et al. [7] and Sladek, et al.[8] where the obtained information digitized by an optical sensor is used to guide the touch probe for re-measuring the sample surfaces. The presented systems are cooperative integrations where optical sensors acquire the global shape information of objects to guide the touch probes for automatic point sensing. They are, however, limited to dealing with workpieces with relatively simple features.

Therefore, this thesis aims at developing an effective competitive integration approach for the compensation of an optical scanner by using a tactile probe to perform the RE of complex shape parts. The part should have both common geometric features and freeform surface; it also has non-surface features, such as slots or holes. The work of this thesis mainly focuses on three aspects: multi-sensor system integration, geometric elements modelling and fitting, and fused data compensation.

In a multi-sensor integration system, each single sensor needs to be configured properly for satisfactory measurement results. The resolution, measuring ranges and working principles of the multiple sensors are usually different. Each individual sensor works in their own separate coordinate system, then all the data from different coordinate systems have to be precisely integrated into a common source.

An integrated multi-sensor system results in a variety of information and data. They require a unified and consistent data representation. Standard file formats provide an effective way to represent the data and exchanged with other systems in coordinate measurement. The parts measured by multi-sensor system usually comprise complex surfaces and features. Multi-sensor data fusion requires suitable methods and algorithms to process the multiple data acquired from different sensors. The methods in the RE of geometry include: data registration, polyhedral surface generation, shape recognition and segmentation and model reconstruction.

The discrete shapes should be best-fitted to different geometric elements based on mathematical and numerical principles. The integrated system accuracy and resolution depend on all separate systems, but should be biased towards the precise tactile method. A compensation approach for RE based on the multi-sensor integration system is developed in this thesis.

1.3. Aims & objectives

The aim of this thesis is to propose & validate the competitive integration of inhomogeneous sensors in the context of reverse engineering applications. The focus of this study is to compensate inaccuracies of the point cloud data using more accurate tactile probing. The measurement volume of workpiece discussed in this thesis ranges from 20 mm $\times$20 mm $\times$20 mm to 500 mm $\times$500 mm $\times$500 mm. The measurement speed of the hybrid system is expected to be similar to optical method and the accuracy is close to tactile system. The main objectives of the thesis are:

- A universal approach to unify tactile and optical sensors for the measurement of geometric features
- A workflow based on tactile-optical multi-sensor techniques for RE applications
- A set of algorithms for discrete geometry fitting and initial estimates
- A set of programs for geometric elements best-fit and compensation of point cloud data

- A fast and accurate method for RE of complex shape part based on a multi-sensor technique, which can take advantage of the fast speed of the optical sensor & high accuracy of the tactile probe

1.4. Outline

The thesis is organized as follows:

Chapter 2 describes three measuring techniques commonly used in dimensional measurement: tactile probing, laser scanning and fringe projection. Their working principle and mathematical model are discussed separately. The calibration method of each technique is also presented. The multi-sensor configurations and data fusion procedures, as well as the related works in multi-sensor integration for dimensional measurement are detailed.

Chapter 3 introduces a new approach, which is called the "centroid of spherical centres" method, for tactile-optical measuring system coordinate integration. The benefits of the proposed method are improved accuracy in coordinate unification, and the method is a universal approach to be used to integrate a CMM touch probe and optical sensors. An additional advantage of this method is that different measuring devices do not need to be placed in the same workplace.

Chapter 4 first describes the common data processing methods for RE applications. The workflow for RE mainly includes these operations: data pre-processing, data registration, meshing, shape recognition and segmentation, and model reconstruction. Then the least squares methods for best-fit geometric elements are presented. A synthesized initial estimation for nonlinear functions of the least squares algorithms is discussed. Finally a compensation method for hybrid tactile-optical system in RE application is proposed.

Chapter 5 first introduces the multi-sensor measuring platform and investigates the measurement errors of laser line scanning by using tactile probing as a reference. The feasibility and robustness of the proposed approach are also examined. Then a part with only geometric features is used to evaluate the method proposed in Chapter 4 after data segmentation. Then a detailed case study of RE of an industrial housing workpiece by using multi-sensor competitive approach is presented. The developed programs based on the Matlab platform are exploited to verify the proposed algorithms. Finally, the multi-sensor data compensation, the CAD model reconstruction process, the measurement speed using different methods and the accuracy evaluation of the studied workpiece are presented.

Chapter 6 summarizes the thesis with conclusions drawn from the study and propose some promising directions for the future research.

Chapter 2

Multi-sensor Integration in Dimensional Measurement

2.1. Introduction

Acquiring 3D point data from physical objects is increasingly being adopted in a variety of product development processes, such as quality control and inspection, reverse engineering and many other industrial fields. A variety of sensor technologies have been developed to meet the requirement of surface digitization with different accuracy and measuring ranges.

2.2. Sensor techniques for coordinate measurement

Different sensor technologies are developed for surface digitization in dimensional measurement. According to whether the probes or sensors contact the surface, the data acquisition methods can basically be divided into two categories: tactile measurement methods and non-contact measurement method [9]. Figure 2-1 gives an overview of the classification of some of the existing sensor techniques [10].
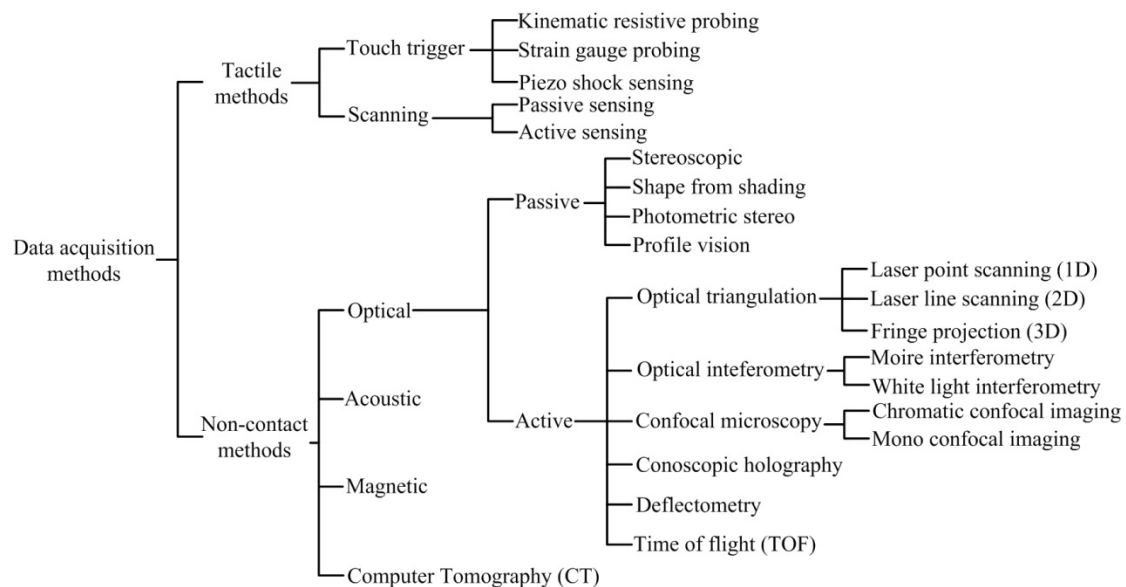
Figure 2-1: Existing sensor techniques for measurement

In this thesis, three data acquisition techniques are implemented in our experiments: tactile probing, laser line scanning and fringe projection. These techniques have been widely used in dimensional measurement, their typical resolution and measuring range plots are shown in Figure 2-2 [11]. Their working principles and calibrations are discussed in the following sections.

(a) Resolution   (b) Measuring range
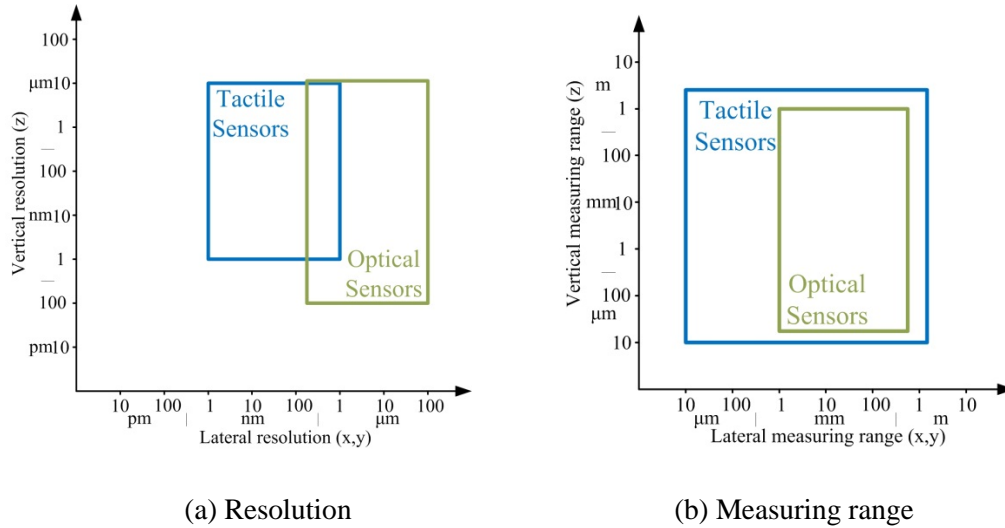
Figure 2-2: Typical resulition and measuring range plots for optical sensors and tactile probes in coordinate measuring systems

2.2.1. Tactile probing

2.2.1.1. Principle of the tactile probing system

Tactile probing systems are usually used in cases where surface measurements allow or require lower point data density, such as the inspection of prismatic objects, workpiece surfaces with a known CAD model or a shape without large variation. The measuring ranges span from sub-micrometre to several millimetres in one, two or three dimensions. In a special case, 2.5 dimensional probing systems are planar sensitive and have only limited sensitivity/measuring range perpendicular to this plane [11].

The tactile probing sensors are usually slower in acquiring points compared to optical sensors. Their contact working features make them unsuitable for measuring soft material objects. Other limitations of the probing systems are that surface zones might not be measured if the sizes of these regions are smaller than the diameter of the tip ball or peaks might lead to the smoothed approximation of the surface (Figure 2-3 (a)). Moreover, the different sizes of the stylus tips also influence the measurement results as shown in Figure 2-3 (b) [2]. However, the touch trigger probing systems are generally considered to show a higher accuracy in comparison to optical sensors [4]. They are simple, more adaptive to the environment and not sensitive to ambient light which greatly affect the accuracy of optical systems.

(a) Inaccessible regions   (b) Influence of the different tip sizes
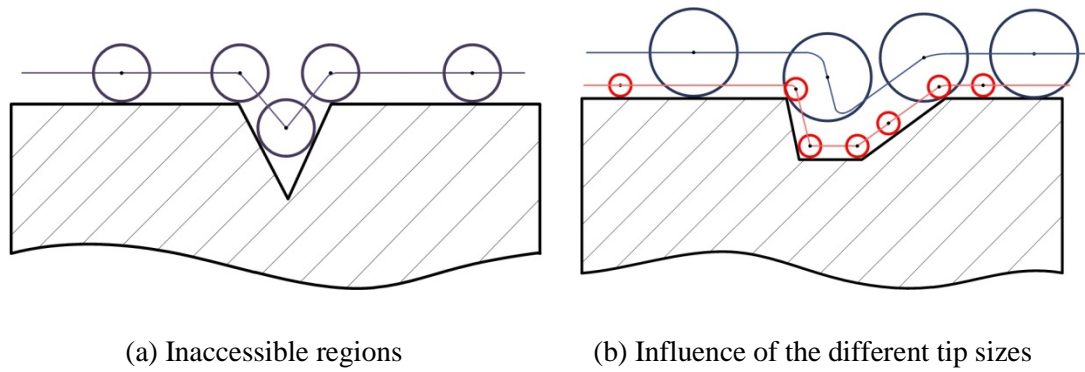
Figure 2-3: Limitations of the tactile probing system

The working principle of tactile probes is based on a mechanical interaction with the workpiece surface and they usually measure in more than one direction. There are two differentiated modes, touch trigger mode and scanning mode.

In the touch trigger mode, the data acquisition speed is usually slow (1~2 points/second). The probe mechanism generates a trigger signal with the help of information obtained by a displacement measuring system; the signal can be triggered when a certain threshold value is exceeded. Reaction force from the probing system to the CMM must be as low as possible [2]. However, if the triggering force is too low the false triggers will be detected due to inertia. The trigger signal generated by the probe in real time will be processed to record the position of the contact point. Therefore, the touch trigger probing process contains two basic steps. First a trigger signal is generated when a surface is touched by the moving tip. And then followed by a withdrawing procedure, the signal is generated again when the tip is back off the surface, the stylus returns to its previous position and is ready for next point probing. A disadvantage of this method is that it may take a long time as the process of approaching the surface and withdrawing has to be repeated for each point to be probed.

In scanning mode, the probe tip is always in contact with the surface during the scanning process. The touching element is guided on a line along the surface while a set of coordinates are sampled in a time sequence. The points acquired by scanning sensors (up to 500 points/second) are much more than the trigger sensors. However, as the stylus constantly and consistently contacts the work surface, their measurement uncertainty is higher than touch trigger probing because of dynamic measurement errors. The main difference between scanning and touch trigger probes is that scanning probes use electrical springs and small linear drives, which generate their probing force electronically instead of mechanically like touch trigger probes [12]. In general, the scanning sensors are more complex in structure, data analysis and monitor control than the touch trigger sensors. Accordingly, the scanning sensors are suitable to perform the measurement of size, position and profile of precise geometric

features, while the touch trigger sensors can be exploited for shapes without significant variations [10].

A limitation of tactile probing for RE is that prior knowledge of the part is required for efficient data capture. This is necessary to guide the probe to touch the surface. Without such knowledge, the probe must scan very slowly, even when not contact with the part, or else risk damage upon collision. Very few examples exist, such as Renishaw Cyclone scanning system that uses a 'raster scanning' method to digitize the surface, where this is not the case.

2.2.1.2. Modelling of the tactile probing system

Most frequently a tactile probing system is a 3D data acquisition system, which means that the initial acquired data are 3D in $(x,\ y,\ z)$ coordinates. The geometrical information of workpiece can be derived from this 3D data. Therefore, a tactile probing system has to have at least the following features to fulfil its requirements [2]:

- A contact element to establish an interaction with the surface (e.g. tip ball, disc or cone)
- A transmitting component to transfer information about the interaction from the contact element to the sensor (e.g. stylus shaft)
- A force generating element (suspension) to produce a defined probing force (e.g. spring)
- A sensor to sense the interaction between the contact element and the surface (e.g. electric switch)
- An output transmitting the information for triggering a length measuring device (e.g. scale) or for further processing (e.g. correction of bending, taking into account qualified tip ball radius, evaluation in instrument's software).

Most often, the functional characteristics of the probing systems can be derived from a Cartesian (most coordinate measuring machines), cylindrical, or a spherical coordinate system. The probing process requires the definition of the coordinate systems for data acquisition. Three coordinate systems are defined in a 3D tactile probing system as shown in Figure 2-4 [2].
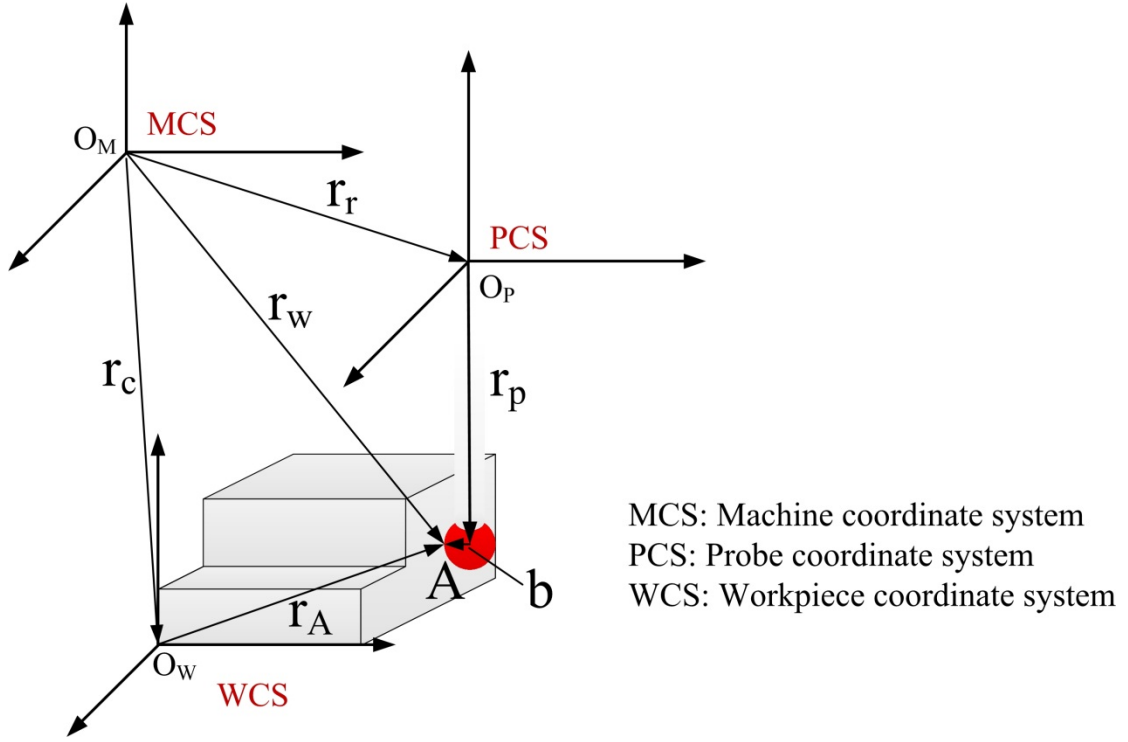
Figure 2-4: Probing system in coordinate measurement

Where $\vec{r_A}$ is the position vector of the actual contact point A in the workpiece coordinate system (WCS). $\vec{r_r}$ represents the position vector of the origin of the probe coordinate system (PCS) in the machine coordinate system (MCS). $\vec{r_C}$ stands for the position vector of the origin of the WCS in the MCS. $\vec{r_w}$ denotes the point vector of the contact point in MCS. $\vec{r_p}$ represents the position vector of the centre of the tip ball in the PCS. And $\vec{b}$ denotes the tip correction vector which starts from the centre of the tip to the contact point.

From the coordinate systems relationships described in Figure 2-4, the final result of $\vec{r_A}$ can be derived. $\vec{r_w}$ in the MCS and WCS is represented as:

$$\vec{r_w} = \vec{r_c} + \vec{r_A} \tag{2-1}$$

While $\vec{r_w}$ in the MCS and PCS can be represented as:

$$\vec{r_w} = \vec{r_r} + \vec{r_p} + \vec{b} \tag{2-2}$$

Then we can obtain the position vector of point A:

12

$$\vec{r_A} = \vec{r_r} + \vec{r_p} + \vec{b} - \vec{r_c} \qquad\qquad (2-3)$$

2.2.1.3. Calibration of the tactile probing system

In order to perform correct measurements, the position of the tip ball centre point related to the reference point of the probing system ($\vec{r_p}$ in Figure 2-4) and the radius of the tip ball (absolute value of $\vec{b}$ in Figure 2-4) must be known first [13]. This is the main purpose of a calibration process. There are many factors influencing these parameters, such as probing force (magnitude and direction), pre-travel of the probe, wear of tip ball, plastic deformation, elastic behaviour of probing system, styli, wear of workpiece surface, temperature and other influences [2].

The parameters can be determined experimentally with a calibrated artefact under the same conditions. This procedure is called probing system qualification. The most common used calibrated artefact is a sphere (diameter 10 mm to 50 mm). A sphere has the advantages that it is as very precise calibrated standard and can be positioned without regard to rotational position. Its surface has normal vectors in every spatial direction, therefore the correction of tip ball diameter can be independent of normal direction of surface [2]. The qualification is developed in different strategies by each manufacturer of CMMs/probing systems because of the very different probing systems. However, the general qualification strategy includes the following steps [14]:

- Selection of the calibrated artefact
- Choice of the location and orientation of the artefact
- Definition of number, location and sequence of probing points (for scanning mode: scanning lines, data rate, and travelling speed)

Each influencing parameter (probing force and direction, operating mode, stylus with tip ball etc.) must be chosen as far as possible to be identical with the measurement to be performed afterwards with the qualified probing system [2].With the probed points, the parameters to be calibrated can be derived by mathematical fitting methods and then the parameters can be exploited for compensation of acquired data from the surface.

2.2.2. Laser scanning

2.2.2.1. Principle of the laser scanning system

In comparison to tactile probing, the laser scanner can acquire a high density of point data with significantly higher measurement speed (typically thousands to tens of thousands of

points per second). Laser scanning offers the possibility to measure surfaces points from multiple features in a single scanning pass resulting in relatively simpler probing paths, reducing the human labour required. Its non-contact nature also makes it suitable to measure the surfaces with flexible materials [3]. This makes it a common choice in RE applications and quality control of free form surfaces. However, laser line scanning is sensitive to issues almost irrelevant to tactile based methods such as ambient light, surface colour, shininess, transparency and other surface properties influencing the measurement results [15]; it also suffers from digitizing of the non-surface features, such as slots or holes, due to occlusions and obscuration of these artefacts.

The laser scanner works based on optical triangulation method. Within the triangulation principle a point on an object surface can be determined by the trigonometric relations between a camera, a projector and the object itself. A basic geometric relationship for a 1D triangulation principle is shown in Figure 2-5 (a) [16].

(a) Triangulation in 1D   (b) Triangulation in 2D
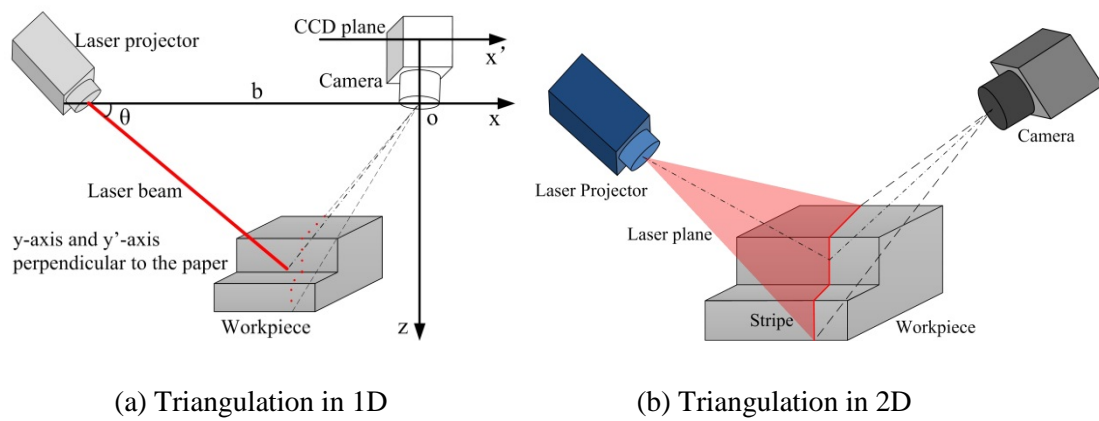
Figure 2-5: Triangulation principles in laser scanning

Where, a single camera is aligned along the z-axis with the center of the lens located at origin. At a baseline distance b, to the left of the camera (along the negative $x-axis$), a laser projector sends out a beam of light at a variable angle θ, relative to the $x-axis$ baseline. The point (x, y, z) is projected into the digitized image at the pixel (x', y') so $x'z = x'f$ and $y'z = yf$ by similar triangles, where f is the focal length of the camera in pixels. The measured quantities (x', y', θ) are used to compute the (x, y, z) coordinates:

$$x = \frac{b}{f \cos \theta - x'} x'$$

(2-4)

$$y = \frac{b}{f\cos\theta - x'} y' \qquad\qquad (2\text{-}5)$$

$$z = \frac{b}{f\cos\theta - x'} f \qquad\qquad (2\text{-}6)$$

For any fixed focal length f and baseline distance b, the range resolution of a triangulation system is only limited by the ability to accurately measure the angle θ and the horizontal position x'.

The measuring areas of common laser triangulation sensor (1D sensor) range from millimeters to centimeters [3]. The laser point scanning in 1D is limited in accuracy and efficiency. An extension of the triangulation principle is known as laser line scanning (2D sensor). The laser line scanner projects a laser plane onto the specimen and so a profile can be captured by camera each time, as shown in Figure 2-5 (b). The calculation method of each point on the scanning line or profile is similar as the 1D triangulation. However, the efficiency is greatly improved.

The accuracy of a laser scanner usually depends on many factors, such as the optical aberration of the lenses, the calibration method used, the relative position of the scanner and the object, the view angle and the condition of the surfaces etc. [17, 18]. The typical measurement range of laser scanning is ± 5 to ± 250 mm, and accuracy is about 1 part in 10,000 and measurement frequency of 40 kHz or higher [19, 20].

2.2.2.2. Modelling of the laser scanning system

As the laser line scanner is a 2D sensor, the camera of the scanner acquires a line image on the CCD (charge-coupled device) camera array at each scan. Each pixel on the line image corresponds to a point on the object surface. As the perspective projection principle is most commonly used in camera model [21], the modelling of a laser scanning system is shown in Figure 2-6 [22].

ICS: Computer image plane coordinate system
ACS: CCD array plane coordinate system
CCS: Camera coordinate system
WCS: Workpiece coordinate system
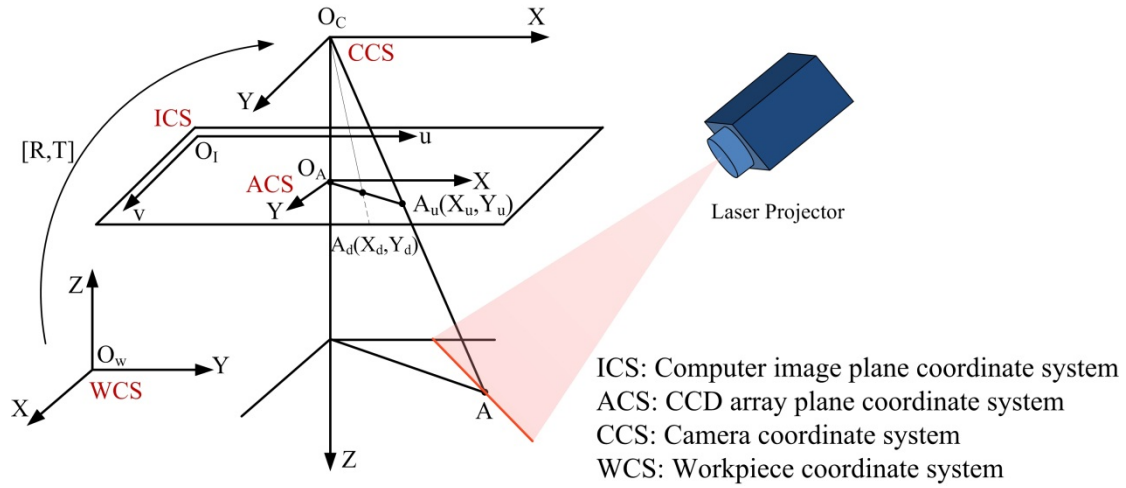
Figure 2-6: Perspective projection model of the laser line scanning system

Where CCS is 3D camera coordinates system, O_C is the optical center of the camera, $Z-axis$ is the optical axis of the camera lens, and $O_C X$ and $O_C Y$ are parallel to $O_A X$ and $O_A Y$, respectively. $O_A XY$ is CCD array plane coordinates system, O_A is the intersection of the $Z-axis$ and $O_A XY$, WCS is 3D workpiece coordinate system (also can be regarded as world coordinate system), which is set up to describe the position of any object in the real world. $O_C O_A$ is the camera effective focal length f. $O_I uv$ is 2D computer image coordinate system which is in same plane with $O_A XY$; O_I is the origin of the image plane, the unit of $u-axis$ and $v-axis$ is pixel. Let (u_o, v_o) be the coordinate of O_A in the $O_I uv$, here (u_o, v_o) is the principle point. It should be stressed that owing to possible misalignment of the CCD array, O_A does not necessarily coincide with the geometrical centre of image plane.

A is a point on the surface in the WCS or CCS, its correspondence in the ACS should be $A_u(X_u, Y_u)$. Then the transformation from WCS to ICS can be derived through the following process.

The transformation from WCS to CCS is

$$\begin{bmatrix} x \\ y \\ z \end{bmatrix} = R \begin{bmatrix} x_w \\ y_w \\ z_w \end{bmatrix} + T = \begin{bmatrix} r_1 & r_2 & r_3 \\ r_4 & r_5 & r_6 \\ r_7 & r_8 & r_9 \end{bmatrix} \begin{bmatrix} x_w \\ y_w \\ z_w \end{bmatrix} + \begin{bmatrix} t_x \\ t_y \\ t_z \end{bmatrix} \tag{2-7}$$

where R is a 3×3 rotation matrix and T is a translation vector.

According to perspective projection principle, the transformation from ACS to CCS is

$$\rho \begin{bmatrix} X \\ Y \\ 1 \end{bmatrix} = \begin{bmatrix} f & 0 & 0 \\ 0 & f & 0 \\ 0 & 0 & 1 \end{bmatrix} \begin{bmatrix} x \\ y \\ z \end{bmatrix} \qquad (2\text{-}8)$$

where ρ is scale factor.

The transformation from ACS to ICS is

$$\begin{cases} u = u_o + \dfrac{X_u}{\mu_x} - \dfrac{Y_u \cos\theta}{\mu_x} \\[3mm] v = v_o + \dfrac{Y_u}{\mu_y \sin\theta} \end{cases} \qquad (2\text{-}9)$$

where μ_x and μ_y is the physical dimension of each pixel in the $O_A X - axis$ and $O_A Y - axis$ direction, respectively. They can be derived from the specifications of the CCD cameras given by their manufacturers. θ is the angle between the $O_A X - axis$ and $O_A Y - axis$. Considering that industrial cameras designed for this application are manufactured with tight tolerances, which leads to θ very close to 90 degrees. In this case, assuming that $\theta = 90°$ will not affect camera calibration accuracy [23].

Define $N_x = \dfrac{1}{\mu_x}$ and $N_y = \dfrac{1}{\mu_y}$, Equation (2-9) can be rewritten as

$$\begin{cases} u = u_o + N_x X_u \\ v = v_o + N_y Y_u \end{cases} \qquad (2\text{-}10)$$

As the camera optical system does not work accurately according to idealized pinhole imaging principle, the lens distortion must be considered when a camera is calibrated. Therefore the actual corresponding point of A in the CCS is A_d instead of A_u in the ACS due to the lens distortion. There are mainly three types of lens distortion [24]: radial distortion, decentering distortion and thin prism distortion. Tsai [22] states that only radial distortion needs to be considered for industrial machine vision application. This conclusion can be verified by the Matlab toolbox provided by Bouguet [25], which shows that for the most lenses currently manufactured, the tangential component model is significantly smaller that the radial component. And to Tsai's experience, only first-order radial distortion needs to be

considered because any more elaborate modelling not only would not help but also would cause numerical instability. Since the radial distortion is the main factor that affects the measurement accuracy, here we only take the first-order radial distortion in consideration in establishing the camera model. The relationship between (X_u, Y_u) and (X_d, Y_d) is

$$
\begin{cases}
X_u = X_d(1 + k(X_d{}^2 + Y_d{}^2)) \\
Y_u = Y_d(1 + k(X_d{}^2 + Y_d{}^2))
\end{cases}
\tag{2-11}
$$

Substituting Equations (2-7), (2-10) and (2-11) into Equation (2-8), finally, the coordinates of the point $A(x_w, y_w, z_w)$ represented in the WCS can be derived from the following formula:

$$
\rho \begin{bmatrix} u \\ v \\ 1 \end{bmatrix} = \begin{bmatrix} fN_x r_1 + r_7 u_o & fN_x r_2 + r_8 u_o & fN_x r_3 + r_9 u_o & fN_x t_x + t_z u_o \\ fN_y r_4 + r_7 v_o & fN_y r_5 + r_8 v_o & fN_y r_6 + r_9 v_o & fN_y t_y + t_z v_o \\ r_7 & r_8 & r_9 & t_z \end{bmatrix} \begin{bmatrix} x_w \\ y_w \\ z_w \\ 1 \end{bmatrix}
\tag{2-12}
$$

The parameters mentioned in Equations (2-12) can be obtained by a calibration process.

2.2.2.3. Calibration of the laser scanning system

The goal of calibration is to determine the transformation from 2D image data in CCD array to the 3D spatial coordinate system. The parameters need to be calibrated include intrinsic parameters and extrinsic parameters. Define

$$
A_C = \begin{bmatrix} N_x & 0 & u_o \\ 0 & N_y & v_o \\ 0 & 0 & 1 \end{bmatrix}
\tag{2-13}
$$

Equation (2-12) can be written as

$$
\rho \begin{bmatrix} u \\ v \\ 1 \end{bmatrix} = A_C [R, T] \begin{bmatrix} x_w \\ y_w \\ z_w \\ 1 \end{bmatrix}
\tag{2-14}
$$

where $[R, T]$ is the camera extrinsic parameters matrix. It describe the transformation from WCS to CCS. A_C is camera intrinsic parameters matrix. Effective focal length f, scale factor ρ and distortion coefficient k are intrinsic parameters; (u_0, v_0) is the principle point, it is also an intrinsic parameter.

18

To solve all of the intrinsic and extrinsic parameters simultaneously, at least six "conjugate pairs" of non-coplanar points in the world coordinate system and their correspondences on the CCD image are required. Often more calibration points are necessary to improve the calibration accuracy. The instrument for generating 3D calibration points can be a plane with pattern or a 3D artefact.

The calibrations of CCD cameras have been investigated by a considerable number of authors. Tsai [22] proposed a two-step method, accurate calibration points can be easily obtained using this method and then the camera can be calibrated with a coplanar target. His two-stage technique was efficient, accurate, and straightforward to implement in a real environment. It was considered to be a versatile method for camera calibration more than one decade after this approach was proposed. Zhang [26] presented a more flexible technique for camera calibration by viewing a plane from different unknown orientations. The proposed technique only requires the camera to observe a plane with pattern at a few (at least two) different orientations. Either the camera or the planar pattern can be freely moved and the motion need not be known. Che, et al. [27] presented a single ball-target-based method for the extrinsic calibration of a 3D multiple-axis laser scanning system, and then developed a constrained optimization calibration algorithm. Their work focused on extrinsic calibration and did not consider intrinsic calibration problems. Wei, et al. [28] proposed a novel approach that employs an artefact consisting of two rigid planes orthogonal to each other. On each plane, there are several black squares and rectangles providing non-coplanar calibration points. Their method can generate large numbers of highly accurate world points for calibration.

After the calibration is complete, we can reconstruct the 3D spatial points (x_w, y_w, z_w) from 2D image points (u, v) based on Equation (2-14).

In the commercial laser scanning sensors (e.g. Nikon [29], Laser Design & GKS [30] and Faro [31]), the laser projector and camera are integrated together and the laser scanner is usually mounted on a CMM platform or on a robotic or a articulated arm when doing the data acquisition. Some parameters (e.g. intrinsic parameters) have been calibrated by manufactures and then only the rest (e.g. extrinsic parameters) need to be calibrated in practical applications.

2.2.3. Fringe projection

2.2.3.1. Principle of fringe projection system

If 1D and 2D sensors are not sufficient (e.g. for the sampling of complex surfaces with a high point density), fringe projection (3D sensor) can be applied for data acquisition. FPP (Fringe projection profilometry) using a phase-shifting technique has been extensively investigated

[32-42] and recognized as one of the most effective techniques for practical shape measurement.

The difference between FPP and other structured light methods is that its projection is a grating field in space. A DLP (digital light processing) projector has been commonly adopted for projecting phase stripe patterns owing to its easy availability, low cost, and high flexibility. The phase is used to describe the cycle distribution of grating field and the coordinates of points are obtained by calculating the phase of the fringe image. The FPP method projects a grating stripes field which is modulated by a periodic function onto the surface of the objects. The phase of the grating stripes offset occurs due to variation in the height of the object surface (see Figure 2-7). 3D coordinates of points can be calculated by comparison of the relationship of phase shift offset and the height of surface.

(a) Original stripes   (b) Workpiece surface   (c) Projection grating
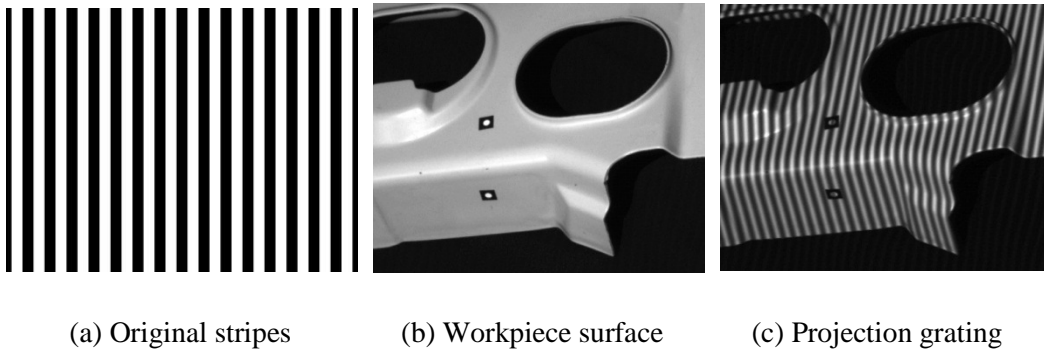
Figure 2-7: FPP scanning process

The FPP method can directly measure the overall surface of the object by a single projection because the phase in the space is continuously distributed, which is a prominent advantage of the phase method. Additionally, a higher resolution can be achieved by using the "Phase-shifting" algorithm compared to the 1D and 2D triangulation sensors.

The measurement volume of common fringe projection systems ranges from 1 mm × 1 mm × 0.3 mm to 2 m × 2 m × 0.5 m with measurement uncertainties of 0.005-0.3 mm. Uncertainty contributions depend on factors such as phase measuring errors, the distortion of the lenses and the calibration method used, etc. [11].

2.2.3.2. Modelling of fringe projection system

The camera model in fringe projection system is the same as the one that is built in laser scanning systems. A system model needed to be established to include the mapping relationship among 3D spatial points (x_w, y_w, z_w), 2D image points (X, Y) and phase θ of 3D points. The complete FPP system model [23] is shown in Figure 2-8.
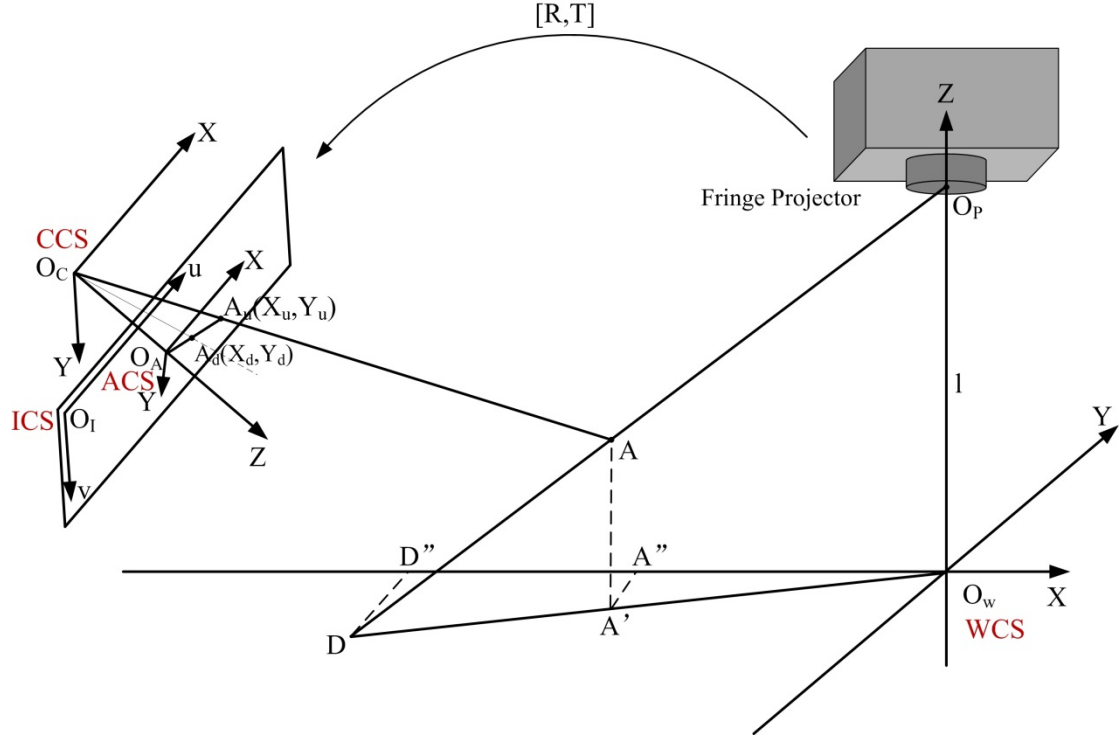
Figure 2-8: FPP system model

The meaning of ICS, ACS, CCS and WCS is also same as Figure 2-6. WCS is set up according to the position of fringe projector: $O_w XY$ plane parallels the projection plane; $O_W Y - axis$ parallels grating stripes; $O_W Z - axis$ goes through the projection center O_P. A' is the projection of 3D point A on $O_W XY$ plane. $O_P A$ and $O_W XY$ plane intersect at point D. A" and D" are projection of A' and D on $O_W X - axis$ of $O_W XY$ plane, respectively. $A_u \left(X_u, Y_u \right)$ is the image of point A on CCD array plane $O_I uv$ and its phase is θ.

The system model includes two parts: $(X, Y) - (x, y, z)$ relationship equation and relationship equation $\theta - (x, y, z)$. As the $(X, Y) - (x, y, z)$ relationship has been established in Equation (2-8), here only the relationship between point (x, y, z) in the CCS and its phase θ is needed to be considered.

As shown in Figure 2-8, A' and O_W are projections of point A and O_P on $O_W XY$ plane, respectively, therefore $AA' // O_p O_W$, $\Delta DA'A \backsim \Delta DO_W O_P$, where

$$\frac{O_w A'}{O_w D} = \frac{O_w O_P - A'A}{O_w O_P} \tag{2-15}$$

21

A'' and D'' are projection of A' and D on $O_W X - axis$ of $O_w XY$ plane, respectively, therefore $A''A'//D''D'$, $\Delta O_w A'' A' \backsim \Delta O_w D'' D$, where

$$\frac{O_W A'}{O_W D} = \frac{O_W A''}{O_W D''}$$

(2-16)

From Equation (2-15) and (2-16), we have

$$\frac{O_W A''}{O_W D''} = \frac{O_W O_P - A'A}{O_W O_P}$$

(2-17)

where $O_W O_p = l$; D'' are projection of D on $O_W X - axis$ of $O_W XY$ plane. $O_W Y - axis$ parallels grating stripes, therefore D'' and D have same phase value also equal phase value θ of A, where

$$O_W D'' = \frac{\lambda_o}{2\pi}(\theta - \theta_o)$$

(2-18)

where θ_o is phase of origin O_W, λ_o is grating step, which is the length corresponding to one cycle (2π) of the phase variation.

Substituting Equation (2-18) to (2-17), we have

$$\theta = \frac{(2\pi l / \lambda_o)x - \theta_o z + l\theta_o}{l - z}$$

(2-19)

Substituting Equation (2-7) to (2-19),

$$\theta = \frac{a_1 x + a_2 y + a_3 z + a_4}{a_5 x + a_6 y + a_7 z + a_8}$$

(2-20)

where

$$a_1 = 2\pi(r_1 - \theta_o r_7)l / \lambda_o$$
$$a_2 = 2\pi(r_2 - \theta_o r_8)l / \lambda_o$$
$$a_3 = 2\pi(r_3 - \theta_o r_9)l / \lambda_o$$
$$a_4 = 2\pi(t_x - \theta_o t_z)l / \lambda_o + \theta_o l$$
$$a_5 = -2\pi r_7 l / \lambda_o$$
$$a_6 = -2\pi r_8 l / \lambda_o$$
$$a_7 = -2\pi r_9 l / \lambda_o$$
$$a_8 = -2\pi t_z l / \lambda_o + l$$

Equation (2-20) is $\theta - (x, y, z)$ and describes the relationship between phase θ and 3-D coordinates in the CCS, $a_1, a_2, a_3, a_4, a_5, a_6, a_7, a_8$ are system parameters to be calibrated.

To combine Equations (2-7), (2-8), (2-11) and (2-20), we obtain a complete 2D to 3D $(X, Y, \theta) - (x, y, z)$ model. In practical measurement, substitute coordinate value of each point (X, Y) in the ACS and its phase value θ, then the 3D spatial point coordinate (x_w, y_w, z_w) is acquired.

2.2.3.3. Fringe image processing

Phase analysis and processing is another key knowledge in fringe projection technology. For a FPP system, phase nonsinusoidal error and phase-shifting error of grating stripes are the main error sources [43, 44]. The camera is used to take images of objects under an auxiliary light source field, which is the stripes image. The image includes modulated information of object height and grating stripes phase value. Therefore accurate interpretation of the fringe image is an important part of obtaining accurate measurement results. While interpreting the image to obtain phase value, the question arises how they are to be derived.

It is a two-step process to obtain phase θ: first obtain the main phase value of the fringe image in the range of 0 to 2π; second recover the main value phase field to the complete phase field, which is called phase unwrapping.

Moire Fringe [33], Fourier transform [34-36] and phase-shifting [37-39] methods have played huge roles in facilitating projection measuring technology. Phase-shifting methods can provide better accuracy of results and have good usability, therefore phase-shifting followed by the Gray-code method [40, 41] have been widely used in practical application of image processing.

(1). Phase-shifting method

Phase-shifting technique is such that several sinusoidal gratings are projected onto the surface of objects. Among the various phase-shifting algorithms available [45], the three-step phase-shifting method [46, 47] is the simplest and requires the minimum number of frames, which uses $2\pi/3$ phasing-shift. However, four-step phase-shifting algorithm [48] is currently the most widely used method because it uses $\pi/2$ phasing-shift which is relatively easy to implement in the optical mechanisms; four sinusoidal gratings are projected in the cycle for 0, $\pi/2$, π, $3\pi/2$ and each of them offset ¼ cycle.

$$
\begin{aligned}
I_1(m,n) &= I'(m,n) + I''(m,n)\cos[\theta(m,n)] \\
I_2(m,n) &= I'(m,n) + I''(m,n)\cos[\theta(m,n) + \pi/2] \\
I_3(m,n) &= I'(m,n) + I''(m,n)\cos[\theta(m,n) + \pi] \\
I_4(m,n) &= I'(m,n) + I''(m,n)\cos[\theta(m,n) + 3\pi/2]
\end{aligned}
\tag{2-21}
$$

where each pixel can get a light intensity value $I_i(m,n)(i=1,2,3,4)$ is light intensity value of each pixel, $I'(m,n)$ is the average intensity, $I''(m,n)$ is the intensity modulation, $\theta(m,n)$ is the phase.

The theoretical phase value of the pixel $\theta(m,n) = \phi(m,n) + 2k(m,n)\pi$ can then be calculated through the following formula:

$$
\phi(m,n) = \arctan\frac{I_4(m,n) - I_2(m,n)}{I_1(m,n) - I_3(m,n)}
\tag{2-22}
$$

$\phi(m,n)$ obtained in this way is the main value and unique at the phase $[0, 2\pi]$.

(2). Phase unwrapping

Phase wrapping in the phase-shifting method is the process of determining the phase values of the fringe patterns in the range of 0 to 2π [45]. Phase unwrapping, on the other hand, is the process of removing the 2π discontinuity to generate a smooth phase map of the object [49].

Considering the period of trigonometric functions is 2π, the complete phase value $\theta(m,n)$ of the coding can be obtained by the following formula:

$$
\theta(m,n) = \phi(m,n) + 2k(m,n)\pi
\tag{2-23}
$$

$k(m,n)$ is an integer and represents cycles of grating stripe of point (m,n). Therefore the key to phase unwrapping is to identify $k(m,n)$.

There are mainly two types of phase unwrapping methods: temporal and spatial method [50]. Temporal phase-unwrapping methods [51, 52] such as the Gray-code method [53] project sufficient different frequencies within a fringe pattern according to time sequence to generate adequate encoded information and use this information to unwrap the absolute phase value. Gray-code is a kind of binary code where there is only one different bit coding between every two adjacent codes. If black stripes express logical 0 and white stripes express logical 1, then the n-bit Gray-code can be acquired through continuous projection of n pieces of different frequency grating of black and white. After image acquisition, each pixel of a CCD finally gets a gray value vector. Binary images can acquire a Gray-code coding and this can determine a number of discrete stripes.

(4). Calibration of fringe projection system

Based on above model, the calibration of the system includes intrinsic & system parameters. The camera's intrinsic parameters are the matrix A_C and parameters such as focal length f, scale factor ρ and distortion coefficient k in $(X,Y)-(x,y,z)$ relationship equation. Parameters $a_1, a_2, a_3, a_4, a_5, a_6, a_7, a_8$ in $\theta-(x,y,z)$ equation are the system parameters.

The calibration method for the camera's intrinsic parameters has been described in Section 2.2.2. The strategy for calibration of the system parameters is quite similar to that for camera. Thus, all these parameters can be calibrated by using a 3D target or a planar artefact with patterns. The patterns could be cross line, circle or chessboard (see Figure 2-9), which are relatively simple to obtain with high accuracy, although caution must be taken to ensure that the manufacturing process does not introduce distortion.

| (a) Cross line | (b) Circle | (c) Chessboard |
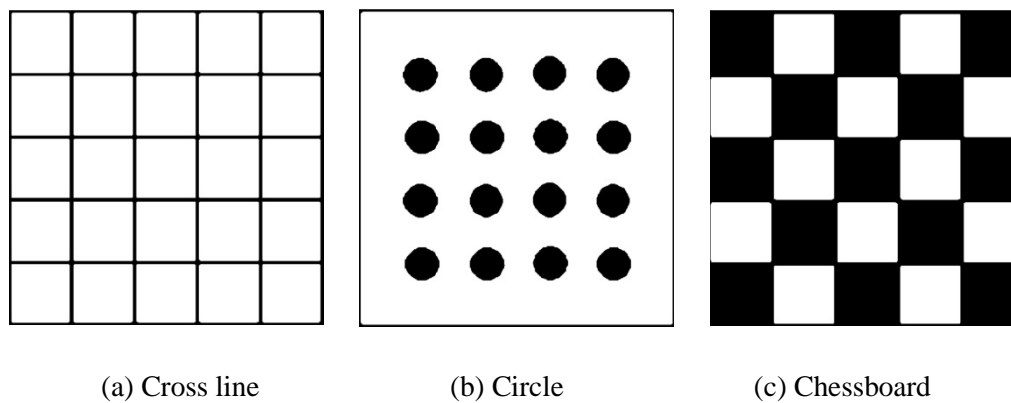
Figure 2-9: Typical calibration patterns

By processing the planar image, the edges of the squares or circles can be extracted and fitted to lines or centres of circles. Then the corner points or centre points can be used as calibration

points. Therefore a minimum of eight sample points (x_i, y_i, z_i, θ) (which represents the 3D coordinate (x_i, y_i, z_i) of *ith* sample point and its phase value θ) need to be captured and then substitute them to Equation (2-20), all the eight unknown parameters can be determined.

It should be noted that when the camera settings or relative position of the camera(s) and projector changes, the calibration has to be repeated for correct measurement results.

2.2.4. Comparison of the three sensors

To measure a complex workpiece containing various detailed features, the most suitable sensor should be selected for each particular feature. Table 2-1 presents the main characteristics comparison of the three sensors.

The three sensors mainly cover the measurement tasks in micro domains with 2D and 3D data acquisition. The measurement system integrating the three sensors can be exploited to implement the general applications in dimensional measurement, RE, etc.

Table 2-1: Comparison of the main characteristics of the three sensors

	Tactile probing	Laser scanning	Fringe projection
Principle	Mechanical interaction	Laser triangulation	Triangulation & Phase-shifting
Resolution (µm)	0.01~1	0.1~100	0.1~100
Measuring range (mm)	0.01×0.01×0.01~1000×1000×1000	5×5×5~250×250×250	5×5×5~1000×1000×300
Speed	Several points/second	Tens of thousands of points/second	Millions of points/second
Init. Data type	3D (X, Y, Z)	2D (R, C)	2D (R, C)
Advantages	1. High resolution/accuracy 2. Not sensitive to the surface reflection 3. Robust and not sensitive to the ambient light	1. High scanning speed and dense point data acquisition 2. Global information acquisition 3. Suitable for the measurements of surfaces with soft/flexible materials	1. Very high scanning speed and dense point data acquisition 2. Global information acquisition 3. Suitable for the measurements of surfaces with soft/flexible materials
Disadvantages	1. Low data capturing speed 2. Limitations to its own dimension sizes 3. Sparse density of the acquired points data	1. Low resolution, noisy/redundant data 2. Limitations of occlusion and viewpoint 3. Sensitive to the surface optical conditions	1. Low resolution, large number of noisy/redundant points 2. Limitations of occlusion and viewpoint 3. Very sensitive to the surface optical conditions and ambient light
Applications	1. Primitive shapes 2. Features with known CAD models 3. Surfaces without large variations	1. Global data acquisition 2. Complex surfaces or topography measure 3. Parts with soft/flexible materials	1. Body scanning 2. Global information acquisition 3. Complex surfaces or topography measure

2.3. Multi-sensor integration in coordinate measurement

The reduction of the lead time in measurement, and the increased requirements in terms of complexity, accuracy and flexibility have resulted in a great deal of research effort aimed at developing and implementing combined systems based on integration of different (homogeneous and inhomogeneous) sensors. Multi-sensor data fusion methods then are

employed to achieve both holistic geometrical measurement information and improved reliability or reduced uncertainty of measurement.

A multi-sensor integration system in dimensional measurement is a measuring system which combines several different sensors in order that the measurement result can benefit from all available sensor information and data. While fusing data sets, characteristics such as resolution and measuring ranges have to be considered. On the other hand, due to the different measuring techniques and their physical working principles, different interactions between the workpiece and sensor occur and different surfaces are captured. With a multi-sensor integration system, particular features of a workpiece can be measured with the most suitable sensor, and the measurement with small uncertainty can be used to correct or replace data from other sensors which exhibit relevant systematic errors but have a wider field of view or application range. Therefore, the merits of each sensor in the integrated system can be fully utilized and their disadvantages can also be mitigated to improve the data acquisition performance of the whole system.

2.3.1. Multi-sensor configuration

Sensors of a similar type which capture the same or a comparable physical object to be measured are called homogeneous sensors. On the other hand inhomogeneous sensors acquire different characteristics of a scene. Multi-sensor fusion performs the synergistic application of different homogeneous and inhomogeneous sensors to execute a given measuring task. The integration approach of multiple sensors into a multi-sensor system depends on the application and sensor data or signal type. Durrant-Whyte [54] classifies physical sensor configuration in a multi-sensor data fusion system into three categories as shown in Figure 2-10: competitive, complementary and cooperative integration.

- A competitive sensor configuration is one where the sensors are configured to measure the same feature independently in order to reduce the measurement uncertainty and to avoid erroneous measurements. For example, an image sensor measures the same area and the redundant information is averaged by evaluating the mean for each pixel. Thereby all images of the series contribute equally to the final measurement result [55].

- A complementary sensor configuration is one where the sensors do not directly depend on each other but can be combined in order to give more complete information about the object. Complementary sensors can be exploited to resolve the problem of incompleteness of acquired data. An example is the data fusion of images captured with different illumination series to achieve images with higher contrast [56].

- A cooperative sensor configuration uses the information provided by one or more independent inhomogeneous sensors to drive one or more other sensors for measuring. Often, cooperative sensor configurations allow measurands that have not previously be evaluated to be measured. A practical example of this kind of sensors configuration would be the case of multi-sensor integrated on the CMM platform and use of the global information acquired by an optical sensor to guide the tactile probe for high precision coordinate data acquisition [7].

(a) Competitive   (b) Complementary   (c) Cooperative
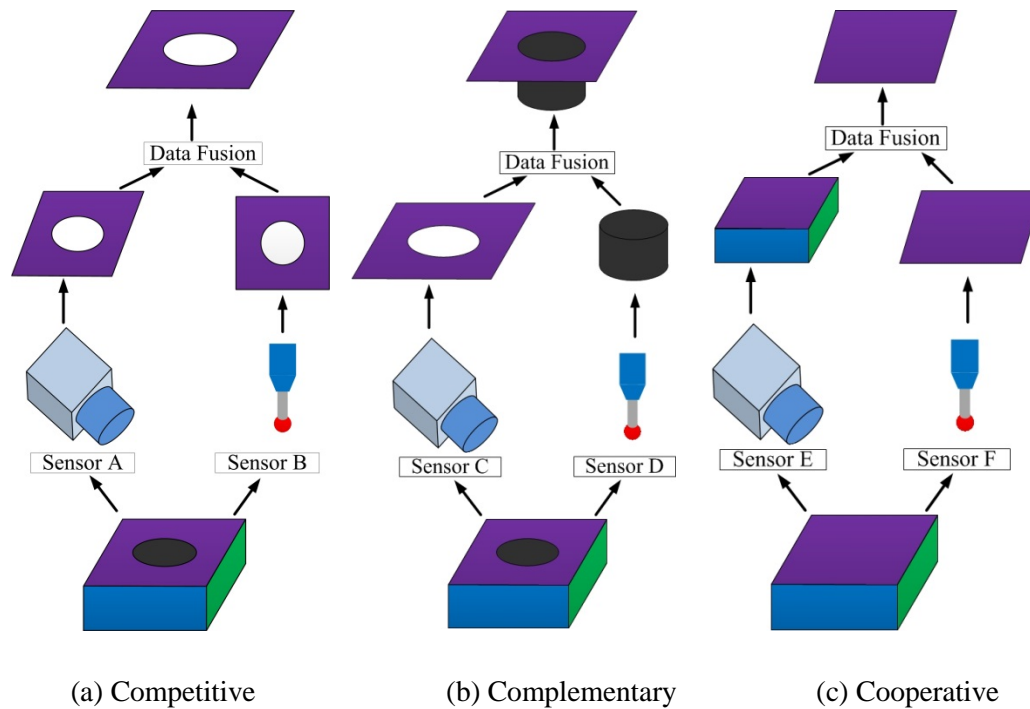
Figure 2-10: Sensors configurations in multi-sensor systems

2.3.2. Theoretical aspects of multi-sensor data fusion

The data acquired by the each sensor in the integrated system, dependently or independently, are embedded in their own coordinate systems which are distinctly different from each other. There are many key issues that need to be considered for data processing in order to achieve the multi-sensor data fusion. Generally, the process of the multi-sensor data fusion based on different information sources should include the following procedures:

- Data pre-processing
- Data registration
- Data fusion

2.3.2.1. Data pre-processing

The information captured by different sensors is not directly linkable, the raw data acquired from multiple sensors are typically needed to pre-process to improve their qualities, such as error points removal, data filtering, data reduction, etc.

(1). Error points removal

Typically parts need to be clamped before scanning. The geometry of the fixtures is scanned by optical sensors and becomes a part of the scan data. Then the fixture data should be eliminated manually. Some error points, for example the bed of CMM is scanned when using optical sensor and these points obviously do not belong to the parts, they also need to be manually removed.

(2). Data filtering

In order to better exploit the high density point data, a data filtering method is often applied. Usage of data filtering is a common practice in RE application. Various techniques [57, 58] are used successfully to improve point cloud quality by decreasing measurement noise. Filtering methods will be discussed further in Section 4.2.1.

(3). Data reduction

The raw point cloud scanned by optical sensors usually contains hundreds of thousands points, because of the high resolution of CCD cameras. Furthermore, some features on the parts are repeatedly scanned, especially when multiple views of an object are required to capture the full model, which also introduce a large number of redundant points. It might take a lot of computing time if all these original points are input into triangulation process to generate a polyhedral model of this model. Therefore the vast amounts of data need to be reduced in order to improve the efficiency of the subsequent treatments [59].

After pre-processing, the data becomes more conducive to further processing. The pre-processing in multi-sensor data fusion should also include the data format conversion when it is necessary.

2.3.2.2. Data registration

Data registration has two purposes: a) 3D point data scanned from different views by the subsystem in their local coordinate system are aligned into a global coordinate system; and b) data acquired by different sensors are transfer into a common coordinate system. In this thesis, data registration refers to the latter purpose.

As every employed sensor has its own coordinate system, which is usually different from each other, the measured data from each other should be transformed and merged into a common coordinate system in order to build a complete 3D model. Moreover, in the recognition and position stages prior to the shape inspection, the digitized data from unfixed rigid objects also needs to be registered with an idealized geometric model [60]. Therefore, registration is one of the most critical issues and decisive steps of multi-sensor data fusion.

The transformation parameters include 3D rotations and translation. When data sets (e.g. images) are acquired with different magnifications, transformations of proportion, sometimes known as "scaling", may also need to be considered. Commonly, the criterion for determining the transformation parameters is the Least Squares Criterion. This involves the minimization of the variance of distances of corresponding points in the sensor data or of corresponding points in overlapping areas [11].

2.3.2.3. Data fusion

The data fusion process is performed to decide which measurement data should be integrated into the final data set and how to handle the redundant data. The methods for data fusion broadly belong to one of the following three techniques: estimation, inference, fuzzy or neural methods [11]. Estimation methods, which include least square analysis [61] and weighted average [62] are suitable to analyse the measurement systems where various results are acquired for the same measurand or for a regression plot are combined. They are typically applied to steady-state measurements [63]. In addition, Kalman filtering and its further developments are usually used as model-based stochastic state-estimators in processing of time-dependent and time-discretised digital measurement signals [64, 65]. Inference methods, like Bayesian probability theory are used for measurement data evaluation and contemporary uncertainty determination [66, 67].

2.3.3. Related research in multi-sensor integration

The theoretical origins of data fusion can be traced back to the late sixties, although a broad application of these techniques did not take place until the early eighties [68]. In the meantime, the research activities on data fusion have become very extensive and applications to different fields have been reported, such as robotics [69], pattern recognition [70], medicine [71], non-destructive testing [72], geo-sciences [73], military reconnaissance and surveillance [74], etc. In the following, comprehensive research works related to measurement and RE are presented.

2.3.3.1. Homogeneous optical sensors integration

The homogeneous sensors, such as cameras, laser scanners, fringe projection scanners, or other optical sensors, are integrated into a multi-sensor system to achieve a representation of sufficient data and/or better measurement accuracy.

One typical example is the multi-station photogrammetry network which integrates several homogenous cameras. After calibration of the system, each observation of the object can be captured with several images simultaneously. These images are registered to a global coordinate to obtain a final point cloud [75]. Similarly, Aguilar, et al. [76] developed a fast stereo metric system, which integrates two holographic optical elements, to measure free-form surfaces of railway concrete sleepers and calculate track and rail seat dimensional tolerances.

Moreover, a series of images captured by a single sensor (called virtual sensor in [77]) also can be classified as a homogeneous sensor fusion problem. Instead of multiple sensors capturing simultaneously, a single optical sensor is used to digitize the object several times in succession to obtain a series of images with different focal depths, positions or view orientations. Then more detailed information can be extracted from these images. Such applications are quite widely studied and implemented due to its economy and flexibility. One example of this integration setup is when applying the 'shape from shading' technique. The setup consists of different illumination sources and a fixed camera and the camera captures a series of grayscale images with different illuminations. The height map of the object can be derived by the gradients analysis and calculation in these images [78, 79]. Another example is data fusion in the fringe reflection method, also called deflectometry. From the measured deflectometric data, different approaches allow for reconstruction with the aid of additional knowledge or the fusion of several measurements [80].

For the three-dimensional shape measurement of complex structures for example freeform surfaces, fringe projection systems are applied. Fringe projection can be installed in mobile systems or in coordinate measuring machines. Two or more cameras are usually used to capture the information simultaneously after system calibration to achieve better surface coverage. Often, the objects to be measured are bigger than the measurement range of the cameras or too complex to be captured in one single measurement. In a complementary integration, multi-views are taken from different camera orientations and registered and fused into a global coordinate system [81], problems such as shading can be solved with such a setup [82].

2.3.3.2. Inhomogeneous optical sensors integration

Like the homogeneous optical sensor integration, the multiple inhomogeneous optical sensors with different measuring principles and resolution can also be combined by cooperative or complementary integration and applying multi-scale measuring and verification strategies.

In cooperative configuration systems, the lower resolution sensors are usually used to capture the global information with restricted resolution. Then, a data analysis phase follows to evaluate the information content. Further local measurements with higher resolution sensors are required if there is not sufficient information. The resultant data is updated after combining each additional measurement datum until the measurement tasks are fulfilled. The system developed by Weckenmann, et al. [83] combines a fringe projection system and a white light interferometer to measure the wear of cutting tools. A compact sensor head combining an optical interference microscope with a scanning probe microscope in a single measurement is demonstrated in [84]. Sokolov, et al. [85] introduces a combined confocal sensor and scanning probe system for nano-coordinate metrology.

Some systems of complementary configurations of inhomogeneous optical sensors have also been demonstrated by several authors. Reich, et al. proposed a multi-sensor system by combining photogrammetry and fringe projection for shape measurement of complex objects [86]. Schmitt, et al. [87] developed a method for the automated positioning and alignment of fibre-reinforced plastic structures by data fusion of two optical sensors. The first sensor is an image processing sensor for the robust detection of the local fibre orientation and the second one is a light section sensor for the determination of the contour position of textile preforms. The developed method was evaluated under industrial conditions through a prototype. It can measure different quality criteria of preform structures.

2.3.3.3. Tactile and optical multi-sensor integration

Even though tactile and optical sensing technologies are widely used in data acquisition in dimensional measurement and RE, it has been shown that each technique has its own characteristics and applications. The requirement of both high speed and high accuracy 3D measurement in modern measurement or RE have resulted in a great deal of research effort aimed at developing and implementing combined systems based on integration of inhomogeous sensors such as mechanical probes and optical sensors.

(1). Cooperative configurations

The optical sensors can be a simple video camera, a laser scanner or a fringe projection system, which acquires the global shape information and provides the guidance information to

drive the CMM to execute the local exploration with a more precise tactile probe [11]. In such systems, the advantages of the two kinds of sensors can be exploited at the same time, i.e. the ability of the optical sensor to quickly generate the approximate shape and the ability of the contact probe to obtain higher accurate measurement result. Nashman, et al. [88] developed a real-time integrated system that combines a vision system and a touch probe for dimensional inspection tasks. The low resolution vision camera is fixed on the CMM table and provides the global information. Then the images captured by vision camera are used for the workpiece positioning. With comparison of the image data and the data generated by the probe, the fused information is used to guide the tactile probe to provide the final inspection data. This makes automatic capture of specific features more efficient.

Motavalli, et al. [89] described an similar integrated sensory system combing contact probe and two cameras for RE applications. In their work, one vertical camera is mounted on the CMM for viewing the part from the top. The other camera is placed on a stand for viewing the part horizontally. The processed images are then used to guide the touch probe to automatically digitize the surfaces and create CAD representations of part prototypes.

Shen, et al. [7] presented a cooperative sensor integration system that fused a 3D active vision (fringe projection) system and a touch probe for rapid and high precision coordinate metrology. Intelligent feature recognition algorithms can be applied to extract the global surface information acquired using the 3D active vision system. The obtained information can be subsequently used to automatically guide the touch probe for rapid coordinate data acquisition and to strategically control the probe for high precision sampling of critical surface area.

Chan, et al. [5] developed a multi-sensor system integrating a CCD camera and a tactile probe on a CMM platform for RE. The two sensors are fixed on the CMM arm together. The images captured by the CCD camera are processed by neural network algorithm based method to provide the geometric data which can be used for locating the object and planning the probing path of the tactile sensor. The CCD images play the role of the CAD model like in CAD model based inspection planning systems.

Similarly, Carbone, et al. [6] proposed a method to combine a stereo vision system and a touch probe. In their method, the 3D vision system is performed to acquire a number of clouds of points to generate a rough CAD model and to guide the mechanical probe to digitize the surfaces. The touch point data are then imported to the CAD environment to produce the final, accurate CAD model.

Chen, et al. [90] proposed a multi-sensor automatic inspection system, which combines the coordinate measuring machine with conoprobe laser sensor and can select automatically either of the two methods for different (simple-geometry or complex free-form) measured objects so as to raise the accuracy and efficiency of measurement.

In summary, the implementation of above integrations tends to be cooperative where optical sensors provide approximate shape to guide the tactile sensor for automatic digitization. This improves efficiency, but has no direct benefit on accuracy.

(2). Complementary configurations

The complementary integration systems have also been studied by several authors.

Bradley, et al. [91], Chan, et al. [92], and Jamshidi, et al. [93], each presented separate integrated laser-tactile systems. A laser scanner is used to scan large area surface patches and achieve sufficient data sampling, whereas a CMM touch probe is used to precisely define the boundary of bounding contours. Both sensors are mounted on the CMM arm. Generally, the objects need multiple scans with different views by the laser scanner to acquire complete point data.

Xie, et al. [94] presented a complementary sensor approach for RE. In their work, a multi-probe measurement system integrated with a CMM, a structured-light sensor, a trigger probe and a rotary table has been developed. The structured-light sensor is applied to scan the profile of a part from different views, while the trigger probe is used to measure the edge and key features of the part. Then the data generated by different modes can be merged into a whole data set.

Sladek, et al. [8] presents a hybrid contact-optical coordinate measuring system for metrology. The structured light system is used to acquire the surface of workpiece, then numerical analysis is performed to calculate a set of surface points that should be finally re-measured by the CMM. The combination of measuring systems enables the measurement of a wider range of objects than for any single system alone and the limitations of each system are compensated by the other.

Zhao, et al. [95] presented an automated dimensional inspection planning method using the combination of a laser scanner and a tactile probe. The inspection features are specified and selected based on the extracted geometry features and the associated Product & Manufacturing Information items from a CAD model. Then a knowledge based sensor selection method is applied to choose the suited sensor for each inspection feature.

In summary, complementary integration systems select different probing methods to measure different features, often based on the principle that tight tolerance or non-surface elements should be measured by high-precision contact probing, while elements with looser tolerance can be scanned via optical techniques.

(3). Competitive configurations

Only limited research on competitive integration of hybrid contact-optical sensors has been found. In the work presented by Huang, et al. [96] and Bešić, et al. [97], reduction of the measurement uncertainties has been studied. This will be detailed in Chapter 4. This thesis focuses on the development of a competitive integration of optical-tactile sensors for the RE applications, which will be discussed in Chapter 4.

Moreover, ElMaraghy and Rolls [98] analysed digitizing errors between tactile probe and laser scanning data. The integrated tactile and optical sensor calibration problem has been researched by Shen, et al. [7, 99]. They developed an automatic camera calibration scheme, by adopting the tip of the CMM probe to provide high-precision 3D coordinates for camera calibration and to establish a common coordinate system for sensor integration.

2.3.3.4. Other multi-sensor integration

There are also other multi-sensor coordinate measuring setups are developed. One example is a complementary integration system which consists of a specially designed light pen with point shaped LED light sources which are aligned in one line with the probe stylus and a high-resolution CCD. On the basis of knowing the positions of the light sources and the probe stylus the 3D coordinates for the centre of the probe stylus can be calculated. During measurement the touch trigger probe contacts the object measurement surface and the image of the light sources is captured by dual CCD cameras. Then the coordinate rotation and translation between the two camera coordinate systems is calibrated. Experimental results of such a setup showed the axis orientation errors were eliminated and a better stability and precision with an uncertainty of ±0.1 mm in the distance of 2 m [100].

To improve measurement precision, recent research activities have tried to exploit Dual Energy Computed Tomography (CT) [101]. By scanning a specimen using different energies and applying the knowledge about beam attenuation in the material, it is possible to combine information of both reconstructions in order to quantify the different materials of a component. Such integration belongs to a competitive sensor configuration application.

Furthermore, combining X-ray computed tomography with the design and components of industrial CMMs makes it possible to achieve an accuracy enabling CT being used in

industrial coordinate metrology. Bartscher et al. [102] developed a complementary integration system for RE. In their work, a fringe projection system was used to measure the outer surface of a cast cylinder, and CT was exploited to scan inner surface. Then all information was combined to achieve holistic geometrical measurement.

2.3.3.5. Commercial multi-sensor systems

Commercial multi-sensor CMMs are developed by using a combination of several sensors to provide higher precise or larger ranges of the measurements. Many CMM manufacturers, for example, Nikon, Hexagon, Werth Messtechnik, Zeiss, etc. [103], can provide the multisensory solutions. A commercial hybrid structured light measuring system with combinations of photogrammetric sensor and tactile probing is made by GOM Ltd. [104]. FARO Technologies Inc. develops a kind of hybrid laser and hard probe system, with a laser line and a trigger probe mounted on an articulated arm [31].

Some commercial CMMs integrate with other non-contact methods, such as computed tomography or fibre probe [103, 105, 106]. Additionally, multi-sensor systems based on tracker sensors [29], interferometry or photogrammetry [107] etc., are also available. However, the techniques and methods combining the different sensors in these systems are usually not published due to commercial purposes.

To the author's best knowledge, most of solutions combine the optical sensors with a tactile probe in a complementary configuration.

2.3.3.6. Data format conversion for the system integration in CAD/CAM environment

The measurement of multi-sensor system is not isolated and should be integrated with other activities for example PLM (Product Lifecycle Management). It is also an important issue to embed the measurement activity into the manufacturing process. The RE should also consider the integration problem because the measured point data which is used to reconstruct the CAD model needs to satisfy the design intent and specifications [10].

If each respective measuring system or software outputs different data formats, data format conversion is usually needed. The most common solution for the system integration is based on interface standards are specified with standard file formats. Many standards and neutral files are published for these purposes, such as IGES (Initial Graphics Exchange Specification), STEP (Standard for the Exchange of Product Model Data) and STL (Stereo Lithography or Standard Triangulation Language) etc. are used in this thesis for data fusion in CAD environment.

2.4. Summary

Multi-sensor integration has been shown to realize measurements with holistic, better representative and reliable information.

This chapter first presents an overview of classification for existing sensor technologies in dimensional measurement. Then three different sensing techniques commonly used in coordinate measurement - tactile probing, laser line scanning and fringe projection that will be implemented in this thesis, are discussed in detail considering their working principles, system models and calibration methods. The sensors' measurement accuracy and ranges as well as possible uncertainty contributions are also introduced. In general, touch tactile probing are considered to be more accurate compared with line scanning and fringe projection, except measuring soft surface or very thin wall when the object is affected by the tactile probe. This is not the case in this thesis.

Then the different multi-sensor configurations and general procedures for multi-data fusion are presented. The multi-sensor integration for surface digitization has also been introduced. Homogeneous optical sensor integration, inhomogeneous optical sensor integration, inhomogeneous tactile and optical probe integration, and some other system integration are surveyed. Commercial systems for multi-sensor systems in dimensional measurement are also described.

The following chapter will introduce a universal approach to integrate the coordinate system of a tactile probe and optical sensors.

Chapter 3

Coordinate Unification for Integrated Tactile-Optical Systems

3.1. Introduction

In Chapter 2, multi-sensor integration systems were shown to be able to provide more efficient solutions and better performances than single sensor based systems. The reduction of the lead time in RE, and the increased requirements in terms of accuracy as well as flexibility have resulted in a great deal of research effort aimed at developing and implementing combined systems based on cooperative integration of inhomogeneous sensors such as mechanical probes and optical systems, which have already been introduced in Section 2.3.3. However, a limitation of the prosed systems is that the integration of the optical system with the CMM generally takes place but is limited at the physical level, flexibility level and usability level. In most multi-sensor systems, a tactile sensor (such as stylus) and optical sensor (such as laser scanner) share the same probe fixed on the CMM arm and recalibration is needed after each change of sensor. Furthermore, some features, because of the existence of occlusion and diffuse reflection, are very difficult to scan using optical sensors. The views of optical sensors need to be changed several times to acquire global information. Then the flexibility of the system is greatly restricted because the optical sensors are fixed on the CMM arm.

When applying multi-sensor systems, different information sources (sensors) should be integrated in one common system. Bradley, et al. [91] and Xie, et al. [94] each presented a complementary sensor approach for reverse engineering; a touch probe and a laser sensor are attached to CMM $Z - axis$ arm and two sensors coordinates system can be referenced to the same one by measuring the same high precision ball bearing. A hybrid contact-optical coordinate measuring system was designed by Sladek, et al. [8], but the specific unification algorithm is not given. Huang, et al. [108] proposed an iterative registration and fusion method for multi-sensor calibration. It uses an iterative closest point (ICP) algorithm [60] to achieve surface fusion and Kalman filter [109] to obtain accurate surface registration. However the ICP method and its variants [110, 111] are more suitable for registration of data sets measured by the same or homogenous sensors (for example structured light and laser) which have similar resolution and accuracy. It also requires a sufficient number of coincident points from different data set to obtain an acceptable registration accuracy.

A flexible and effective approach for the integration of a CMM touch probe with optical sensors has been proposed in this thesis. A sphere-plate artefact is developed for unification of the hybrid system and it does not need the physical integration of optical sensors onto the CMM arm, but includes their combination at the measurement information level. This sphere-plate uses nine spheres rather than a traditional plate with three spheres to perform the geometric transformation. The system unification is achieved by measuring the sphere

calibration board and then measurement results from all of the optical sensors and the CMM probe head are combined into one set. This operation has to be done prior to any measurements, after the calibration of separate systems. It is carried out only once before a series of measurements and then the viewing position and orientation of the optical sensor can be adjusted to scan data from as many views as necessary to completely define the workpiece surface.

3.2. Geometric transform method for hybrid system unification

The optical scanner and the CMM tactile probe work in their own separate coordinate systems. If the integrated system is to produce useable results, these two coordinate systems have to be unified.

The same position surface data of a workpiece scanned from an integrated system can be seen as a kind of rigid body movement, so the geometric transformation method can be used to deal with coordinate unification. Since three non-collinear points can express a complete coordinate frame, data transformation of the two systems will be achieved simply with three different reference points and a three-point alignment coordinate transformation method can be used to deal with coordinate system unification. Therefore, the system unification problem for optical system and CMM tactile probe is converted to a coordinate transformation problem, the coordinates of multiple scan data from both systems can be transformed to one coordinate system. Coordinate transformation of 3D graphics includes geometric transformations of translation, proportion and rotation. The coordinate transform method by three points is derived by Mortenson and presented in [112].

3.3. Calibration board design

Since the error of each measuring reference point can be seen as equal weight value, the data fusion errors can be seen as average distributed errors [112]. It is very difficult to obtain the same single reference point from two different sensors (tactile and optical sensors in this case) without imposing strict & undesirable physical constraints on the system. This is compounded by the different measurement principles and methods of the two systems as well as different point cloud density. For this reason, most calibration systems use a geometric feature, rather than single point. If a reference feature point is taken as the calibration reference point every time, the possibility of occurrence of system error, human errors and accidental errors will increase greatly. Because three points can establish a coordinate, we can consider calculating the centroid of a standard calibration ball and then use the sphere centre coordinate as the datum reference point coordinate to achieve data fusion and reduce fusion errors.

The data fusion of 3D measurement data from different systems will be achieved through the alignment of three datum sphere centre points. In fact, the data fusion problem is, therefore, converted to a coordinate transformation problem. The transformation is determined by comparing the calculated coordinates of the centres of the calibration balls obtained in measurement conducted by the optical system.

An ball-plate calibration board (see Figure 3-1 (a)) with 9 spheres attached to it was created for data fusion of the hybrid system. Three spheres A_1, B_1 and C_1 form an approximate equilateral triangle and three groups of spheres form three small approximate equilateral triangles. The spheres are made of solid polypropylene with a matt finish and have good roundness and sphericity (see Figure 3-1 (b)). Their nominal diameter is Φ =25.4mm with a form error no greater than Φ =30 μm.
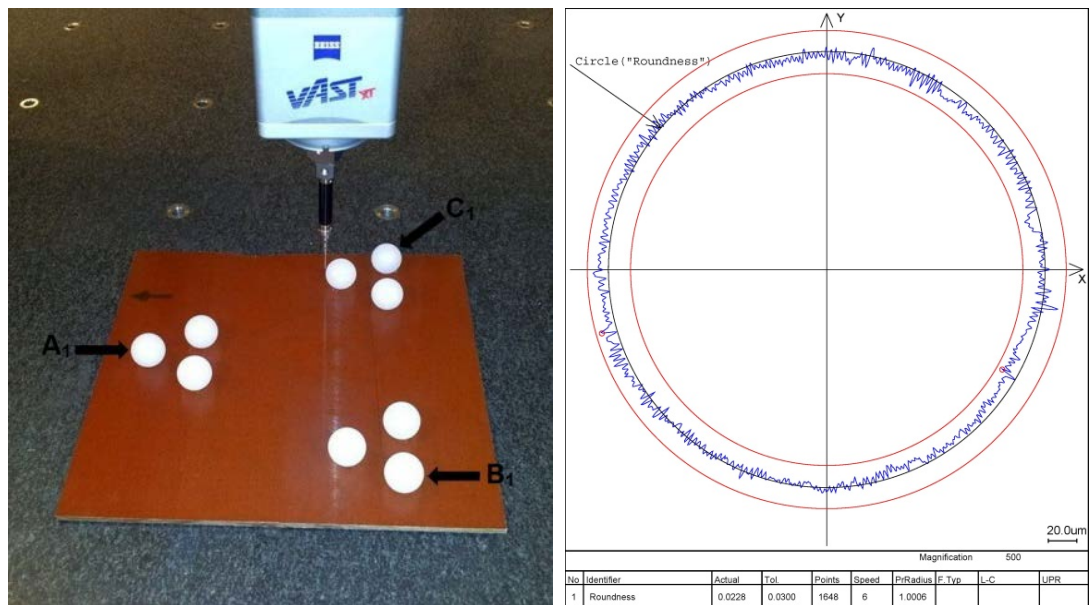
    (a) Calibration board on CMM   (b) Representative roundness of calibration balls

Figure 3-1: Spheres calibration board

3.4. Hybrid system configuration and calibration

3.4.1. Elements of the hybrid system

The integrated system (see Figure 3-2) was designed and manufactured with the following components as shown in Table 3-1:

Table 3-1: The components of the integrated system

A	High accuracy CMM	Zeiss PRISMO system - Maximum permissible error of length measurement $MPE_E = (1.9+L/300)$ µm (ISO 10360-2:2009)
B	Two CCD cameras	IDS UI-1485LE-M-GL, the CCD resolution is 2560(H)×1920(V), the dimension of a pixel is 2.2 µm×2.2 µm
C	Lens	Fujinon HF12,5SA-1/1,4 5 Megapixel C-Mount Lens, the focal length is 12.5 mm
D	Projector	Panasonic PT-LB60NTEA projector with 1,024×768 pixels
E	Planer calibration board (12W×9H×15 mm squares) for structured light scanner calibration and sphere-plate standard for unification of hybrid system	
F	FaroArm Quatum laser scanner	
G	PC Workstation	

(a) Zeiss CMM and structured light system   (b) FaroArm scanner

Figure 3-2: Elements of the integrated system

3.4.2. Hybrid system calibration

The CMM and optical scanners need to be calibrated separately before measurement. A master stylus was used for qualifying the CMM reference sphere and then the stylus system to be used during measurement must be qualified.

FlexScan3D PRO 3D scanning software [113] was used in the structured light scanner system to calibrate cameras and measure surface points. After calibration, the accuracy of the structured light system is up to 45 µm.

The calibration for the FaroArm portable coordinate measuring machine is divided into two stages: hard probe calibration and the laser line probe calibration. The manufacturer specification for the non-contact (laser) volumetric accuracy is 54 µm.

3.5. Proposed method and algorithm description

3.5.1. Proposed method

The optical sensor is often the main error source for an integrated tactile-optical coordinate system. For example in general laser line scanning is considered to be less accurate in comparison to touch trigger probing [4]. In order to further improve the measuring accuracy of datum-points we can consider using the centroids of spherical centres triangle rather than the original spherical centres triangle to unify two data sets of tactile and optical sensors. Therefore, we propose a "centroid of spherical centres" method was proposed for data unification of multi-sensor system; the specific steps are as follows:

Step 1: Measure the sphere-plate by CMM and optical scanners separately and calculate the spherical centre coordinates of each reference ball;

Step 2: Calculate of the centroid coordinates of spherical centres triangle measured by both systems separately;

Step 3: Use the centroids to form two new triangles and substitute their vertexes coordinates to Equation (3-6) to obtain R and T; and then use rotation R and translation T to unify two systems.

3.5.2. Mathematical model of 3D Cartesian coordinate transformation

Suppose two 3D Cartesian coordinates $O - XYZ$ and $O_T - X_T Y_T Z_T$, in space Cartesian coordinates transformation process, first the origin O is translated to another origin O_T, then two coordinates that have same origin can be transformed into the same one through three rotations. The transformation retaliation can be described by Equation (3-1):

$$\begin{bmatrix} x \\ y \\ z \end{bmatrix}_T = \begin{bmatrix} x_o \\ y_o \\ z_o \end{bmatrix} + kR \begin{bmatrix} x \\ y \\ z \end{bmatrix}_O \tag{3-1}$$

where $[x\ y\ z]_O^T$ is the coordinate in $O - XYZ$ and $[x\ y\ z]_T^T$ is the coordinate in $O_T - X_T Y_T Z_T$; $[x_o\ y_o\ z_o]^T$ is three translation parameters, R is rotation matrix and k is scale factor. α , β and γ are three rotation angles with respect to X , Y and $Z - axix$,respectively.

$$R = R_x(\alpha)R_y(\beta)R_z(\gamma) \tag{3-2}$$

$$R_x(\alpha) = \begin{bmatrix} 1 & 0 & 0 \\ 0 & \cos\alpha & -\sin\alpha \\ 0 & \sin\alpha & \cos\alpha \end{bmatrix} \tag{3-3}$$

$$R_y(\beta) = \begin{bmatrix} \cos\beta & 0 & \sin\beta \\ 0 & 1 & 0 \\ -\sin\beta & 0 & \cos\beta \end{bmatrix} \tag{3-4}$$

$$R_z(\gamma) = \begin{bmatrix} \cos\gamma & -\sin\gamma & 0 \\ \sin\gamma & \cos\gamma & 0 \\ 0 & 0 & 1 \end{bmatrix} \tag{3-5}$$

Then there are seven parameters x_o y_o z_o α β γ and k , so at least three pairs of coincidence points (nine known values) are needed to solve these parameters.

3.5.3. The principle of non-linear least squares

The Gauss-Newton algorithm [114] and Levenberg-Marquardt algorithm [115] have been widely used in solving non-linear least squares problems.

For an over-determined non-linear equation group,

$$\begin{bmatrix} f_1(x_1, x_2, \cdots, x_n) \\ f_2(x_1, x_2, \cdots, x_n) \\ \vdots \\ f_m(x_1, x_2, \cdots, x_n) \end{bmatrix} = 0\ (m > n) \tag{3-6}$$

which is $f(x) = 0$. It is usually converted $f(x)$ into quadratic functional form in the case where the existence of solutions cannot be determined.

Take function

$$\varphi(x) = \frac{1}{2} f(x)^T f(x) = \frac{1}{2} \sum_{i=1}^{m} f_i^2(x) \tag{3-7}$$

44

Then the minima $x*$ of function $\varphi(x)$ is the least squares solution of over-determined non-linear equations, which is

$$\varphi(x*) = \min_{x \in R^n} \varphi(x) = \min_{x \in R^n} \frac{1}{2} f(x)^T f(x) \tag{3-8}$$

Therefore, solving the over-determined non-linear equations problem is converted to a non-linear least squares problems. By the necessary conditions for the existence of extrema, if $f(x)$ is differentiable in the domain, then $g(x)$ is the gradient function of $\varphi(x)$, define $g(x) = \nabla \varphi(x) = 0$, which is

$$g(x) = \nabla \varphi(x) = \frac{1}{2} Df(x)^T f(x) = 0 \tag{3-9}$$

where $Df(x)^T$ is the Jacobian matrix,

$$Df(x)^T = \begin{bmatrix} \dfrac{\partial f_1}{\partial x_1} & \dfrac{\partial f_2}{\partial x_1} & \cdots & \dfrac{\partial f_m}{\partial x_1} \\ \dfrac{\partial f_1}{\partial x_2} & \dfrac{\partial f_2}{\partial x_2} & \cdots & \dfrac{\partial f_m}{\partial x_2} \\ \vdots & \vdots & & \vdots \\ \dfrac{\partial f_1}{\partial x_n} & \dfrac{\partial f_2}{\partial x_n} & \cdots & \dfrac{\partial f_m}{\partial x_n} \end{bmatrix} \tag{3-10}$$

First, linearize function $f(x)$, then its Taylor approximations at a point x^k is:

$$f(x) \doteq Df(x^k)(x - x^k) - f(x^k) = l_k(x^k) \tag{3-11}$$

Substituting Equation (3-11) into Equation (3-9), we have

$$x^{k+1} = x^k - \left[Df(x^k)^T Df(x^k) \right]^{-1} Df(x^k)^T f(x^k) \tag{3-12}$$

Equation (3-12) is the Gauss-Newton iterative method.

According to Equation (3-1), in this context Equation (3-6) can be rewritten as

$$
\left(\begin{bmatrix} x_1 \\ y_1 \\ z_1 \\ x_2 \\ y_2 \\ z_2 \\ x_3 \\ y_3 \\ z_3 \end{bmatrix}_T - \begin{bmatrix} x_o \\ y_o \\ z_o \\ x_o \\ y_o \\ z_o \\ x_o \\ y_o \\ z_o \end{bmatrix} - kR \begin{bmatrix} x_1 \\ y_1 \\ z_1 \\ x_2 \\ y_2 \\ z_2 \\ x_3 \\ y_3 \\ z_3 \end{bmatrix}_O \right) = 0
\qquad (3\text{-}13)
$$

The fitting function of spatial coordinate transformation, a seven parameters problem, is a matrix function. We can convert it into a non-linear over-determined equation group, take space coordinates of three reference points which contains the nine coordinate values to compose nine over-determined non-linear equations, then exploit the non-linear least squares method to solve these seven parameters.

The specific solving steps are as follows:

Step 1: The matrix function needed to be fitted is

$$
y = \mathop{F}_{9\times1}(x_1, x_2, x_3, x_4, x_5, x_6, x_7)
\qquad (3\text{-}14)
$$

Where the 3D Cartesian coordinate transformation model $F(x) = \Delta x + x_7 RX$, x_1, x_2, x_3 are three parameters of the translation matrix Δx separately; x_4, x_5, x_6 are the parameters of matrix R; x_7 is the scale factor; X is the 3D coordinates before transformation whereas y is the 3D coordinates after transformation.

Step 2: Set up

$$
G(x_1, x_2, x_3, x_4, x_5, x_6, x_7) = \sum_{9\times1} (F(x_1, x_2, x_3, x_4, x_5, x_6, x_7) - y)^2
\qquad (3\text{-}15)
$$

Step 3: Solve the minima of the multivariate function:

$$
g(x) = \nabla G(x) = 2f(x)(Df(x)^T) = 0
\qquad (3\text{-}16)
$$

The Gauss-Newton iterative method is exploited to solve (3-16). We select the initial value for the iteration, and stop the iteration when 1-norm of the vector difference of two adjacent seven parameters is smaller than a certain threshold (for example 10^{-6}) in the iterative process, then the optimal solution can be derived in terms of the least squares method.

3.6. Experiment results and error analysis

A sphere-plate artefact with nine spheres attached to it was created for unification of the hybrid system and a set of Matlab program was developed for the verification of this method. The multi-sensor systems are placed in a temperature-controlled room, typical of normal CMM applications, with the environmental temperature controlled to 20±1°C. The CMM, structured light scanning system and FaroArm laser scanner were calibrated separately, and then the sphere calibration board was measured by CMM touch trigger and both optical scanners separately (see Figure 3-3).
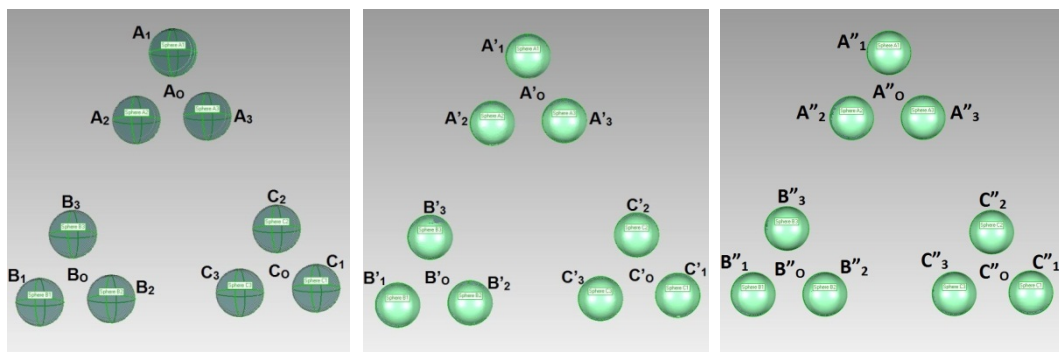
(a) Measured from CMM   (b) Measured from structured light   (c) Measured from FaroArm laser

Figure 3-3: Spheres surface and centres measured from tactile and optical systems

The coordinates of centres and the radius of the spheres measured by every method were calculated by the least squares best fit method. Table 3-2 shows the standard deviation of the residual distances of the measurement points and the radius of the spheres.

$$Std\ Dev = \sqrt{\frac{\sum_{i=1}^{n}(r_i-\overline{r})^2}{n-1}} \tag{3-17}$$

where r_i is the distance between each point and the centre, $\overline{r}$ is the radius of the spheres.

Table 3-2: The standard deviation on the centre and the radius of the spheres

Unit: mm	Std Dev			Radius			ΔR (VS CMM)	
	CMM	Structured	Faro Laser	CMM	Structured	Faro Laser	Structured	Faro Laser
A_1	3.7×10^{-3}	1.65×10^{-2}	1.34×10^{-2}	12.695	12.701	12.711	0.006	0.016
A_2	5.7×10^{-3}	1.67×10^{-2}	1.80×10^{-2}	12.688	12.704	12.691	0.016	0.003
A_3	4.7×10^{-3}	1.63×10^{-2}	1.34×10^{-2}	12.702	12.706	12.704	0.004	0.002
B_1	2.6×10^{-3}	1.55×10^{-2}	1.13×10^{-2}	12.698	12.728	12.707	0.030	0.009
B_2	6.1×10^{-3}	1.55×10^{-2}	1.30×10^{-2}	12.709	12.729	12.718	0.020	0.009
B_3	3.6×10^{-3}	1.60×10^{-2}	1.56×10^{-2}	12.698	12.727	12.711	0.029	0.013
C_1	3.2×10^{-3}	1.41×10^{-2}	1.29×10^{-2}	12.704	12.706	12.705	0.002	0.001
C_2	3.0×10^{-3}	1.53×10^{-2}	1.08×10^{-2}	12.695	12.696	12.703	0.001	0.008
C_3	4.5×10^{-3}	1.53×10^{-2}	1.28×10^{-2}	12.688	12.693	12.705	0.005	0.017
Average	3.7×10^{-3}	1.56×10^{-2}	1.34×10^{-2}	12.697	12.710	12.706	0.013	0.009

Taking the data measured from the CMM as the true values, because of its relatively high measuring accuracy, then comparing with the data obtained with both optical methods, it can be seen that the accuracy of the FaroArm laser scanner is slightly better than structured light system in this case.

First, three spherical centres A_1, B_1 and C_1 were selected as benchmark reference points to unify CMM and optical scanning systems, then centroids A_O, B_O and C_O were used to integrate the multi-sensor system.

Table 3-3 shows the coordinates of spherical centres of A_1, B_1 and C_1, which were measured by CMM and both optical scanners in their own local coordinates systems. For each sphere, 3,000 points therefore a total of 9,000 points, were used to obtain the fitting results.

Table 3-3: The coordinates of sphere centres

Unit: mm	CMM			Structured Light			FaroArm Laser		
	X	Y	Z	X	Y	Z	X	Y	Z
A_1	30.685	101.375	20.107	-28.700	-52.042	780.778	-87.255	-158.201	487.637
B_1	172.079	23.386	20.162	-167.538	-134.196	788.102	64.301	-158.385	543.295
C_1	169.797	184.615	20.296	-170.332	25.826	768.330	37.642	-158.521	384.334

Then 1,000 points for each sphere (total 9,000 points) were randomly selected to best-fit nine spheres. The calculated coordinates of the centroid of the spherical centres triangle are shown in Table 3-4.

Table 3-4: The coordinates of the centroids

Unit: mm	CMM			Structured Light			FaroArm Laser		
	X	Y	Z	X	Y	Z	X	Y	Z
A_O	55.890	100.907	19.998	-53.875	-53.315	780.607	-62.262	-158.370	484.267
B_O	159.085	43.736	20.150	-155.192	-113.544	785.843	48.373	-158.380	525.162
C_O	158.399	162.12	20.096	-158.245	3.937	771.455	29.798	-158.642	408.286

The translation vector T and rotation matrix R were solved by using above data, then the residuals of coordinates and root mean square of residuals were compared.

3.6.1. Coordinate unification of the CMM and structured light system

The non-linear least squares algorithm was exploited to solve seven parameters. It is worth mentioning that different initial values were selected for iteration (such as 0, 0, 0, 0, 0, 0, 1), the algorithm was found always to quickly converge (15-20 iterations for both methods) and obtain accurate least squares solutions even with a poor initial estimate, which shows the algorithm is robust and not sensitive to the initial values in this case.

The RMSR (root mean square of residuals) was used to validate the final unification accuracy.

$$RMSR = \sqrt{\frac{\sum_{i=1}^{n} (r_{iX}^2 + r_{iY}^2 + r_{iZ}^2)}{3n}} \qquad (3\text{-}18)$$

where r_{iX} is the residuals of ith datum point in the $X-axis$ direction, the rest may be deduced by analogy.

Table 3-5 shows the residuals of coordinates and RMSR after transformation from structured light system coordinate to CMM coordinate.

Table 3-5: The residuals & RMSR of coordinates (CMM & structured light)

Unit: mm	Datum point	Traditional Method			Datum point	Centroid Method		
		X	Y	Z		X	Y	Z
Residuals	A_1	0.006	0.003	-0.010	A_O	0.003	0.002	-0.005
	A_2	-0.008	0.009	-0.002	B_O	-0.004	0.004	-0.001
	A_3	0.001	-0.001	0.000	C_O	0.001	0.000	0.000
RMSR		5.675×10^{-3}				2.754×10^{-3}		

It can be seen that all the residuals of coordinate transformation by using centroid method are less than or equal the traditional method. The parameters solved by using the traditional three spheres method are:

$$R_T^S = \begin{bmatrix} -0.9993 & -0.0316 & 0.0191 \\ -0.0337 & 0.9920 & -0.1214 \\ -0.0151 & -0.1220 & -0.9924 \end{bmatrix}, T_T^S = \begin{bmatrix} 4.7879 \\ -149.1387 \\ 813.5296 \end{bmatrix}, k_T^S = 0.999973$$

Rotation angle $\alpha_1 = 173.023°$, $\beta_1 = 1.095°$, $\gamma_1 = 178.191°$.

The parameters are solved by using the centroid method are:

$$R_C^S = \begin{bmatrix} -0.9993 & -0.0316 & 0.0194 \\ -0.0338 & 0.9920 & -0.1215 \\ -0.0154 & -0.1221 & -0.9924 \end{bmatrix}, T_C^S = \begin{bmatrix} 4.7849 \\ -149.1008 \\ 813.5904 \end{bmatrix}, k_C^S = 0.999976$$

Rotation angle $\alpha_2 = 173.020°$, $\beta_2 = 1.114°$, $\gamma_2 = 178.187°$.

3.6.2. Coordinate unification of CMM and FaroArm laser scanner

Table 3-6 shows the residuals of coordinates and RMSR of residuals after transformation from the FaroArm laser coordinate system to the CMM coordinate system.

Table 3-6: The residuals & RMSR of coordinates (CMM & FaroArm laser)

Unit: mm	Datum point	Traditional Method			Datum point	Centroid Method		
		X	Y	Z		X	Y	Z
Residuals	A_1	0.015	-0.008	-0.007	A_O	0.007	-0.004	-0.003
	A_2	0.000	0.000	0.000	B_O	0.000	0.000	0.000
	A_3	0.000	0.012	-0.013	C_O	0.000	0.006	-0.006
RMSR		8.462×10^{-3}				4.045×10^{-3}		

It can be seen that all the residuals of coordinate transformation by using the new method are also better than or equal to the traditional method. The parameters solved by using the traditional three spheres method are:

$$R_T^L = \begin{bmatrix} 0.9885 & -0.1514 & 0.0023 \\ -0.0026 & -0.0017 & 1.0000 \\ -0.1514 & -0.9885 & -0.0021 \end{bmatrix}, T_T^L = \begin{bmatrix} -102.2929 \\ -178.0915 \\ 592.6479 \end{bmatrix}, k_T^L = 1.000047$$

Rotation angle $\alpha_3 = 90.120°$, $\beta_3 = 0.134°$, $\gamma_3 = 8.708°$.

The parameters solved by using the centroid method are:

$$R_C^L = \begin{bmatrix} 0.9885 & -0.1512 & 0.0023 \\ -0.0025 & -0.0018 & 1.0000 \\ -0.1512 & -0.9885 & -0.0021 \end{bmatrix}, T_C^L = \begin{bmatrix} -102.3066 \\ -178.0889 \\ 592.6370 \end{bmatrix}, k_C^L = 1.000035$$

Rotation angle $\alpha_4 = 90.123°$, $\beta_4 = 0.129°$, $\gamma_4 = 8.697°$.

The position and orientation of sphere plate are changed multiple times to ensure the process is robust when their physical setup is altered. The results of the repeated tests show no loss of accuracy.

Both experiments show that the residuals and the RMSR (see Table 3-5 and 3-6) greatly reduce after using the centroid method to the integrate tactile-optical coordinate system, and then the centroids can be used as datum-points for unification of the hybrid CMM and optical systems by optimisation. If the coordinates of all nine centres are used as input for the optimization, the unification RMSR of CMM with structured light and CMM with FaroArm laser is 2.2565×10^{-2} mm and 1.8684×10^{-2} mm, respectively. The RMSR for nine spheres give the poorest results in comparison with centroid or traditional three-sphere methods. This indicates that excessive imprecise datum-points (data measured from optical methods) are not conducive to improving the unification accuracy because of the induced inaccuracy in the optimisation, it also shows the effectiveness of the new centroid approach.

3.7. Summary

As a response to the requirements of more effective and accurate measurement, significant efforts are being devoted to the development of multi-sensor integration system in coordinate measurement. The coordinates of all subsystems have to be unified if the integrated system is to produce correct results.

The traditional three-point geometry transformation is a usual choice for coordinate transformation. While using three datum-points for coordinate transformation and unification of tactile-optical coordinate system, the question arises how to select optimal match datum-points from two different sensors. Then a new development in coordinate unification called the "centroid of spherical centres" method was introduced in this chapter, which can be used instead of the traditional method which uses three datum-points to perform the geometric transformation and unification of tactile and optical sensors. A sphere-plate artefact with nine spheres is developed for unification of the hybrid system and the sphere centre points, instead of just surface points, are exploited as datum-points. In this way some error contributions specific to each measuring method are averaged out, which renders the fusion of the systems more robust for practical cases.

For an integrated tactile-optical system the accuracy depends on both separate systems. However, the main error source comes from the optical sensors and the accuracy should be biased towards the contact method. In order to further improve the measuring accuracy of datum-points, the centroids of spherical centres triangle rather than original spherical centres triangle is used to unify the multi-sensor system. The same numbers of points are used to calculate and compare the residuals of coordinates for both methods. Then a set of own developed Matlab program was utilized for the verification of proposed method. The results shown that the "centroid of spherical centres" method is more accurate compared to the spherical centres method. The unification of CMM with a structured light system and a FaroArm laser scanner shows this novel approach is simple, convenient, efficient and robust. Both experimental results prove this novel method is more accurate than the traditional three spheres method. Different measuring devices do not need to be placed in the same workplace. The benefits of the proposed method are improved accuracy in coordinate unification, and robust response to initial estimate.

In the next chapter, this method will be used to unify the Zeiss PRISMO CMM coordinate system and Nikon LC15Dx laser scanning system.

Chapter 4

Reverse Engineering of Geometry Based on Multi-sensor System

4.1. Introduction

Reverse engineering is the process of creating a design model and a manufacturing database for an existing part or prototype. The applications of RE are redesigning existing workpieces/tools or prototype parts where the CAD model of parts are not available.

Ideally, a fully automatic RE system would exist that can make decisions, classifications and reconstructions etc. without any user interaction. However, to the author's knowledge, until now there are no efficient systems have been designed which would consistently fulfill this goal for workiece with complex geometry and freeform. There are several reasons. First, the parts to be scanned are imperfect, owing to manufacturing errors, any damage and abrasion in their usage. Furthermore, the point cloud data is inaccurate and noisy which is caused by measuring system, and sometimes is incomplete because of occlusion or shiny surface. Finally, the algorithms for processing of complex shapes are still not mature. For example, some small geometric features cannot be successfully extracted in the segmentation process, or cylinders are identified as parts of a revolution surface rather than cylinders. Therefore, it is important to have a priori global characterization of the shape to be reverse engineered, and to have a prior understanding of the measurement process at the present state-of-the-art.

When digitising an object, all surface geometry is captured including imperfections caused by the manufacturing process and any damage the part may have suffered as well as noise introduced by the measurement process. Typically, the part will be manually remodelled to capture the design intent and to disregard imperfections. There are some reasons for this. Firstly, modelling every single defect could be time consuming and therefore expensive. Secondly, one of the main goals of RE is to reconstruct a CAD model of the workpiece. Therefore the aim is to create a 'more perfect' part model representing true design intent rather than simply copying the product being investigated. This may require a detailed understanding of the function, depending on the part being modelled, because only then can the design intent be correctly interpreted.

4.2. Discrete Geometry Processing in Reverse Engineering

RE technology starts with a solid artefact and constructs a geometric model by mean of coordinate data derived from a measurement system in order to obtain a diversified and highly creative design. The core developing procedures of RE products include:

1) Derive the coordinate data related to the existing object model using a measurement system and construct the CAD model.
2) The constructed CAD model must be subjected to profile inspection, testing and correction.

3) The solid model of the RE workpiece can be rebuilt through moulding, sculpting, CNC (computer numerical control) machining or rapid prototyping (RP).

Motavalli [116] pointed out that RE is accomplished in three steps, including part digitisation, feature extraction, and CAD modelling. Part digitisation is the measurement process of the object model, and the measurement result is stored in a cloud of 2D or 3D coordinate points. Data processing based on RE involves the following operations:

- Data pre-processing
- Data registration
- Meshing
- Shape recognition and segmentation
- Model Reconstruction

Moreover, data format conversion is often required.

The classical workflow of RE of workpiece is shown in Figure 4-1.
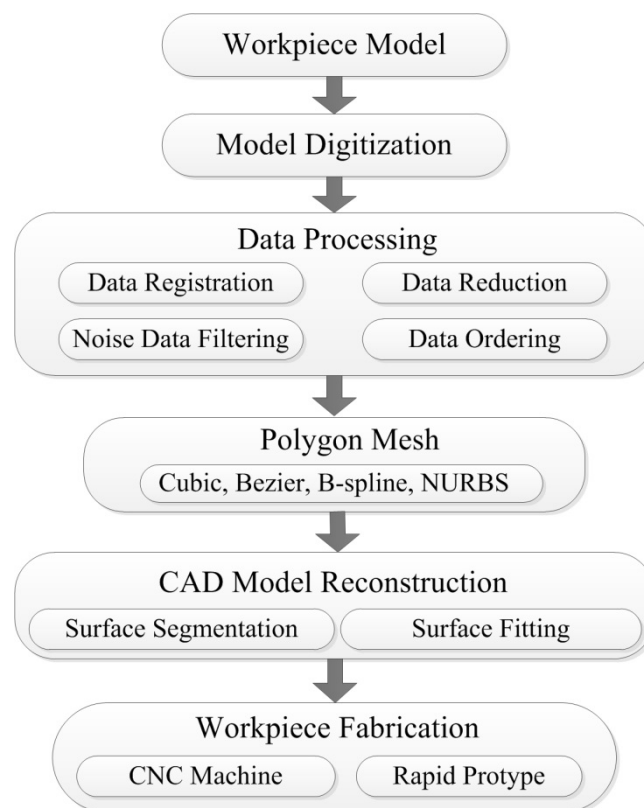
Figure 4-1: Flowchart for a RE workpiece

4.2.1. Point data pre-processing

At the first step the measured data typically is pre-processed at the necessary level of abstraction. Data pre-processing usually includes data filtering, data reduction, data ordering etc. as described in Section 2.3.2.

The part digitisation process of RE usually involves massive point cloud data. This is especially when the surfaces are digitized by optical methods, which often generate large amounts of redundant points and noisy points. If all data is used in surface construction, it usually takes a considerable time. Worse, the results may not replicate the original object model owing to the adverse effect of measurement noise. Hence, the foremost tasks in the processing of measurement data consist in the elimination of noise data and the reduction of measurement data.

The purpose of the data filtering is to eliminate noise points, while keep the physical surface features information unchanged. These motivations bring out a set of robust filtration techniques, most of them are presented in ISO 16610 [117]. Commonly used data filtering methods are Gaussian filtering [118], Averaging filtering [119] and Median filtering method [120], the filtering effects as shown in Figure 4-2 [121]. Gaussian method can better maintain the morphology of original data when performing filtering. Averaging filtration computes the statistical average of each point for the filtration of point cloud. Median method uses statistical mean values to filter point data, which makes this method be more suitable for the point cloud with relatively low accuracy. In general, the Gaussian filtration is used in this thesis for data filtration.
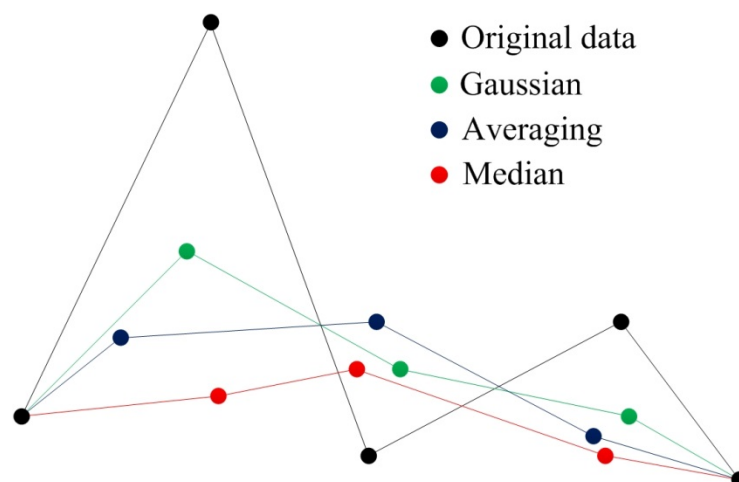
Figure 4-2: Three commonly used data filtering methods

Since not all data points measured by optical sensors are useful for the reconstruction of the final model, it is necessary to reduce the vast amount of point data while retaining the required feature. There have been a number of methods studied by several authors. Martin et al. [122] devised a uniform data reduction technique using the median filtering approach. Hamann [123] developed a data reduction method based on curvature. Points in nearly planar surface regions are preferentially removed. Lee et al. [59] proposed a non-uniform grids method to reduce the amount of scanned data. In thesis, curvature (Hamann) and uniform (Martin et al.) based methods are used for data reduction.

4.2.2. Multi-view data registration

Registration is one of the most important steps of data processing in RE. The point data acquired by multiple views are usually represented in their own coordinate systems. During the registration process, the measurement data captured in the respective coordinate system are aligned and transformed to one global coordinate system.

Methods that are commonly used to register multi-view data can be classified into four categories:

1) Applying a numerical algorithm. The transformation parameters of multi-view data include three rotations and three translations. They can be determined by minimizing the distance between corresponding points in different surfaces. The most representative one is the ICP (Iterative Closest Point) algorithm [60] and its variants [124-126]. Many of the difficulties inherent in feature based methods are overcome by these methods. However, according to the author's best knowledge, how to find the corresponding points has not yet been well solved. The ICP method also requires a sufficient number of conjugate points from different data set to obtain better registration accuracy.

2) Using fiducial markers [127, 128]. The markers can be planar or 3D and are usually adhered on or near the surface to be scanned. While the measuring sensor is taking point data from a specific view, the 3D coordinates of the markers within the view are obtained at the same time. The relative position and orientation of two data sets can be determined if three or more markers are visible in both views. This method is usually fast and reliable. However, apart from the manual preparation work before the measurement, the drawback of this strategy is that the areas covered by the markers cannot be digitized reliably. This problem is especially limiting when objects are small size or have abundant details. Moreover, adhering markers on the surface is even prohibited in some applications.

3) Employing other optical or magnetic devices. For example, a FARO Laser Tracker can be used to combine a camera and a laser tracker to track the targets fixed on the scanning

sensor and thereby determines the position and orientation of the sensor [31]. The optical/magnetic tracing devices can work with large volume objects and obtain good registration results. However, the auxiliary tracing devices are relatively heavy, cumbersome, and of high cost for many applications.

4) Exploiting mechanical devices like CMM arms [94], turntables [129] or multi-joint robotic arms [130]. In these solutions, either the sensor or the object to be measured is placed on the mechanical devices, whose movement can be strictly controlled. The movement parameters of the devices are used to automatically compute the geometric transformation in the measurements. This method works well for some applications, yet it is limited for measuring large objects. In addition, the use of extra mechanical devices unavoidably reduces the flexibility and portability of the measuring system, and the effect on measurement of each element must be well quantified.

4.2.3. Polyhedral surface generation

The scattered point sets are usually approximated to proper polyhedral surfaces in order to build the topology structures [131]. The polyhedral surfaces are composed of polygon meshes where the local neighbour information of each vertex can be found. The local neighbour information is required by most computations of normal vector or curvatures on the scattered point sets [10]. As the scattered point sets generated by optical sensors are usually noisy, unorganized or incomplete, there have been considerable techniques developed by many authors [132-136] for mesh generation of unorganized point sets. Among these methods, the method developed by Alliez, et al. [134] is one of the most popular methods for surface reconstruction of noisy defective point samples.

4.2.4. Shape recognition and segmentation

After a model is measured, the acquired point cloud data should be divided into several smooth regions for further processing, which is called the segmentation process. The segmentation process is used to group the initial model into a set of sub-components based on predefined criteria. Each of the segmented regions then has an appropriate, recognizable meaning [137].

According to different applications, the existing segmentation methods can be classified into two categories. The first category is aimed at grouping the more natural object model into pieces of meaningful regions based on the viewpoint of human cognition. Most of the segmentation methods in computer graphics, biological, medical and digital heritage applications are classified as this category. The second one is committed to segmenting partitioning the discrete model into patches and each patch can be fitted by a single,

mathematically analysable shape. The applications in mechanical engineering, especially in RE, belong to this category. For example, a mechanical part data set is segmented into data patches of planes, cylinders, spheres, etc., belongs to this category [10].

A segmentation that extracts the edges and partitions the 3D point data plays an important role in fitting surface patches and applying the measured data to the manufacturing process. In RE, the segmentation has the greatest effects on product development time and the quality of the final surface model [138]. Considerable research activities in shapes segmentation have been explored in recent years. The methods for segmenting 3D data in engineering applications can be generally classified into three types: edge-based, region-growing and hybrid-based [138].

The edge-based approaches [139-142] detect discontinuities in the surfaces that form the closed boundaries of components in the point data. Normal vectors and curvatures are commonly used to find the boundary points. Edge-based methods are developed and applied widely because they are simple and efficient. However, as the scanned data from measurement sensors (especially optical sensors) are generally noisy and unreliable in edge vicinities, finding edges is always unreliable as the computations of normal and higher-order derivatives are sensitive to the noise [9].

Region-growing methods [143-145], on the other hand, attempt to generate connected regions first, then proceed with segmentation by detecting continuous surfaces that have homogeneity or similar geometrical properties. In principle, region-based methods work on the global size of point data sets and so they are more robust to the noise than edge-based methods. However it generates less accurate surface models than those of the edge-based method and it is also difficult to modify the final model.

The hybrid approaches [138, 146, 147], combining the edge-based and region-based information, have then been developed to overcome the limitations involved in edge-based and region-based methods.

As the algorithms for segmentation are beyond this research work, the existing methods for data segmentation are implemented for the applications to RE in this thesis. The method used for data segmentation is introduced in Section 4.3.2.

4.2.5. Model Reconstruction

After the segmentation process, the original point set is divided into subsets which consist of a series of polygon mesh patches or labelled points belonging to a particular region. These subsets are needed to classify to what type of surface each subset of points belongs (e.g.

planar, sphere) and find that surface of the given type which is the best fit to those points in the given subset. The surfaces subsets can be broadly classified into two categories: geometric elements like planes, spheres, cylinders, cones; and freeform surfaces which can be modelled using parametric surfaces such as Bezier surfaces, Basis Splines (B-Splines) or Non Uniform Rational B-spline (NURBS) [9]. The CAD model of an object can be constructed by combining geometric primitives or parametric patches and their boundaries [148].

4.2.5.1. Surface representations

Varieties of surfaces are studied and used in geometric modelling. In general, the surfaces are classified as algebraic and parametric surfaces [149].

(1). Algebraic surfaces

Algebraic surfaces can be represented by an implicit equation in the form $f(x, y, z) = 0$ in 3D space [150]. The advantage of algebraic representation is that manipulating polynomials rather than arbitrary analytic functions is computationally more efficient. Another primary advantage of algebraic surfaces is their closure properties under modelling operations such as intersection, convolution, offset blending, etc. [149].

Quadratic surfaces are a subset of algebraic surfaces, which can be described by a general second-order equation in x, y and z. They can be represented by 10 coefficients (Equation (4-1)) or by a 4×4 symmetric coefficient matrix (Equation (4-2)) [151].

$$f(x, y, z) = Ax^2 + By^2 + Cz^2 + 2Exy + 2Fxz + 2Hyz + 2Gx + 2Jy + 2Kz + D = 0 \quad \text{(4-1)}$$

$$\begin{bmatrix} x & y & z & 1 \end{bmatrix} \begin{bmatrix} A & E & F & G \\ E & B & H & J \\ F & H & C & K \\ G & J & K & D \end{bmatrix} \begin{bmatrix} x \\ y \\ z \\ 1 \end{bmatrix} = 0 \quad \text{(4-2)}$$

There are two approaches for algebraic surface fitting, one by interpolation and the other by approximation. Interpolation is used when the function values at the measured points are known to a high precision. Different interpolation schemes are presented by Frank [152]. In approximation methods, the least square method (linear and nonlinear) is used to find the coefficient of the polynomial equation [153].

(2). Parametric surfaces

Parametric surfaces are those which are represented in terms of two parameters u and w. Such a representation consists of three functions $x = x(u, w)$, $y = y(u, w)$ and $z = z(u, w)$. Examples of these surfaces include Bezier' surfaces, B-spline surfaces, NURBS [149].

Bezier surfaces can be represented in a generic form as given by [154]:

$$p(u,w) = \sum_{i=0}^{m} \sum_{j=0}^{n} p_{i,j} B_{i,m}(u) B_{j,n}(w) \tag{4-3}$$

where $p_{i,j}$ are the vertices of the characteristics polyhedron that form an $(m+1) \times (n+1)$ array, $B_{i,m}$ and $B_{j,n}$ are the Bernstein polynomials. These are parametric surfaces with Bernstein polynomials as their basis functions. The surfaces possess a convex hull property and remain within the convex hull of the control points.

B-spline surfaces are also parametric surfaces with polynomials (instead of Bernstein polynomials) as their basis functions defined over a knot vector [155]. The knots are equidistant in the case of uniform B-splines while the distance is variable in the case of non-uniform splines.

NURBS use rational polynomials as their basis functions. A NURBS curve can be represented as [156]:

$$C(u) = \frac{\sum_{i=0}^{n} w_i P_i N_{i,p}(u)}{\sum_{i=0}^{n} w_i N_{i,p}(u)} \tag{4-4}$$

where p_i are the control points, w_i are the weights and $N_{i,p}$ are the normalized B-spline basis functions of degree p defined over a knot vector (a sequence of non-decreasing numbers):

$$U = \left\{ u_1, u_2, \cdots, u_{n+p+1} \right\} \tag{4-5}$$

A NURBS surface patch can be represented by [157]:

$$p(u,v) = \frac{\sum_{i=0}^{n}\sum_{j=0}^{m} w_{i,j} P_{i,j} N_{i,p}(u) N_{j,q}(v)}{\sum_{i=0}^{n}\sum_{j=0}^{m} w_{i,j} N_{i,p}(u) N_{j,q}(v)} \qquad (4\text{-}6)$$

where $P_{i,j}$ forms the control net, $w_{i,j}$ represent the weights, $N_{i,p}$ and $N_{j,q}$ are the normalized B-splines of degree p and q in the u and v directions defined over the knot vectors:

$$U = \left\{ u_1, u_2, \cdots, u_{n+p+1} \right\} \qquad (4\text{-}7)$$

$$V = \left\{ v_1, v_2, \cdots, v_{m+q+1} \right\} \qquad (4\text{-}8)$$

NURBS surfaces are defined in the parameter region $0 \le u \le 1$ and $0 \le v \le 1$ only and are undefined outside this region [158].

The algorithms for fitting parametric surfaces are divided into gridded and scattered data fitting methods. The least squares approach is the most commonly used technique for fitting these surfaces [149].

4.2.5.2. Boundary representation (B-rep) model creation

After direct segmentation, a set of disjoint regions is been produced, which include not only a series of analytic surfaces, but smooth internal curves as well. The purpose of the B-rep model creation phase is to create a consistent and contiguous model of vertices, edges and faces, where both the adjacency relationships between the constituent elements and the mathematical equations of underlying edge curves and surfaces are explicitly computed and stored [148]. To present a detailed uniform approach for the final B-rep model creation would be very difficult, so this description cannot contain all details, but the basic concepts and most import steps will be introduced.

(1). Constraint management

For finite surfaces which are defined over a bounding box with edges (surfaces that are finite), constraints need to be applied at the boundaries of the surfaces. While generating a solid model from measurements of an existing workpiece, the desired continuities can be obtained by introducing a new patch that would join the two existing surfaces with required continuity. The constrained reconstruction on Bezier' and NURBS patches with desired continuities is presented by Puntambekar, et al. [159]. Multiple patches were joined at the boundaries by

using C^0, G^1 and C^1 continuity. Both parametric and analytic surfaces are successfully joined at the boundaries with desired continuity.

(2). Surface extension

Parametric surfaces are finite surfaces and bounded by vertices and edges. When intersections need to be computed, extension of such surfaces may be required. When the underlying surfaces can be extended beyond the boundaries of their segmented regions, surface-surface intersections will provide proper edge curves, which need to be limited by two end vertices. In the case when intersection is not possible or not a true representation, blends might be inserted or the parameters of the surfaces adjusted to make them meet smoothly [9].

(3). Stitching

Creation of the complete topological structure can be achieved by stitching together the surfaces, edges and vertices. This is a quite straightforward process, since in the previous phases the consistency of the geometrical and topological entities has been established. Taking an edge loop of a given surface, the applied procedure guarantees that each real edge is shared by another edge of a neighbouring surface and the related end vertices are identical. Thus, taking all edges of the loops of given surfaces, all adjacent surfaces can be stitched together [160].

4.2.5.3. Blend reconstruction and further beautification

The blends can be reconstructed after the reconstruction of the primary surfaces. The best approximation to the appropriate radius of blends needs to be determined. Blend information is attached to the edges and incorporated into the B-rep model. Different methods for estimations of blend radii are thoroughly analysed in [161]. The iterative spine method and maximum ball approach are commonly used methods, both of them are efficient and numerically stable for blend approximation [160].

After a consistent B-rep model has been created, there are further tasks to make the representation better from an engineering point of view. A crucial step is the "beautification" of the final model [162]. In the presence of incomplete and noisy measured point data, the generated model is likely to be imperfect. The exclusion of very small edges and facets, filling of little holes, etc. are all important requirements for real-life CAD/CAM models. In addition, for artefacts that have many important geometric properties which represent essential information, such as symmetry, parallelism, orthogonality, concentricity, etc., such constraints may be imposed upon the model, but this should be done under careful consideration [9].

4.2.6. Reverse Engineering of sample workpiece

Figure 4-3 shows a typical workflow for RE of a sample part. The part is digitized by the structure light system that is introduced in Section 3.5. More detailed data processing and model reconstruction techniques based on multi-sensor technique will be discussed further in Chapter 5.

(a) Workpiece prototype
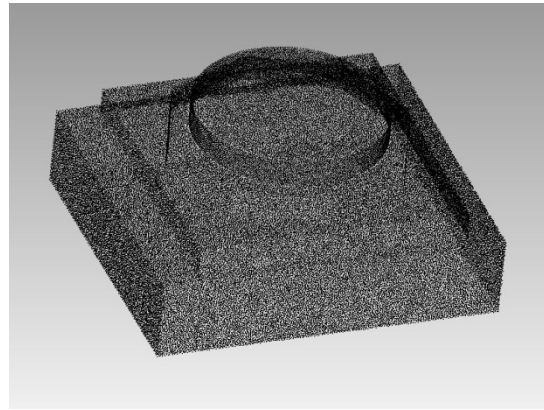
(b) Point cloud data

(c) Polyhedral model

(d) Surface segmentation and recognition
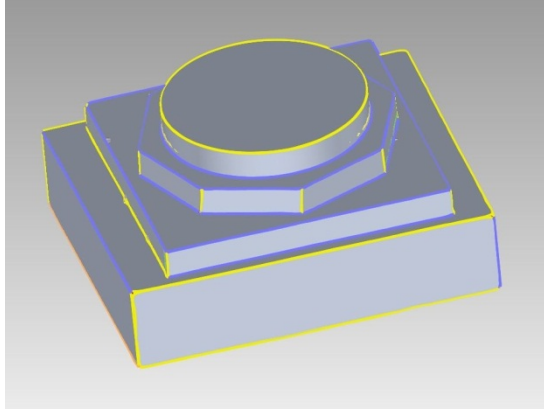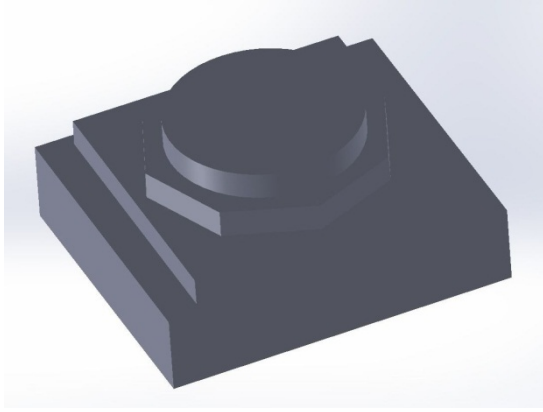
(e) Parametric surface   (f) CAD model reconstruction

Figure 4-3: RE of a sample part

4.3. Best-fit and compensation for geometric elements based on multi-sensor system

4.3.1. Related works in competitive multi-sensor integration

When using RE methods to reproduce a given shape, the tolerance distribution of the scanned part must be considered [9]. M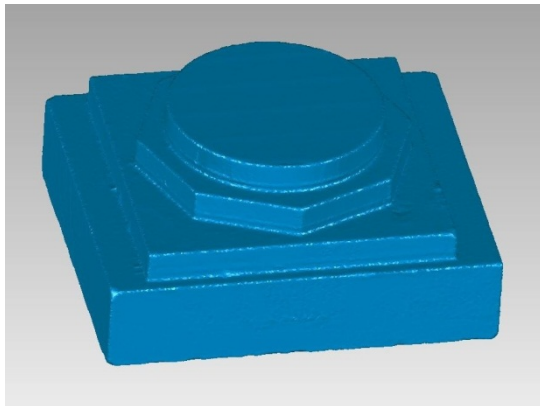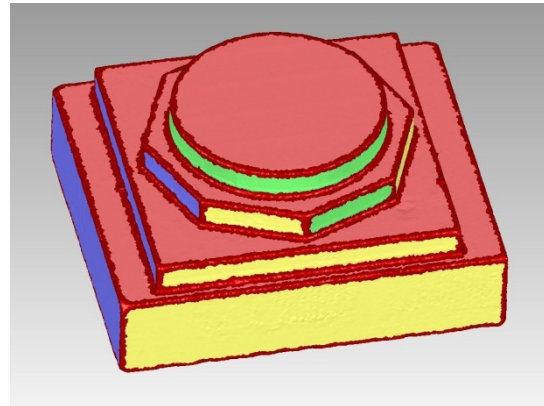ulti-sensor systems allow selecting discrete probing or scanning methods to measure part elements. The decision is often based on the principle that tight tolerance elements should be measured by high precision contact methods, while other more loose tolerance elements can be scanned via the faster optical techniques. Even though the integration of optical sensors and tactile probes, which are introduced in Section 2.3.3, has been explored in the past, such systems tend to be cooperative integration where optical sensors acquire the global shape information of objects to guide the touch probes for automatic point sensing.

Only limited research on competitive integration of hybrid contact-optical has been found. Huang and Qian [96] develop a dynamic approach for integrating a laser scanner and a touch probe to improve the measurement speed and quality. A part is first scanned by the laser scanner to capture the overall shape. It is then probed by a tactile sensor where the probing positions are determined dynamically to reduce the measurement uncertainty according to the scanned data. They use a Kalman filter to fuse the data and to incrementally update the surface model based on the dynamically probed points. Their approach can effectively save measurement time and be able to deal with shiny surfaces, but according to the experimental results displayed in the literature, this approach does not significantly improve accuracy of the fused data.

More recently, Bešić, et al. [97] introduce a method for improving the output of a CMM-mounted laser line scanner for measurement applications. The improvement is achieved by using a median filter to reduce the laser scanner's random error and by simultaneously combining with the reliable but slow tactile probing. The filtered point data is used to estimate the form deviation of the inspected elements while a few points obtained by the tactile probe are used to compensate for errors in the point cloud position. The shape of the part tested in the literature is relatively simple and only point cloud shift error caused by laser sensor is discussed and compensated. The introduced method is very intuitive and understandable. However, only a plane is considered in the literature and, because each point cloud data must be filtered before shifting, the usability is adversely affected.

In addition, current commercial systems or software often only focus on processing point data from individual sensors or techniques; the issue of where and how to effectively and efficiently improve the accuracy of fused data is still a challenge. In particular, to the author's best knowledge, no relevant research has provided a method to efficiently handle integrated measurement data in RE to use sparse accurate measurement information to improve the overall measurement accuracy for RE applications.

Therefore, this thesis proposes an effective competitive approach for using a tactile probe to compensate the data from a laser line scanner to perform accurate reverse engineering of geometric features. With the coordinate data acquired using the optical methods, intelligent feature recognition and segmentation algorithms can be exploited to extract the global surface information of the object. The tactile probe is used to re-measure the geometric features with a small number of sampling points and the obtained information can be subsequently used to compensate the point data patches which are measured by optical scanning system. Then the compensated point data can be exploited for accurate reverse engineering of a CAD model. Since the non-surface features that cannot be scanned by optical methods can be digitised by the tactile probe, this multi-sensor system is also a complementary configuration. The limitations of each measurement system are compensated by the other.

4.3.2. Least squares best fit geometric elements

After a part is scanned, the acquired point cloud data should be divided into several smooth regions for surface fitting purposes. This is called the segmentation process. Segmentation is the problem of grouping the points in the original dataset into subsets, each of which logically belong to a single primitive surface. Most commonly, segmentation has been viewed as a local-to-global aggregation problem with several similarity constraints employed to form a cohesive description in terms of geometric features. A segmentation that extracts the edges

and partitions the 3D point data plays an important role in fitting surface patches and applying the measured data to the RE process. Considerable research activities in shape segmentation have been explored in recent years, which have been introduced in Section 4.2.4. The data sets are segmented into point-based data patches or polygon-based data patches by using different methods. As the discrete point data is much easier to modify in comparison with polyhedral surface, this work only considers the segmentation methods that are able to generate the outputs for point-based data patches.

Woo et. al. [138] developed an octree approach for segmenting the scan data. First the 3D non-uniform grids are generated by calculating the normal of each point. Then points are assigned in the subdivided cells with different levels in size. The edge points are extracted by selecting the points contained in the small-sized cells. Finally the segmented point-based data patches are obtained after these edge points have been removed. This method is able to effectively extract edge neighbourhood points and group data points and was therefore selected for performing the data segmentation in this thesis.

After the segmentation process, the original point set is divided into subsets which can be broadly classified into two categories: geometric elements and freeform surfaces. The algorithms for least squares best fit of various geometric elements have been studied by several authors [115, 153, 163]. The various geometries that are used to reconstruct a CAD model for RE applications and studied in this thesis are planes, spheres, cylinders and cones.

4.3.2.1. Optimization algorithm

Consider a function

$$E(u) = \sum_{i=1}^{n} d_i^2(u) \tag{4-9}$$

which has to be minimized with respect to the parameters $u = (u_1, \cdots, u_n)^T$. Here d_i represents the distance of the data point to the geometric element parameterized by u. In most cases sufficient measuring points will be taken, therefore we have $m \gg n$.

(1). Linear least squares

For linear geometries (for example lines and planes), each d_i is a linear function of the parameters, so that the equation in terms of exist constants a_{ij} and b_i can be written as

$$d_i = a_{i1}u_1 + \cdots + a_{in}u_n - b_i \tag{4-10}$$

Our objective is to make E take its minimum value. This target can be expressed as a system of equations of m linear equations in the n unknowns u. These equations can be rewritten as matrix form

$$Au = b \tag{4-11}$$

where A is the matrix whose $(i, j)th$ element is a_{ij} and b is the column vector whose ith element is b_i. In general $m \gg n$, so we are unable to satisfy all the equations simultaneously. Both sides of Equation (4-11) left multiply by A^T, we can obtain

$$A^T Au = A^T b \tag{4-12}$$

Equation (4-12) is called as normal equation. It provides the solution for u as

$$u = (A^T A)^{-1} A^T b \tag{4-13}$$

In most cases least squares solution of u can be solved by Equation (4-13).

(2). Gauss-Newton algorithm

For nonlinear geometries (such as spheres, cylinders and cones), the functions d_i are nonlinear functions of parameters. For the nonlinear problem, equations for u similar to Equation (4-13) can be mathematically derived. However, to solve such a system we still require an iterative type of algorithm to solve nonlinear least squares model. The reason is the linear method given in Equation (4-13) only provides a coarse approximation. According to our experimental results, for accurate data (such as data measured by touch trigger probe), this model should give a best fit sphere which is very close to the result according to the full nonlinear model; but for less accurate data such as that measured by the laser sensor, there will be a relatively large fitting error between two methods. Therefore, the linear method can be used to generate good initial estimates for the full nonlinear model.

The Levenberg-Marquardt algorithm and Gauss-Newton algorithm are well-known numerical methods and have been widely used in solving non-linear least squares problems, as discussed in Chapter 3. In this thesis, the Gauss-Newton method is used to find the minimum of the sum of squares $E(u)$. Assuming there is one initial estimate $u*$ for the solution u, to solve a linear least squares system of the form

$$Jp = -d \tag{4-14}$$

Where J is the $m \times n$ Jacobian matrix whose ith row is the gradient of d_i with respect to the parameters u

$$J_{ij} = \frac{\partial d_i}{\partial u_j} \tag{4-15}$$

It is evaluated at u , and the ith component of d is $d_i(u)$. The parameter is updated as

$$u := u + p \tag{4-16}$$

Steps of Newton's algorithm are repeated until it reaches a convergent point.

(3). Initial estimates

Some good initial estimates are usually required when using the Levenberg-Marquardt or Gauss-Newton algorithms to find the solution of $E(u)$. If the estimate $u*$ is poor the subsequent estimate may be worse, which is called divergence. If the data is very inaccurate, then the algorithm may take many iterations to converge or even stick in a local optimum solutions. In some extreme cases, the Jacobian matrix J will even become rank deficient and the system (Equation 4-14) will not have a well-defined solution. Therefore, good starting values and reasonably accurate data are very necessary for algorithm fast convergence and obtaining the global optimal solution. The least squares best fit geometric elements algorithms are fully detailed by Forbes [153], his algorithms are exploited as fitting methods, and the method to find initial estimates is discussed.

4.3.2.2. Least squares best fit plane

(1). Parameterization

A space plane can be specified by a point (x_o, y_o, z_o) on the plane and the direction cosines (a, b, c) of the normal to the plane.

$$a(x - x_o) + b(y - y_o) + c(z - z_o) = 0 \tag{4-17}$$

x_o, y_o, z_o, a, b and c are the desired parameters.

(2). Algorithm description

When we have n points (x_i, y_i, z_i), where $n \geq 3$, the best fit plane should pass through the centroid $(\bar{x}, \bar{y}, \bar{z})$ of the data and the direction cosines also have to be found. For this, (a, b, c) is the eigenvector associated with the smallest eigenvalue of

$$B = A^T A \tag{4-18}$$

1) Find the average of the points (x_i, y_i, z_i)

$$\begin{aligned} \bar{x} &= \sum x_i / n \\ \bar{y} &= \sum y_i / n \\ \bar{z} &= \sum z_i / n \end{aligned} \tag{4-19}$$

2) From the matrix A with its first column is $x_i - \bar{x}$, second column $y_i - \bar{y}$ and third column $z_i - \bar{z}$;

3) Solve A by singular value decomposition (SVD) and choose the singular vector (a, b, c) corresponding to the smallest singular value.

4.3.2.3. Least squares sphere

(1). Parameterization

A sphere is specified by its centre (x_o, y_o, z_o) and radius, r. Any point (x_i, y_i, z_i) on the sphere satisfies the equation

$$(x - x_o)^2 + (y - y_o)^2 + (z - z_o)^2 = r^2 \tag{4-20}$$

Equation (4-20) can be simplified as

$$x^2 + y^2 + z^2 - ax - ay - cz + \rho = 0 \tag{4-21}$$

where $a = 2x_o$, $b = 2y_o$, $c = 2z_o$ and $\rho = x_o^2 + y_o^2 + z_o^2 - r^2$.

a, b, c and ρ are the desired parameters.

(2). Initial estimates

When we have n points (x_i, y_i, z_i), where $n \geq 4$, the Equation (4-21) can be written as matrix form

$$\begin{bmatrix} x_i & y_i & z_i & -1 \\ \vdots & \vdots & \vdots & \vdots \\ x_n & y_n & z_n & -1 \end{bmatrix} \begin{bmatrix} a \\ b \\ c \\ \rho \end{bmatrix} = \begin{bmatrix} x_1^2 + y_1^2 + z_1^2 \\ \vdots \\ x_n^2 + y_n^2 + z_n^2 \end{bmatrix} \tag{4-22}$$

Both sides of Equation (4-22) are left multiplied by $\begin{bmatrix} x_i & y_i & z_i & -1 \\ \vdots & \vdots & \vdots & \vdots \\ x_n & y_n & z_n & -1 \end{bmatrix}^T$ and simplified. Using this,

we can obtain

$$\begin{bmatrix} a \\ b \\ c \\ \rho \end{bmatrix} = \begin{bmatrix} \sum x_i^2 & \sum x_i y_i & \sum x_i z_i & -\sum x_i \\ \sum x_i y_i & \sum y_i^2 & \sum y_i z_i & -\sum y_i \\ \sum x_i z_i & \sum y_i z_i & \sum z_i^2 & -\sum z_i \\ -\sum x_i & -\sum y_i & -\sum z_i & n \end{bmatrix}^{-1} \begin{bmatrix} \sum x_i (x_i^2 + y_i^2 + z_i^2) \\ \sum y_i (x_i^2 + y_i^2 + z_i^2) \\ \sum z_i (x_i^2 + y_i^2 + z_i^2) \\ -\sum (x_i^2 + y_i^2 + z_i^2) \end{bmatrix} \tag{4-23}$$

where $x_o = \dfrac{a}{2}$, $y_o = \dfrac{b}{2}$, $z_o = \dfrac{c}{2}$ and $r = \sqrt{a^2 + b^2 + c^2 - \rho}$. The obtained parameters via this

model are used as initial estimates for the full nonlinear model.

(3). Algorithm description

1) Distance equation

$$d_i = r_i - r \tag{4-24}$$

where $r_i = \sqrt{(x_i - x_o)^2 + (y_i - y_o)^2 + (z_i - z_o)^2}$.

2) Objective function

$$J(x_o, y_o, z_o, r) = \sum (r_i - r)^2 \tag{4-25}$$

3) Derivatives

$$\frac{\partial d_i}{\partial x_o} = \frac{-(x_i - x_o)}{r_i}$$

$$\frac{\partial d_i}{\partial y_o} = \frac{-(y_i - y_o)}{r_i}$$

$$\frac{\partial d_i}{\partial z_o} = \frac{-(z_i - z_o)}{r_i}$$ (4-26)

$$\frac{\partial d_i}{\partial r} = -1$$

4.3.2.4. Gauss-Newton strategy for cylinders and cones

Both a cylinder and cone require an axis, for example a space line, to be parameterized. Any line can be specified by giving a point (x_o, y_o, z_o) on the line and direction cosine (a, b, c), which constraint is $a^2 + b^2 + c^2 = 1$. So it requires six parameters to describe a line. The distance from any point (x_i, y_i, z_i) to the axis is found from

$$d_i = \frac{\sqrt{u_i^2 + v_i^2 + w_i^2}}{\sqrt{a^2 + b^2 + c^2}}$$ (4-27)

where

$$u_i = c(y_i - y_o) - b(z_i - z_o)$$
$$v_i = a(z_i - z_o) - c(x_i - x_o)$$
$$w_i = b(x_i - x_o) - a(y_i - y_o)$$

Equation (4-27) is quite complicated for an optimisation routine. If we implement a Gauss-Newton algorithm, the derivatives of this distance with respect to the parameters have to be found, which will give rise to rather complex expressions and take a significant amount of computing time. However, if the axis is exactly vertical and passes though the origin, then all of the expressions become vastly simplified. To simplify computations, a copy of data is translated and rotated so that the point (x_o, y_o, z_o) is at the origin of the coordinate system and the direction cosines are aligned with the $Z - axis$ before each iteration.

First, the data is translated so that the point on the axis is at the origin.

$$x_i = x_i - x_o$$
$$y_i = y_i - y_o$$ (4-28)
$$z_i = z_i - z_o$$

Then, the data is rotated so that the axis is along the Z axis. The rotation matrix used to rotate the axis about the $X - axis$ is given by

$$U_1 = \begin{bmatrix} 1 & 0 & 0 \\ 0 & \dfrac{c}{\sqrt{b^2+c^2}} & \dfrac{-b}{\sqrt{b^2+c^2}} \\ 0 & \dfrac{b}{\sqrt{b^2+c^2}} & \dfrac{c}{\sqrt{b^2+c^2}} \end{bmatrix}$$

(4-29)

The rotation matrix for rotation about the $Y - axis$ is

$$U_2 = \begin{bmatrix} \dfrac{b^2+c^2}{a^2+b^2+c^2} & 0 & \dfrac{-a}{a^2+b^2+c^2} \\ 0 & 1 & 0 \\ \dfrac{a}{a^2+b^2+c^2} & 0 & \dfrac{b^2+c^2}{a^2+b^2+c^2} \end{bmatrix}$$

(4-30)

We can rotate the data by applying the matrix $U = U_1 \times U_2$ to align the cylinder or cone along the $Z - axis$ (see Figure 4-4).
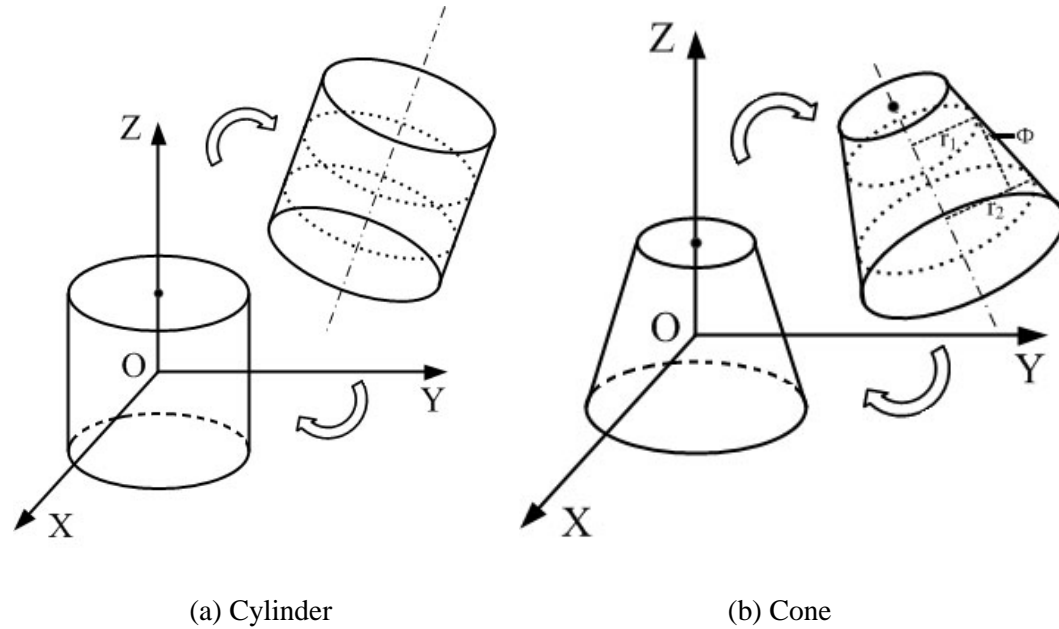

(a) Cylinder   (b) Cone

Figure 4-4: Points data translation and rotation

The iterative Gauss-Newton algorithm for cylinder and cone follows these steps:

1) Translating the data so that the initial estimate point (x_o, y_o, z_o) lies at the origin;

2) Rotation to align the axis of cylinder or cone along the $Z-axis$;

3) Computing increments of the direction cosines, point on the axis and radius (cylinder) or apex angle (cone);

4) Inverse rotation and translation transformations to the old coordinate system;

5) Updating previous values with current increments to determine the new position and orientation of the axis;

6) Checking for convergence. If not converged, then go back to step 1.

4.3.2.5. Least squares cylinder

(1). Parameterization

A cylinder can be specified by a point (x_o, y_o, z_o) on its axis; a vector (a, b, c) pointing along the axis and its radius, r.

Following Section 4.3.2.4, for a near vertical axis, we can set $c = 1$. Also, by knowing x_o and y_o, then z_o can be determined as

$$z_o = -ax_o - by_o \tag{4-31}$$

(2). Initial estimates

From Equation (4-27), any point (x_i, y_i, z_i) on the cylinder satisfies the equation

$$r = \frac{\sqrt{u_i^2 + v_i^2 + w_i^2}}{\sqrt{a^2 + b^2 + c^2}} \tag{4-32}$$

The Equation (4-32) is simplified; we can fit a general quadric

$$Ax^2 + By^2 + Cz^2 + Dxy + Exz + Fyz + Gx + Hy + Iz + J = 0 \tag{4-33}$$

where

$$A = (b^2 + c^2)$$

$$B = (a^2 + c^2)$$

$$C = (a^2 + c^2)$$

$$D = -2ab$$

$$E = -2ac$$

$$F = -2bc$$

$$G = -2(b^2 + c^2)x_o + 2aby_o + 2acz_o$$

$$H = -2(a^2 + c^2)y_o + 2abx_o + 2bcz_o$$

$$I = -2(b^2 + a^2)z_o + 2acx_o + 2bcy_o$$

$$J = (b^2 + c^2)x_o^2 + (a^2 + c^2)y_o^2 + (b^2 + a^2)z_o^2 - 2bcy_o z_o - 2acz_o x_o - 2abx_o y_o - r^2$$

Then initial estimates problem for cylinder can be posed as a liner least squares or eigenvalue problem. A minimum of nine coordinate points is needed for this.

(3). Algorithm description

1) Distance equation

$$d_i = r_i - r \qquad (4\text{-}34)$$

where r_i is defined by Equation (4-32).

2) Objective function

$$J(x_o, y_o, z_o, a, b, c, r) = \sum (r_i - r)^2 \qquad (4\text{-}35)$$

3) Normalization

$$(a, b, c) \leftarrow (a, b, c) / \sqrt{a^2 + b^2 + c^2}$$

$$(x_o, y_o, z_o) \leftarrow (\text{point on axis closet to origin})$$

4) Derivatives

After translation and rotation of data set, parameters x_o, y_o, a and b approach 0, then r_i

simplifies to $r_i = \sqrt{x_i^2 + y_i^2}$.

$$\frac{\partial d_i}{\partial x_o} = \frac{-x_i}{r_i}$$

$$\frac{\partial d_i}{\partial y_o} = \frac{-y_i}{r_i}$$

$$\frac{\partial d_i}{\partial a} = \frac{-x_i z_i}{r_i} \qquad (4\text{-}36)$$

$$\frac{\partial d_i}{\partial b} = \frac{-y_i z_i}{r_i}$$

$$\frac{\partial d_i}{\partial r} = -1$$

4.2.3.6. Least squares cone

(1). Parameterization

A cone can be specified by a point (x_o, y_o, z_o) on its axis; a vector (a,b,c) pointing along the axis and the apex semi-angle ϕ.

For a nearly vertical cone, we set $c = 1$ and then axis $z_o = -ax_o - by_o$.

(2). Initial estimates

Two methods are used to obtain initial estimates for cone fitting: normal vector based method and geometric method.

i) Normal vector based method

The normal vector based method is usually exploited to process dense point cloud data. The normal vector is a local geometric property of a 3D surface and specific to a given point. Many studies have been undertaken for reliable estimation of normal vector from discrete point data, by smooth parametric local surface association [139, 164] or by generating polyhedral surface [138, 140].

Let $n = (n_x, n_y, n_z)$ be the surface normal vector of a point on the cone (see Figure 4-5(a)), φ is the angle between n and axis vector (a,b,c). Then ϕ and φ is complementary, that is $\phi + \varphi = \pi / 2$. We have:

$$n_i \cdot v = h \quad (i = 1, \cdots, n) \qquad (4\text{-}37)$$

where $n_i = (n_{xi}, n_{yi}, n_{zi})^T$, $v = (a,b,c)^T$, $h = \cos\varphi$.

If Equation (4-37) is represented in matrix form, we have

$$Nv = H \tag{4-38}$$

where

$$N = \begin{pmatrix} n_{x1} & n_{y1} & n_{z1} \\ \vdots & \vdots & \vdots \\ n_{xn} & n_{yn} & n_{zn} \end{pmatrix}$$

$$H = (h \cdots h)$$

Then axis vector v and h can be solved by minimizing $\|Nv - H\|_2$, $\phi = \pi/2 - \arccos h$.

ii) Geometric method

The geometric method is quite straightforward. The tough trigger probe is operated on a CMM to scan two circles perpendicular to the cone axis (see Figure 4-5 (b)). By least squares best fitting both 3D circles, we can have their centres C_1, C_2 and radii r_1, r_2. l is the distance between C_1 and C_2. Then axis of cone can be determined by C_1 and C_2, ϕ can be solved by

$$\phi = \arctan \frac{r_2 - r_1}{l} \tag{4-39}$$

(3). Algorithm description

1) Specify t as the distance equation from the point (x_o, y_o, z_o) to the cone surface, then the distance from a point (x_i, y_i, z_i) to the cone is found from

$$d_i = e_i \cos\phi + f_i \sin\phi - t \tag{4-40}$$

where e_i is the distance from (x_i, y_i, z_i) to the line defined by (x_o, y_o, z_o) and (a,b,c); and f_i is the distance from (x_i, y_i, z_i) to the plane specified by (x_o, y_o, z_o) and (a,b,c) (see Figure 4-5 (b)).
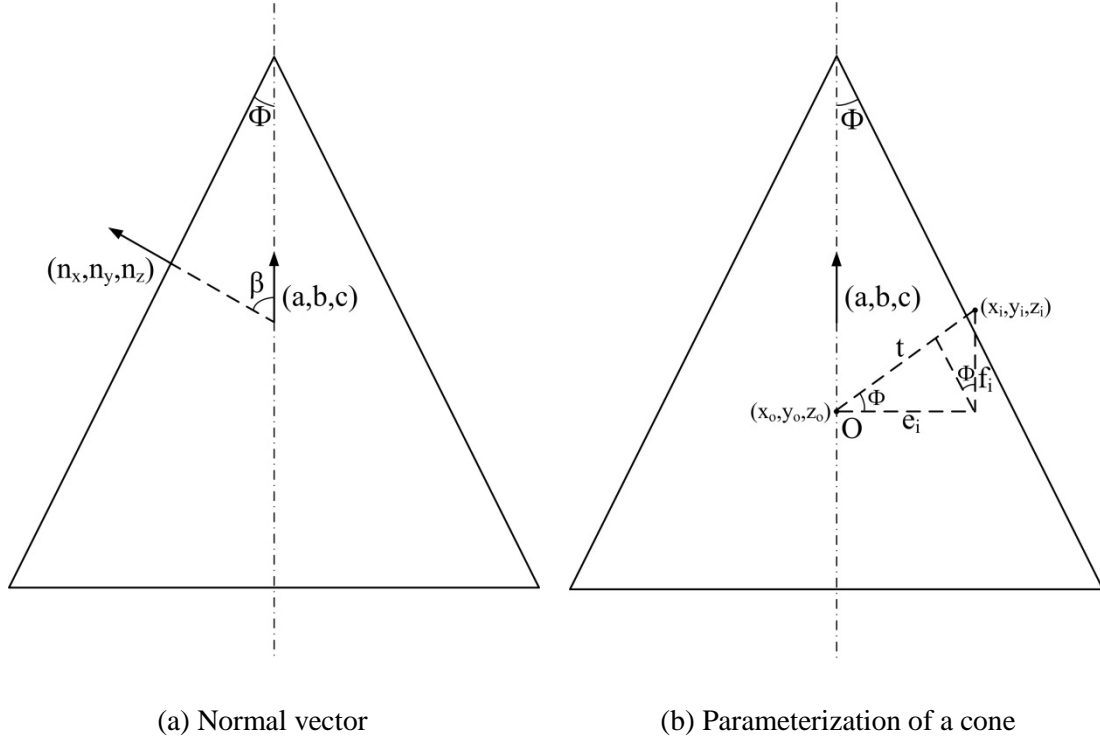
(a) Normal vector	(b) Parameterization of a cone

Figure 4-5: Cone fitting

After translation and rotation of the data set, parameters x_o, y_o, a and b approach 0, then e_i, f_i and r_i can be simplified to

$$
\begin{aligned}
e_i &= r_i \\
r_i &= \sqrt{x_i^2 + y_i^2} \\
f_i &= z_i
\end{aligned}
\tag{4-41}
$$

2) Objective function

$$
J(x_o, y_o, z_o, a, b, c, t, \phi) = \sum (e_i \cos\phi + f_i \sin\phi - t)^2
\tag{4-42}
$$

3) Normalization

$$
(a,b,c) \leftarrow (a,b,c) / \sqrt{a^2 + b^2 + c^2}
$$

$$
(x_o, y_o, z_o) \leftarrow (\text{point on axis closet to origin})
$$

$$
(0 < \phi < \pi/2), \text{ if } \phi > \pi/2 \text{ then } \phi \leftarrow \pi - \phi
$$

$$
\text{if } t < 0 \text{ then } (t \leftarrow -t; (a,b,c) \leftarrow -(a,b,c))
$$

4) Derivatives

$$\frac{\partial d_i}{\partial x_o} = \frac{-x_i \cos\phi}{r_i}$$

$$\frac{\partial d_i}{\partial y_o} = \frac{-y_i \cos\phi}{r_i}$$

$$\frac{\partial d_i}{\partial a} = \frac{-x_i w_i}{r_i}$$

$$\frac{\partial d_i}{\partial b} = \frac{-y_i w_i}{r_i} \qquad\qquad (4\text{-}43)$$

$$\frac{\partial d_i}{\partial \phi} = \frac{w_i}{2}$$

$$\frac{\partial d_i}{\partial t} = -1$$

$$w_i = z_i \cos(\phi) - r_i \sin(\phi)$$

4.3.3. Description of the proposed method

After multi-sensor coordinate system calibration and coordinate system unification, the optical scanner and tactile probe measure in nominally the same absolute coordinate system. However, two data sets measured by different sensors are unlikely to coincide absolutely, which means there will be a measurement difference between the tactile and optical sensor. The final aim of RE is to obtain a comprehensive, accurate CAD reconstruction model. To achieve this goal, a data compensation method is proposed to enhance the measurement accuracy of the point cloud data from the optical scanner. The proposed method is targeted at manufacturing problems where a reverse engineered model with accuracy better than 50 micrometres is needed. Naturally, the scanned data points must be representative of the geometric elements concerned.

4.3.3.1. Proposed method

After data segmentation, the data points are grouped into two types of data sets: geometric elements and freeform surfaces. The elements which include planes, spheres, cylinders and cones can represent 85% of machine objects [165]. Due to their simple mathematical description and ability to model a large percentage of manufacture objects, they are widely used in various modelling systems [166, 167]. In RE, the accuracy of final CAD model depends on the measured point data. As the discrete point data is much easier to modify in comparison with polyhedral surface [138], a small amount of discrete point data measured by the high accuracy, but relatively slow tactile probe, can be used to compensate the densely

scanned data patches that have been measured by the fast, but relatively low accuracy optical method. The specific method follows these logical steps:

1) Use the laser scanner to digitise the entire surface of part; and then exploit a segmentation algorithm, as described in Section 4.3.2, to group the point data patches each belonging to a different surface patches; these data patches will be compensated in Step 3;

2) Use the tactile probe to re-measure tight toleranced geometric features with a small number of points to minimise the temporal cost. Then use the least squares method to best fit these geometric elements to derive the parameters based on mathematical and numerical principles;

3) Substitute the x and y coordinates of each point measured by the laser scanner into the parametric equations (Section 4.3.2), then the new z coordinate can be updated. Use the x, y and new z coordinates as new point data coordinates to build point data sets. Then the compensated data sets are exploited to reconstruct a CAD model.

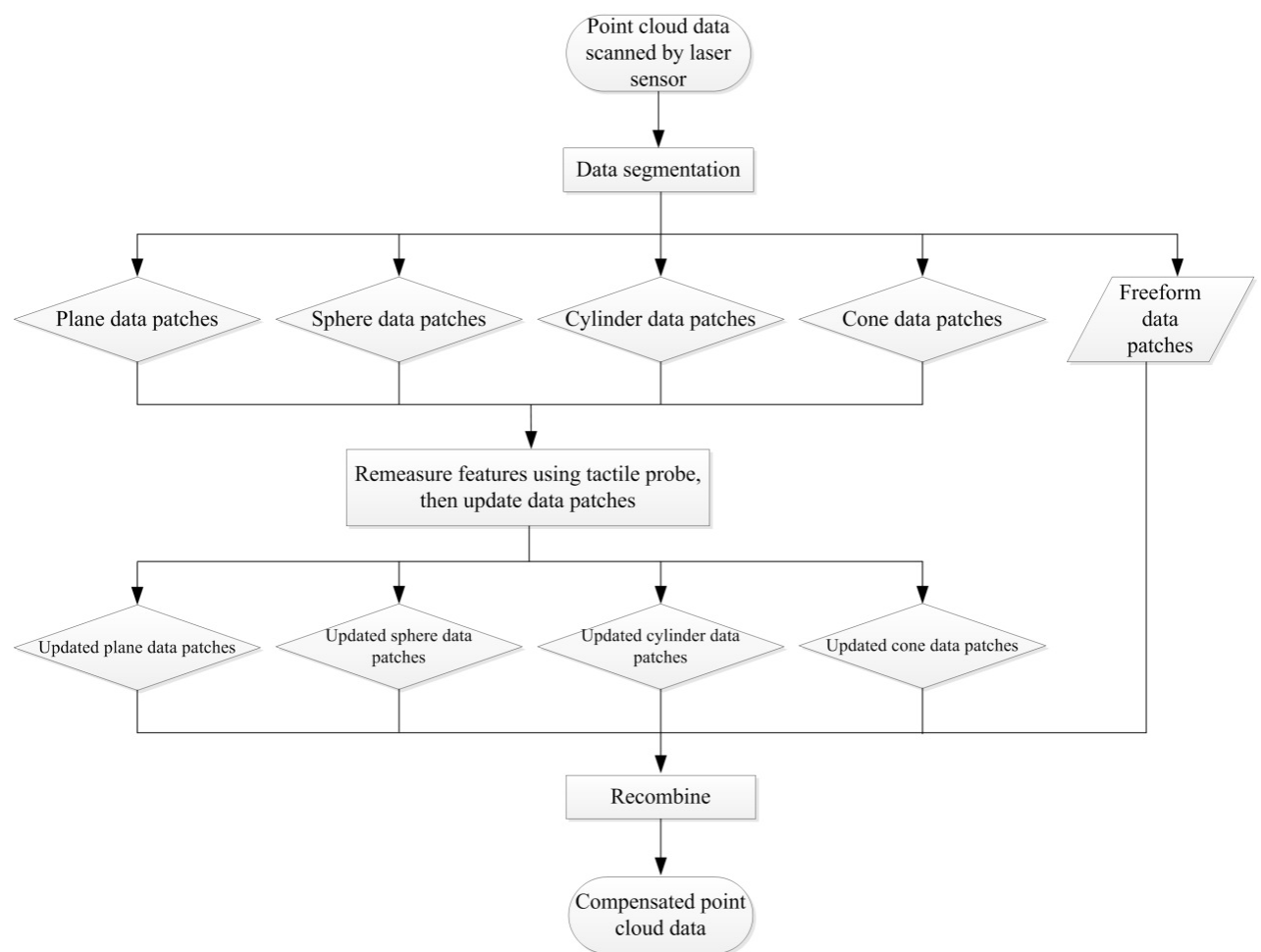Description schematic of the proposed method is shown in Figure 4-6.

Figure 4-6: Schematic of the proposed method

Then the new flowchart of an RE of workpiece by using multiple-sensor contact-optical measuring system can be expressed as in Figure 4-7.
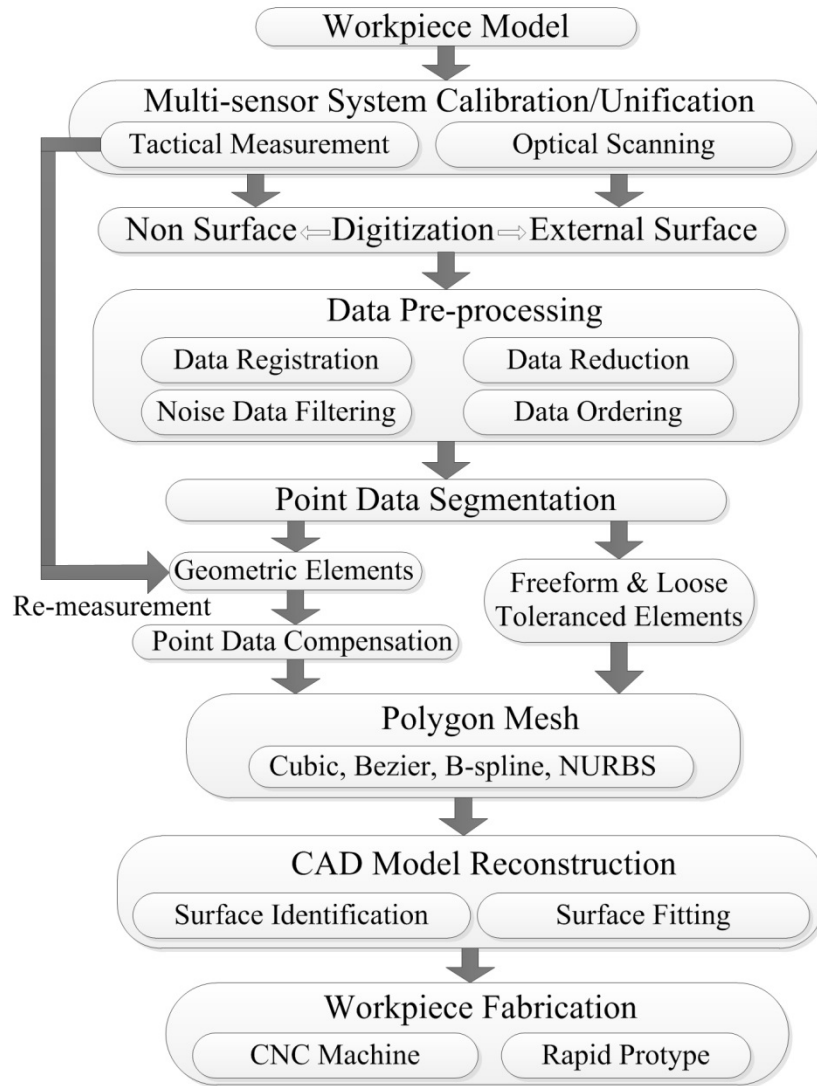
Figure 4-7: New flowchart of RE by using hybrid contact-optical measuring system

4.3.3.2. Algorithms description

The detailed algorithms for compensation of different geometric features based on multi-sensor technique are presented as follows:

(1). Plane compensation

According to Equation (4-17), the parameters to be solved are a, b, c and x_o, y_o, z_o. Here we define $d = -(ax_o + by_o + cz_o)$.

According to our proposed method, the new z coordinate can be derived by:

$$z_{Ni} = (-ax_i - by_i - d) / c \qquad (4\text{-}44)$$

To compare the normal of the plane, we let $d = 1$.

The workflow for plane compensation can be described in Figure 4-8.

Plane measurement using tactile method

⇩

Solve parameters a, b c and d using best fit method

⇩

Plane patch after segmentation using optical measurement
(x,y,z) is one point in the data patch

⇩

$z_N = (-ax - by - d) / c$

⇩

Update all points in the patch and use (x,y,z$_N$) to
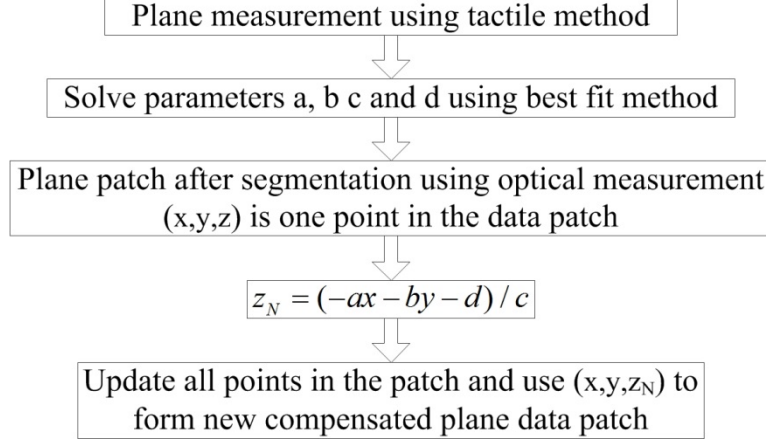form new compensated plane data patch

Figure 4-8: Flowchart of plane compensation by using multi-sensor measuring system

(2). Sphere compensation

According to Equation (4-20), the parameters to be solved are x_o, y_o, z_o and r. First we translate a copy of the data so that the centre of the sphere is at the origin.

$$(x_i, y_i, x_i) = (x_i, y_i, x_i) - (x_o, z_o, y_o) \qquad (4\text{-}45)$$

Then the value of the new z coordinate can be derived by

$$z_{Ni} = \pm\sqrt{r^2 - x_i^2 - y_i^2} \qquad (4\text{-}46)$$

Here two values of z_N are obtained that will fit the sphere. To determine which one is needed, the value of $z(i)$ is determined to be positive or negative:

$$if \ z(i) > 0$$
$$z_N(i) = |z_N(i)|;$$
$$else$$
$$z_N(i) = -|z_N(i)|;$$
$$end$$

In some cases the solving results of z_N includes imaginary parts, which means that the original points are beyond the scope of the sphere to be fitted. We have to delete those points in the new point data coordinates. In fact, this is an effective way to exclude noisy data.

Finally, the origin is translated by an amount equal and opposite to the vector in Equation (4-45), above.

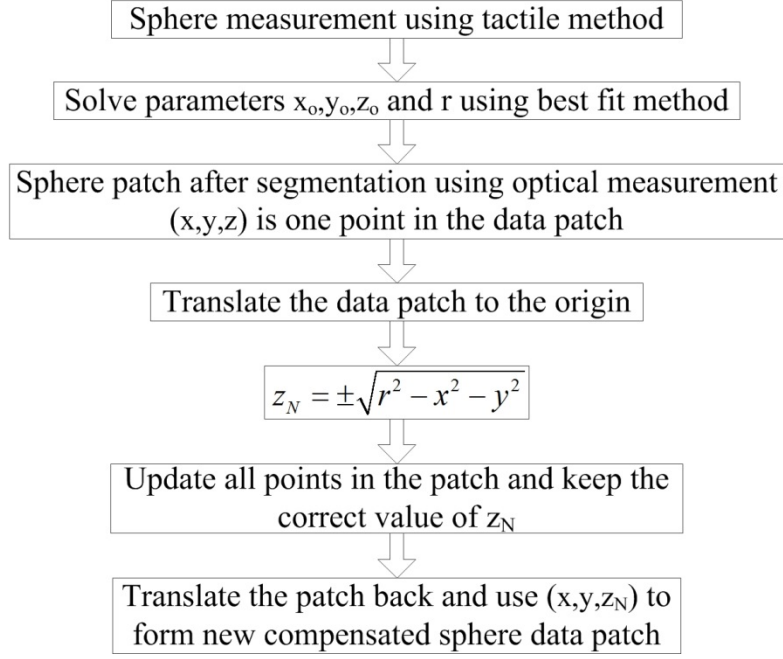The workflow for sphere compensation can be described in Figure 4-9.

Figure 4-9: Flowchart of sphere compensation by using multi-sensor measuring system

(3). Cylinder compensation

For cylinder and cone compensation, the proposed method is inverse shifting of the data so that the point (x_o, y_o, z_o) on the axis lies at the origin. Inverse rotation of the data set is then performed using the transpose of rotation matrix U which rotates (a, b, c) to coincide with $Z - axis$. Again, we will translate and transform the data back after compensation. Then the value of the new y_N coordinate can be obtained by

$$y_{Ni} = \pm\sqrt{r^2 - x_i^2} \tag{4-47}$$

The method for determining the positive and negative of y_{Ni} is much the same as that for spheres.

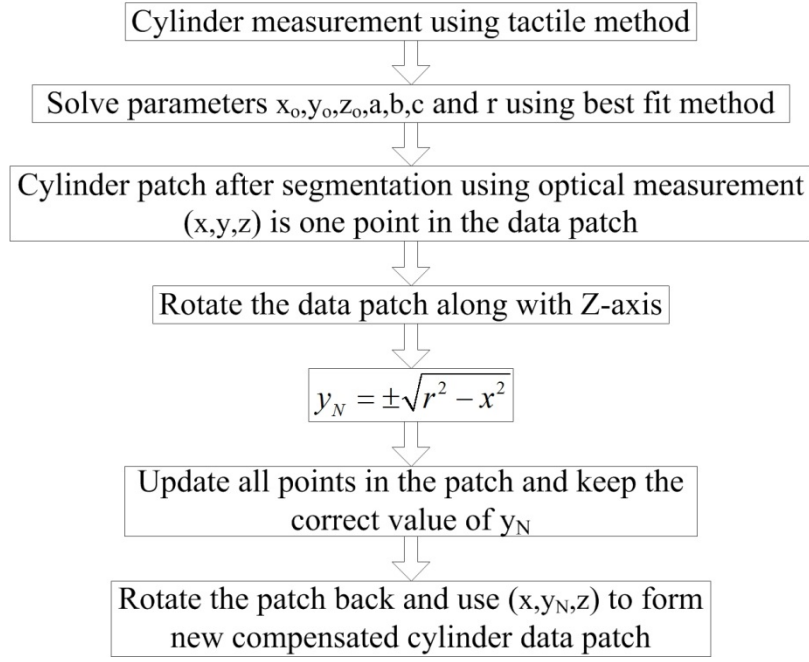The workflow for cylinder compensation can be described in Figure 4-10.

Cylinder measurement using tactile method

⬇

Solve parameters x_o, y_o, z_o, a, b, c and r using best fit method

⬇

Cylinder patch after segmentation using optical measurement (x,y,z) is one point in the data patch

⬇

Rotate the data patch along with Z-axis

⬇

$$y_N = \pm\sqrt{r^2 - x^2}$$

⬇

Update all points in the patch and keep the correct value of y_N

⬇

Rotate the patch back and use (x, y_N, z) to form new compensated cylinder data patch

Figure 4-10: Flowchart of cylinder compensation by using multi-sensor measuring system

(4). Cone compensation

After data set translation and rotation, the value of the new y_{Ni} coordinate of cone can be calculated by

$$y_{Ni} = \pm\sqrt{(r - kz_i)^2 - x_i^2} \tag{4-48}$$

where $k = \tan(\phi)$.

The workflow for cone compensation can be described in Figure 4-11.

4.4. Summary

In many industry areas, it is desirable to create geometric models of existing objects for which no such model is available. RE of workpiece prototype for CAD/CAM is a rapidly discipline where interest is currently high. After elaborating the purpose of RE and the main application areas, the most important data processing steps are outlined and various reconstruction strategies are presented. Specific issues addressed include data pre-processing of points and multiple view registration, polyhedral surface generation and segmentation, related surface representations and creating consistent and accurate B-rep models. The classical workflow of RE is also introduced and finally reconstruction of a geometric model of the prototype is described.

Cone measurement using tactile method

$\Downarrow$

Solve parameters x_o, y_o, z_o, a, b, c and $\emptyset$ using best fit method

$\Downarrow$

Cone patch after segmentation using optical measurement (x, y, z) is one point in the data patch

$\Downarrow$

Rotate the data patch along with Z-axis

$\Downarrow$

$$y_N = \pm\sqrt{(r - kz)^2 - x^2}$$

$\Downarrow$

Update all points in the patch and keep the correct value of y_N

$\Downarrow$

Rotate the patch back and use (x, y_N, z) to form new compensated cone data patch
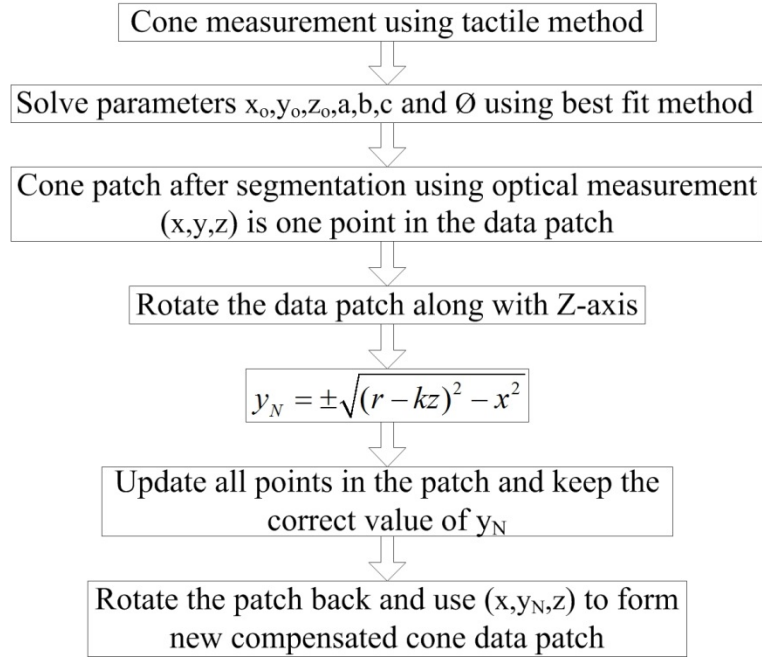
Figure 4-11: Flowchart of cone compensation by using multi-sensor measuring system

The algorithms for computing least-squares best fit geometric elements and initial estimation for the Gauss-Newton algorithm are detailed in this chapter. These algorithms are exploited for best fitting and the compensation of multiple-data measured from multi-sensor system. With the point cloud data acquired using a laser scanner, intelligent feature recognition and segmentation algorithms can be applied to extract the global surface information of the object. Then the high precision touch probe is used to re-measure the geometric features with a small number of sampling points. The obtained information can be subsequently used to compensate the point data patches which are measured by the optical system.

Finally, a novel method for the compensation of fused data measured from integrated multi-sensor system based on geometric algebra approach is proposed. A new workflow for RE of workpiece by using a multi-sensor contact-optical measuring system is also presented.

Validation of the proposed method is described in Chapter 5.

Chapter 5

Experimental Implementation

5.1. Multi-sensor system configuration

5.1.1. System overview

The multi-sensor measurement system used for data acquisition is a Nikon LK V 15.10.8 HA high accuracy ceramic bridge CMM which integrates two different sensors: a Renishaw SP25M touch trigger probe and a Nikon LC15Dx single stripe laser scanner. It operates in a temperature-controlled room, typical of normal CMM applications, with the environmental temperature controlled at 20 ± 0.2 °C. The measurement system contains two parts: the dimensional measurement equipment which include the CMM and the two sensors; the measurement software packages which is used to support the measurement execution and data acquisition. Figure 5-1 gives a general overview of the measurement system. The two sensors integrate with the CMM via the Renishaw PH10MQ articulating motorised probe head; only one sensor can operate at any given time. The software platform CAMIO7 multi-sensor CMM measurement software is used for measurement planning and data acquisition.
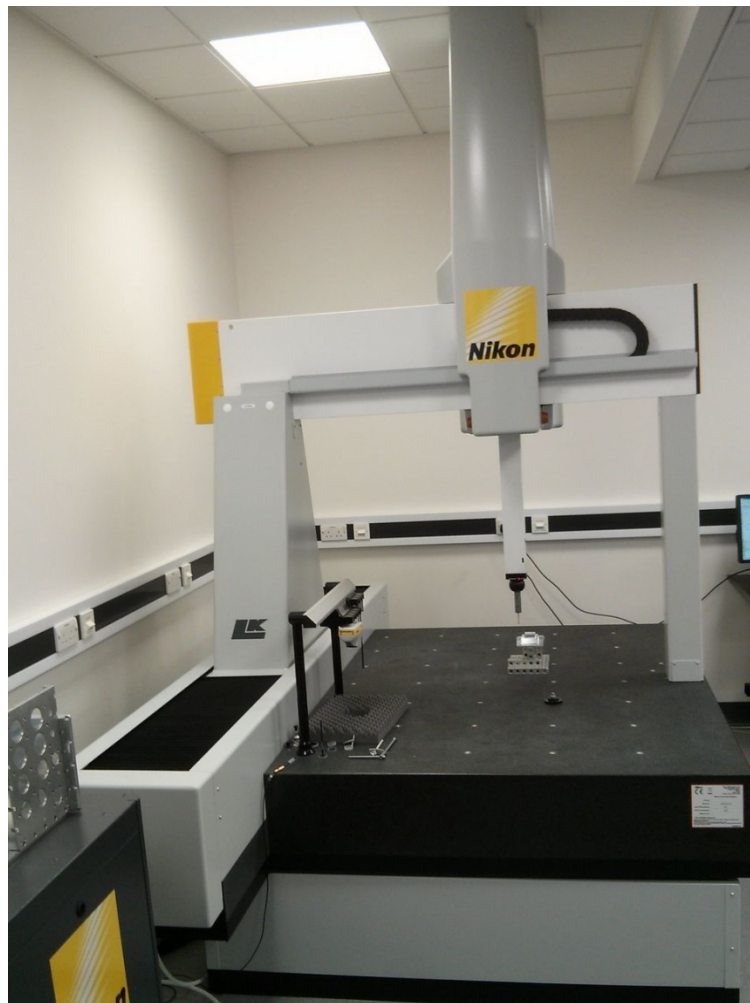

Figure 5-1: Nikon LK V 15.10.8 HA high accuracy ceramic bridge CMM

Table 5-1 shows the main specification parameters of the Nikon LK V 15.10.8 HA CMM, it can be used for touch trigger and non-contact inspection, digitizing, scanning, reverse engineering, etc.

Table 5-1: Nikon LK V 15.10.8 HA high accuracy ceramic bridge CMM

Technical figure	Parameter	Value
	Volumetric accuracy	1.5 um+L/350
	Repeatability	1.5 um
	Velocity	up to 50 m/min
	Acceleration	up to 5400 m/min^2

5.1.2. Sensors description

(1). Renishaw SP25M touch trigger probe

The Renishaw SP25M touch trigger probe comprises two sensors in a single probe system and is able to execute scanning and touch-trigger probing. It is also compatible with different scanning modules, which can carry M3 styli with lengths from 20 mm to 400 mm. Table 5-2 presents the specifications of the SP25M [168].

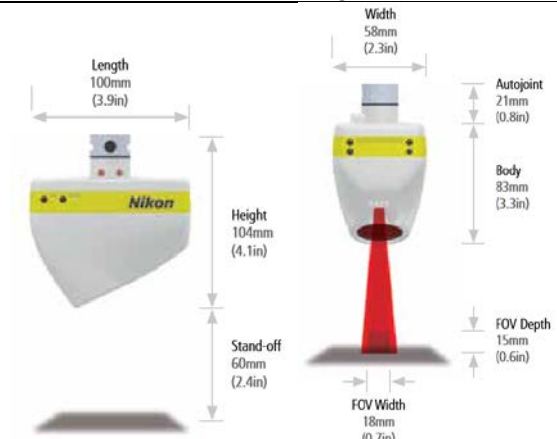Table 5-2: Specifications of the Renishaw SP25M scanning probe system

Technical figure	Parameter	Value
	MPE_E (ISO 10360-2)	1.6+L/375 μm
	Resolution	< 0.1 μm
	Over-travel range	±2.0 mm in X and Y 1.7 mm in +Z 1.2 mm in –Z
	Probe attributes	Pivoting motion in XY plane with translation in Z direction
	Stylus lengths	20-400 mm
	Spring rate	0.2-0.6 N/mm

(2). Nikon LC15Dx laser scanner

Nikon LC15Dx laser scanner works on the laser triangulation principle as described in Chapter 2 and is a high accuracy range laser scanner. The acquired data of LC15Dx are pixel coordinates on 2D images which should be converted to the 3D spatial coordinates of the measured points through calibration. The specifications of the LC15Dx laser scanner are listed in in Table 5-3. The Nikon LC15Dx laser scanner can be used to measure 3D geometric deviations and surface digitization with high point density, etc. When scanning, the surfaces

to be measured should be covered by the field of view (FOV) of the laser scanner. It is also able to digitise shiny surfaces by changing the intensity of the laser. However this is at the cost of sacrificing accuracy.

Table 5-3: Specifications of the Nikon LC15Dx laser scanner

Technical figure	Parameter	Value
	MPE_E (ISO 10360-2)	3.6+L/375 μm
	Multi-stylus test (MPE_{AL})	6 μm
	Resolution (point spacing)	22 μm
	Data acquisition (approx.)	70,000 points/sec
	Points per line (approx.)	900
	Measuring temperature range	18-22 °C (64.4-71.6 °F)
	FOV	18×15 mm
	Laser type	Class 2 (660 nm)
	Weight	370 g

(3). Comparison between two sensors

The two sensors can cover the measurement tasks in macro domains with 2D and 3D data acquisition with tactile or non-contact sensing techniques. Each of them has its own significantly distinct advantages and disadvantages. A complex workpiece is usually comprised of various detailed features, the most suitable sensors must be selected for measurement of each particular feature. The table 5-4 presents the main characteristics comparison of the two sensors. The measuring system integrated with the two sensors can be exploited to capture the surface data in RE and dimensional metrology.

Table 5-4: Comparison of the tactile probe and the laser sensor

	Renishaw SP25M probe	Nikon LC15Dx laser scanner
Principle	Kinematic touch trigger	Laser triangulation
Resolution	< 0.1 μm	22 μm
Speed	1~2 point/second	70,000 point/second
Init. Data type	3D (X, Y, Z)	2D (R, C)
Advantages	1. High resolution/accuracy 2. Not sensitive to the surface reflection 3. Robust and more adaptable to the ambient light	1. High scanning speed and dense point data acquisition 2. Global information acquisition 3. Suitable for the measurements of surfaces with soft/flexible materials
Disadvantages	1. Low data capturing speed 2. Limitations to its own dimension sizes 3. Sparse density of the acquired points data	1. Low resolution, noisy/redundant data 2. Limitations of occlusion and viewpoint 3. Sensitive to the surface optical conditions
Applications	1. Primitive shapes 2. Features with known CAD models 3. Surfaces without large variations	1. Global data acquisition 2. Complex surfaces or topography measure 3. Surfaces with soft/flexible materials

5.2. Case study one: simple geometric shapes

Measurement errors of laser line scanning, their components and sources have been investigated by several authors. Major contributions to the level of noise data are surface optical properties, in-plane and out-of-plane angles and scanning depth [4, 15, 18, 169].

This section first investigates details of measurement results in usage of lase line scanning in dimensional measurement applications. Then the feasibility and robustness of the proposed approach are examined.

The inspection values based on measured and processed results from the Nikon LC15Dx laser scanner are compared to reference values obtained by the SP25M tactile probing. Three different laser scanner measurement errors (position errors, orientation errors and size errors) were investigated by measuring one sphere and one cylinder and comparing the fitting results.

A sphere (Part A) with nominal radius of 12.7 mm and a cylinder (Part B) with nominal radius of 14.55 mm were used to investigate the measurement errors and test the robustness and feasibility of the introduced method. The sphere is made of solid polypropylene with a matt finish and has good roundness and sphericity. The cylinder is made of aluminium alloy and has a shiny surface. Both parts were scanned by the LC15Dx laser scanner and SP25M touch probe five times, separately. During laser scanning, the distance between the surface of the artefact and the laser scanner in various orientations was kept constant by using the

optimal distance to minimize influence of the scan depth to measurement error. Then the original point data scanned by the laser sensor was compensated by using data measured by the tactile probe. The first set of data measured by the tactile probe was used to compensate the data scanned by laser sensor separately.

Figure 5-2 shows the coordinates of the sphere centre and radii calculated from the laser, tactile probe and compensated data; $X-axis$ is the scan sequence (five times for each method).

(a) X coordinates

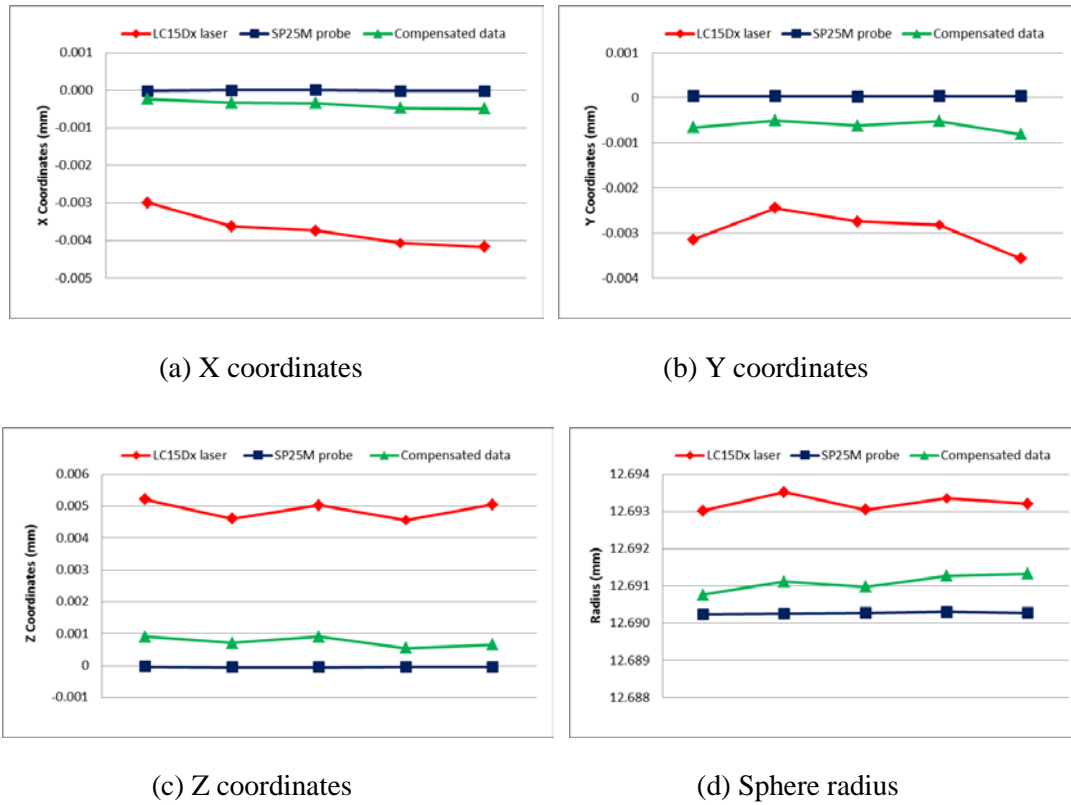(b) Y coordinates
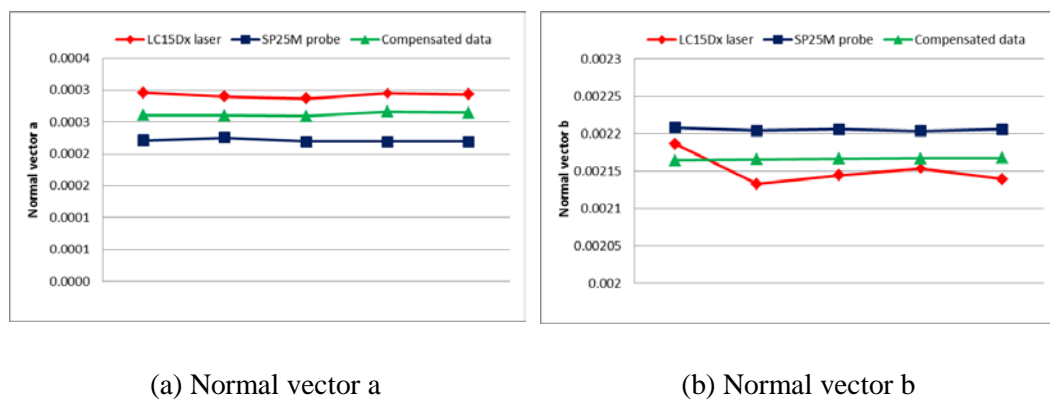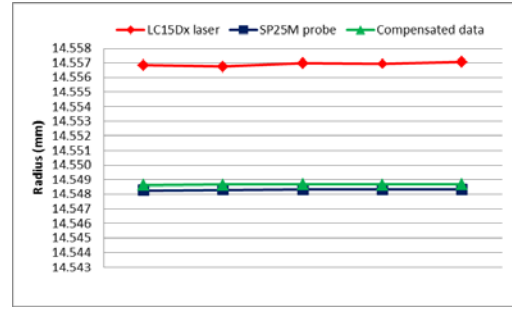
(c) Z coordinates

(d) Sphere radius

Figure 5-2: Fitting results of sphere using different methods

Figure 5-3 shows the normal vector of axis of cylinder and radii calculated from the laser, tactile probe and compensated data.

(a) Normal vector a

(b) Normal vector b
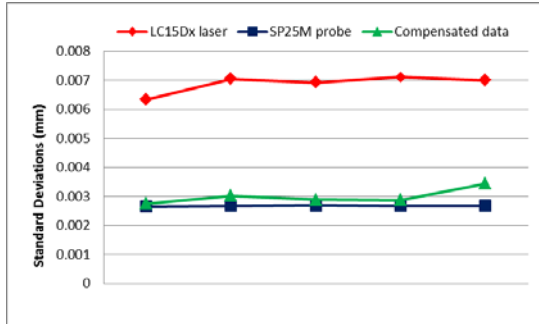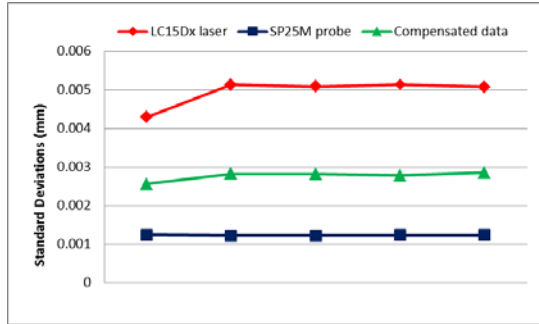
(c) Normal vector c   (d) Cylinder radius

Figure 5-3: Fitting results of cylinder using different methods

Standard deviations of fitting results of Part A and Part B are displayed in Figure 5-4. It can be seen that the deviations measured from SP25M probe are significantly less than those measured from LC15Dx laser scanner.

(a) Sphere (Part A)   (b) Cylinder (Part B)

Figure 5-4: Standard deviations of fitting results of different methods

Overall, the fitting results show high stability of the data measured from the tactile probe. By comparing the centres measured from both sensors, which is presented in Figure 5-2, we can see that there are position errors between two sensors; Figure 5-3 shows the orientation errors between the two sensors by comparing the normal vector of axis of cylinder; Figure 5-2 and 5-3 present the size errors of sphere and cylinder measured from multiple sensors, the shape sizes scanned from laser sensor are slightly bigger that those measured from tactile probe.

Through the above data analysis, it can be seen that all three errors, which are position error, orientation error and size error, are observed in the laser line scanning by using tactile probing as a reference. The systematic errors between laser sensor and tactile sensor and standard deviations significant decrease after the laser data set is compensated.

5.3. Case study two: plane-sphere-cylinder-cone

Part C (Figure 5-3 (a)) is made of aluminium alloy 5083 and designed with only geometric features. After data segmentation, these geometric elements are exploited to prove the concept proposed in this thesis. The elements on the parts include the most typical of geometric features: plane, sphere, cylinder and cone. The workpiece was located on the bed of the CMM and fixed by clamps when performing the measurement.

The laser sensor was used for surface global information acquisition. Because of the reflection of the surface, the intensity of the laser was changed to scan the shiny part. The views of the laser scanner were adjusted by the Renishaw PH10MQ probe head to cover the full surface. A trial version of the commercial software, Geomagic Wrap 2013, was used for performing the data pre-process tasks of data denoising and reduction, etc. The data scanned by laser and tactile probe are shown in Figure 5-5 (b) and (c), respectively. Figure 5-5 (d) displays merged and organized point cloud data.
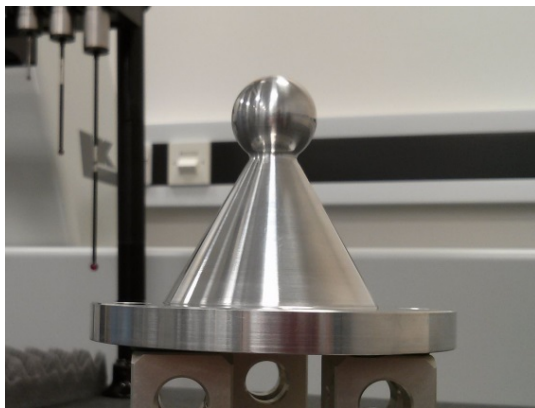
(a) Part C to be measured
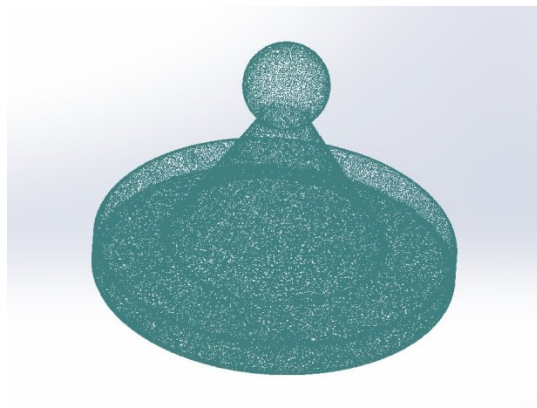
(b) Data measured from laser scanner
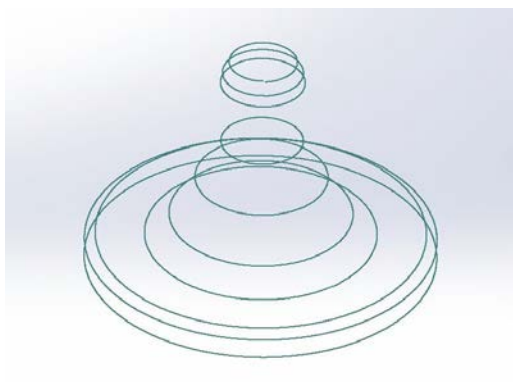
(c) Points measured from tactile probe

(d) Merged data

Figure 5-5: Points data measured using multi-sensor system

The data measured by the laser scanner was segmented by Woo's method which has been described in Section 4.3.2 (see Figure 5-6). Then the large amounts of unordered points that belong to different geometric element patches can be compensated by a small amount of point data using the tactile probe.
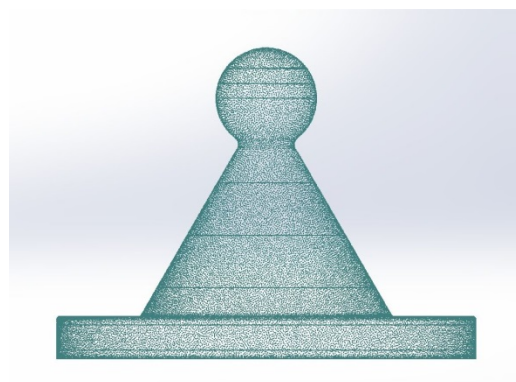

(a) Plane

(b) Sphere

(c) Cylinder

(d) Cone
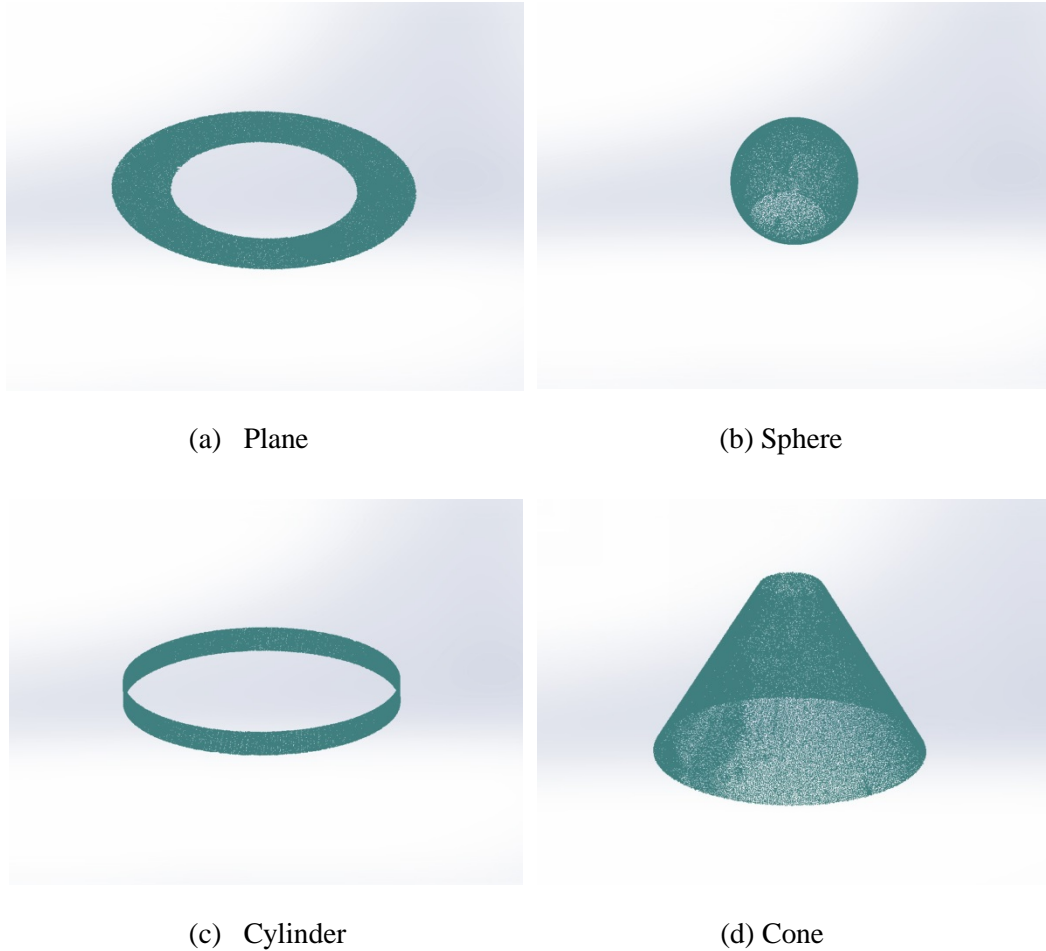
Figure 5-6: Point cloud data segmentation

There is a desire to determine how many points must be captured by the tactile probe to achieve the desired representation of geometric elements. Traditionally, the number of sampled points is required to be ten times the number of parameters in the model [170]. However, in this experiment more sampled points were taken and the fitting results were compared.

The fitting results for different features using different methods and their standard deviations are listed in Table 5-5. All the parameters in the table have been introduced in Section 4.3.2. All the algorithms are introduced in Section 4.3.3 and the experimental results are calculated by utilizing own developed Matlab program.

Table 5-5: Fitting results using different methods (Dimensions in mm)

| Feature	Parameter	Laser	Tactile robe (MIN points)	Tactile probe (more points)	Compensated
Plane	Points	59,064	60	1,031	59,064
	a	-0.0001	0.0000	0.0000	0.0000
	b	0.0000	0.0000	0.0000	0.0000
	c	1.0000	1.0000	1.0000	1.0000
	d	1	1	1	1
	Std Dev	1.278×10^{-2}	7.4×10^{-4}	6.8×10^{-4}	0
Sphere	Points	45,071	40	930	45,071
	x_o	0.0061	0.0022	0.0025	0.0027
	y_o	0.0090	-0.0032	-0.0031	-0.0031
	z_o	51.9679	51.9717	51.9719	51.9716
	r	12.0080	12.0006	12.0006	12.0009
	Std Dev	9.62×10^{-3}	7.1×10^{-4}	6.7×10^{-4}	2.67×10^{-3}
Cylinder	Points	69,426	70	1,270	69,426
	a	-0.0001	0.0000	0.0000	0.0000
	b	0.0001	0.0001	0.0001	0.0001
	c	1.0000	1.0000	1.0000	1.0000
	r	50.0175	50.0106	50.0107	50.0108
	Std Dev	1.448×10^{-2}	8.4×10^{-4}	8.1×10^{-4}	1.37×10^{-3}
Cone	Points	69,030	70	1,503	69,030
	a	-0.0001	-0.0002	-0.0003	-0.0001
	b	0.0001	0.0005	0.0006	0.0006
	c	1.0000	1.0000	1.0000	1.0000
	ϕ	29.9982	29.9976	29.9975	29.9979
	Std Dev	1.522×10^{-2}	9.2×10^{-4}	1.25×10^{-3}	1.89×10^{-3}

All the computing tasks were operated on a desktop computer with an AMD Phenom II×4 970 3.5 GHz processor and 8GB RAM. Table 5-6 presents the computing time of data updating for different features.

Table 5-6: Computational time

Feature	Plane	Sphere	Cylinder	Cone
Number of points	59,064	45,071	69,426	69,030
Computational time (s)	0.004354	0.023247	0.063289	0.144763

The meshed surfaces before and after compensation are illustrated in Figure 5-7 (a) and (b), respectively.
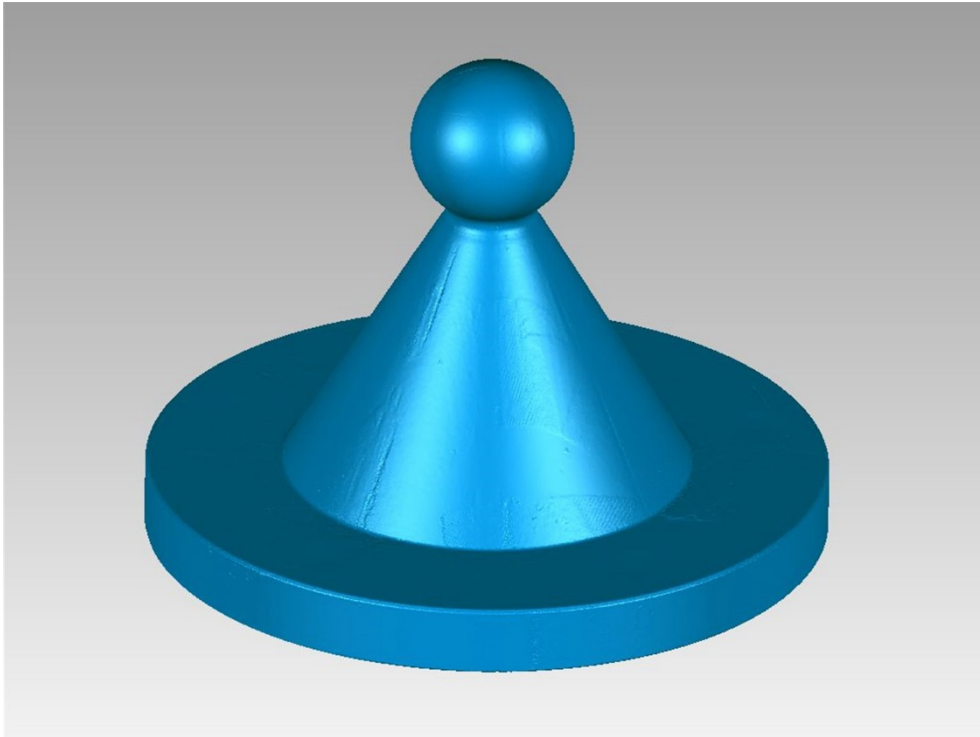
(a) Mesh surface before compensation
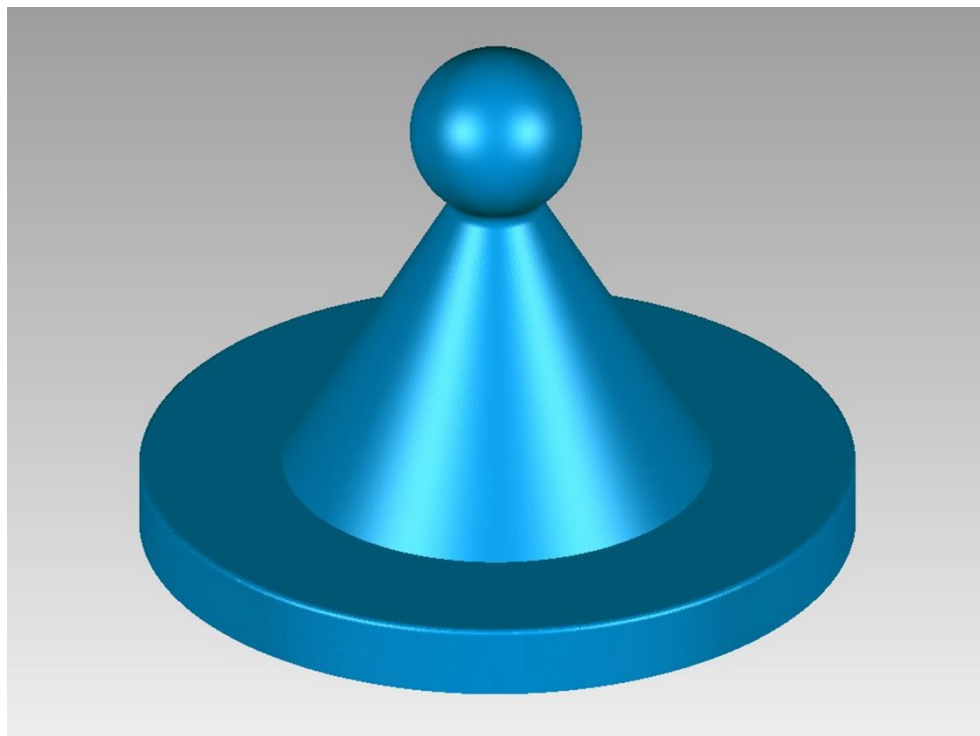
(b) Mesh surface after compensation

Figure 5-7: Mesh surface

From the above fitting results we can draw several conclusions:

1) It has been shown that ten times the number of parameters is a sufficient number of measurement points using the tactile probe, considering its measurement uncertainty. This result is consistent with the conclusion introduced in literature [170].

2) After compensation, the quality of the point data measured from the optical sensor has been greatly improved (see Figure 5-7). In theory, the compensated data has the same accuracy as the data measured from the tactile probe.

3) The compensated data is more robust and more likely to be identified by recognition algorithms, and is therefore more conducive to process in the next step of model reconstruction.

5.4. Case study three: complex housing

5.4.1. Multi-data acquisition

Part D is a more complex housing (Fig. 8 (a)) modified from literature [95],which has a shiny metal surface. It also contains the typical geometric features and freeform characteristic. Therefore, it should be an interesting case to test and verify the proposed approaches for multi-sensor data fusion for RE. The workpiece was located on the bed of the CMM and fixed by clamps, which are supplied by the manufacturer when performing the measurement.
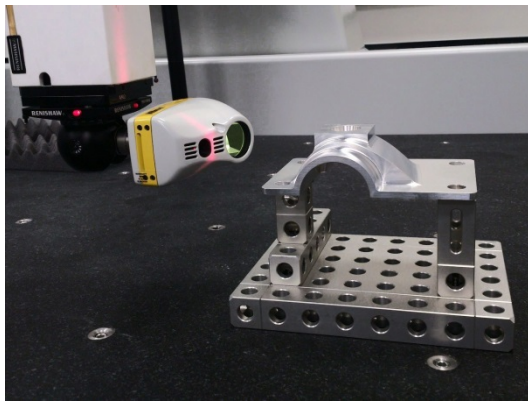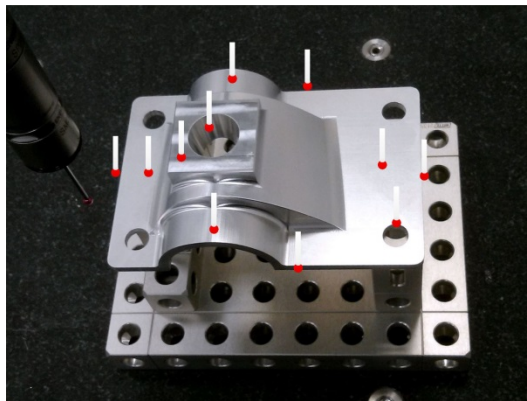
(a) Laser scanning   (b) Tactile probing

Figure 5-8: Tested workpiece and sensor selection

The laser sensor was used for surface global information acquisition (Figure 5-8 (a)). Because of the reflection of the surface, the intensity of laser was changed to scan the shiny workpiece. Two poses of the part were required in order to acquire entirely the point cloud data from the top and the bottom of the workpiece. The datum plane and tight tolerance features need to be measured more accurately, and the inner holes are difficult to scan by laser scanner because of occlusion. Therefore an SH25-1 stylus holder with a M3 40 mm stylus carried by the

SP25M tactile probe was exploited to measure these features (see Figure 5-8 (b)). All point cloud data was scanned manually by the operator.

Table 5-7 presents the numbers of points of raw data, scanning views and measurement time.
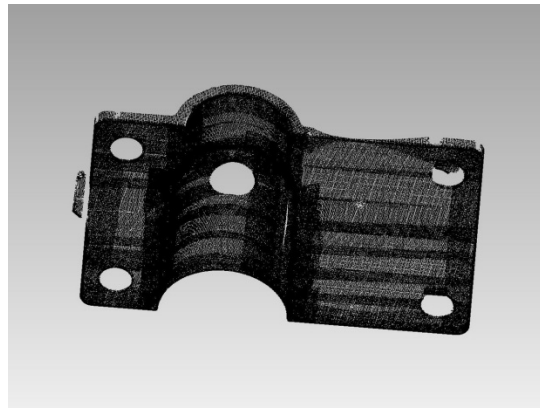
Table 5-7: Numbers of points and scanning time

Methods	Views	Number of points	Measuring time (min:s)
Laser - top	21	6,573,959	12:04
Laser - bottom	12	3,840,678	7:15
Tactile probe	-	4,143	14:55

The raw data for the tip & bottom surfaces scanned by the laser are shown in Figure 5-9 (a) and (b), respectively. The points scanned by touch probe are shown in in Figure 5-9 (c). First, the top and bottom surface point data were registered to the same coordinate system, the method proposed in reference [171] was exploited to align the two piece of data. The raw points cloud data acquired by the laser scanner contains a large number of noise and redundant data. The initial acquired point data is imperfect, which increases the difficulty of the geometry processing in the next stages. Therefore, data denoising and filtering processes are necessary to improve the quality of initial point cloud data. As the data pre-processing procedures are beyond the study scope of this thesis, here the existing Geomagic Wrap software was used to do the pre-processing and improve the quality of the raw data. Figure 5-9 (d) shows the processed and aligned point cloud data.
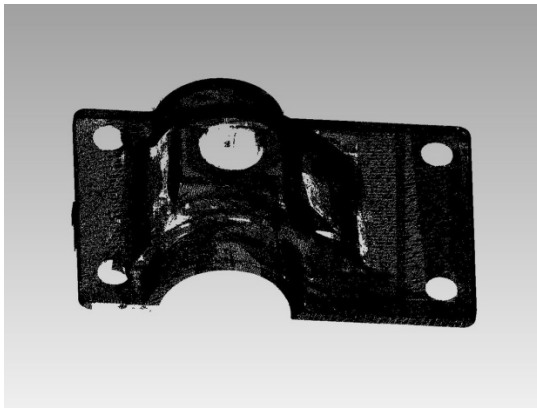
(a) Top surface scanned by laser　　　　(b) Bottom surface scanned by laser
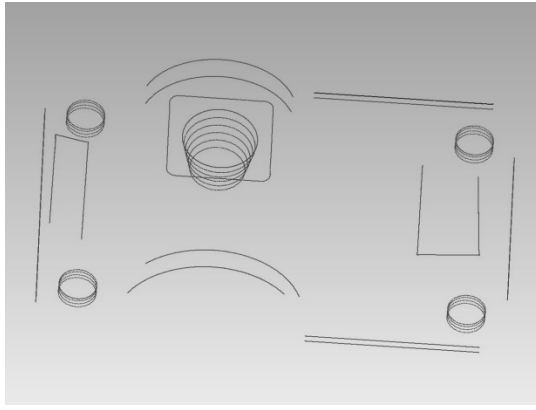
(c) Data scanned by touch probe   (d) Points data after pre-processing and register
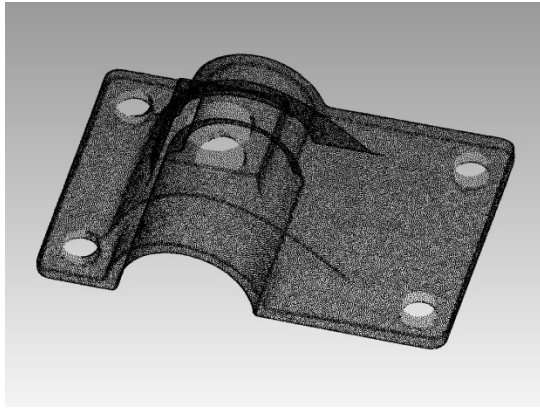
Figure 5-9: Examples of the acquired data

5.4.2. Discrete geometry processing and CAD model reconstruction

5.4.2.1. Point data segmentation and compensation

The merged and organized point cloud data measured from both sensors (Figure 5-10 (a)) was segmented by a feature recognition algorithm. Figure 5-10 (b) shows the point cloud data after segmentation. Then the vast amounts of unordered points belonging to different geometric element patches can be compensated using a small amount of point data from the touch probe. This process is realized by utilizing own developed Matlab program.
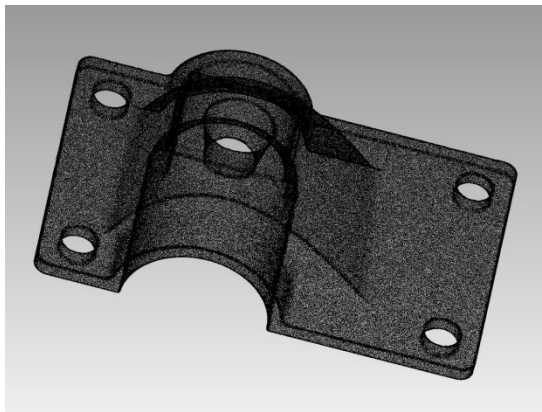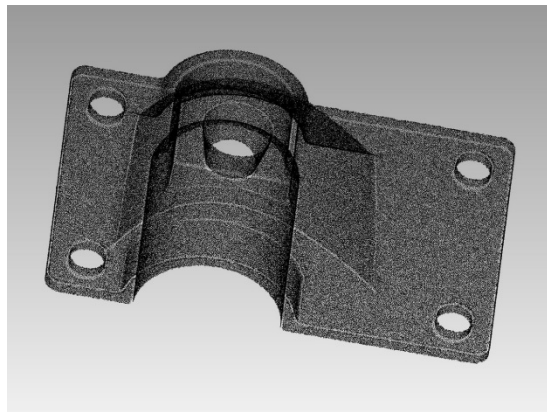
(a) Merged points   (b) Points data segmentation

Figure 5-10: Points cloud data after segmentation

5.4.2.2. Triangle mesh generation and shape recognition

The compensated point data is used to generate a polyhedral surface which is shown as Figure 5-11 (a). Figure 5-11 (b) illustrates the shape recognition on the mesh surface.
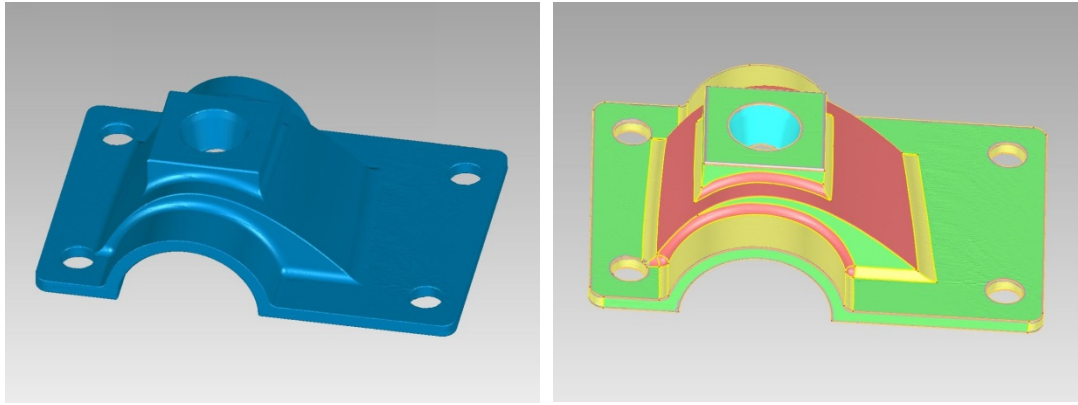
(a) Triangle mesh surface   (b) Shape recognition

Figure 5-11: Points cloud data after segmentation

5.4.2.3. Model Reconstruction

After trimming and stitching the parametric surface (Figure 5-12 (a)) a solid CAD model is generated. Figure 5-12 (b) shows the reconstructed CAD model in the SolidWorks 2013 environment (both uncompensated and compensated models are visually the same).
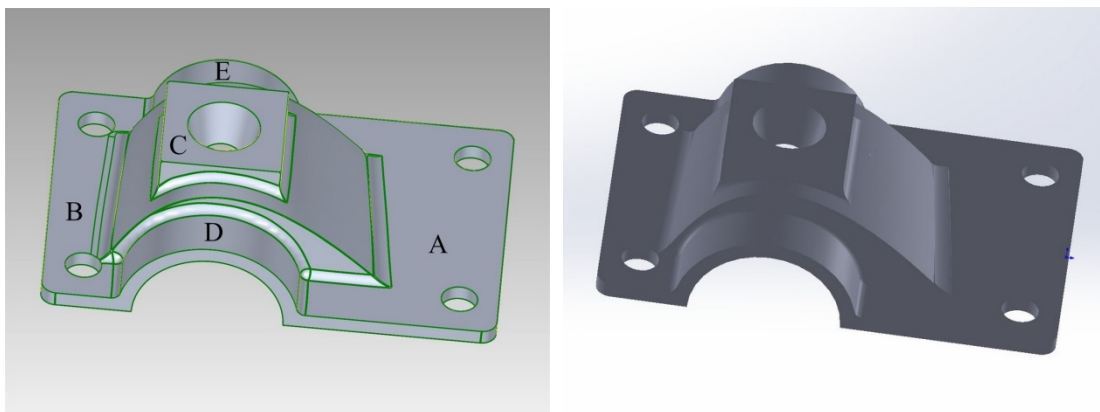
(a) Parametric surface   (b) CAD model rebuild

Figure 5-12: CAD model reconstruction

5.4.3. Measurement speed and accuracy comparison

5.4.3.1. Measurement speed comparison for sensors

In the digitizing process for Part D, the actual scanning time was 19 min 19 s and the tactile probing time was 14 min 55 s, therefore the total measuring time was 34 min 14 s (Table 5-7).

Finally 105,122 points scanned by laser sensor were retained after data reduction to generate a satisfactory mesh surface for CAD model reconstruction, and 2,019 points measured from tactile probe were exploited to compensate the laser scanned data.

In comparison, if we assume that the tactile probe senses the part at the speed of 4-5 points per second, based on the scanning speed presented in Table 5-7, the time to digitise the part using only a tactile method would be a minimum of six hours. The integration of the laser scanner and CMM therefore leads to much faster measurement than the tactile method alone.

5.4.3.2. CAD model accuracy comparison

An independent high accuracy Zeiss PRISMO system, which has been introduced in Section 3.4.1, was exploited to provide an independent evaluation of the accuracy of the reconstructed CAD model. The method described in Chapter 3 was used to unify the two coordinate systems. Table 5-8 shows the residuals of the coordinates and RMSR after transformation from Nikon LC15Dx laser scanning coordinate system to the Zeiss CMM coordinate system.

Table 5-8: The residuals & RMSR of coordinates (Zeiss & Nikon LC15Dx)

Unit: mm	Datum point	Traditional Method			Datum point	Centroid Method		
		X	Y	Z		X	Y	Z
Residuals	A_1	0.001	-0.005	0.006	A_O	0.001	-0.004	0.003
	A_2	-0.006	0.004	0.003	B_O	-0.004	0.001	0.003
	A_3	0.008	0.007	0.008	C_O	0.000	0.000	0.000
RMSR		5.774×10^{-3}				2.403×10^{-3}		

It can be seen that all the residuals of coordinate transformation by using centroid are superior to the traditional method, which further indicates the effectiveness of the method proposed in Chapter 3.

To validate the final reconstructed CAD model quality, we use the root mean square (RMS) error distance to check the accuracy of the constructed CAD model S_{CAD}. However in practice, the actual surface may be difficult or even impossible to obtain. A large number of accurate CMM probing points can be exploited as the reference points on the actual surface [172]. The RMS can then be obtained by

$$RMS = \sqrt{\frac{\sum_{i=1}^{N}\left[d(p_i^T, p_i^S)\right]^2}{N}} \tag{5-1}$$

where p_i^T is the sampled point using CMM tactile probe, N is the number of those sampled points. p_i^S is the projected point to the constructed surface of CAD model S_{CAD}, and $d(p_i^T, p_i^S)$ is the distance between p_i^T and p_i^S.

From Figure 5-13 & 5-14, it can be seen that see the accuracy of reconstructed CAD model after compensation, especially the geometric elements rebuilt from the fused data, has been greatly improved.

Table 5-9 shows the RMS comparisons of the reconstructed CAD models. We can also see that the result indicates that the accuracy of the geometric elements of reconstructed CAD model has been greatly improved after compensation.

Table 5-9: RMS comparison

RMS (mm)	Before compensation	After compensation
Geometric features only	0.045	0.007
Geometric features & freeform	0.074	0.062

5.4.4. Further improvement of the reconstructed model

The final aim of RE is to create a 'more perfect' model representing true design intent as previously described, which means it does not need to simply copy the original product to be reverse engineered. Of course, this requires a detailed understanding of the function and a priori global characterization of the shape of the part.

For example, by analysing the design intent of the housing workpiece, the plane A and B are supposed to be coplanar, plane A and C should be parallel; and cylinder E and F should be coaxial (see Figure 5-12 (a)). Then these adjustments can be realised in the compensation process. In other words, through changing the parameters which are calculated from data measured by touch probe, the data patches measured from optical sensors can be corrected. In this way a 'more perfect' CAD model can be created.

The methods provided in this thesis simplify the problem, so could eventually facilitate an automatic system capable of detecting these relationships.
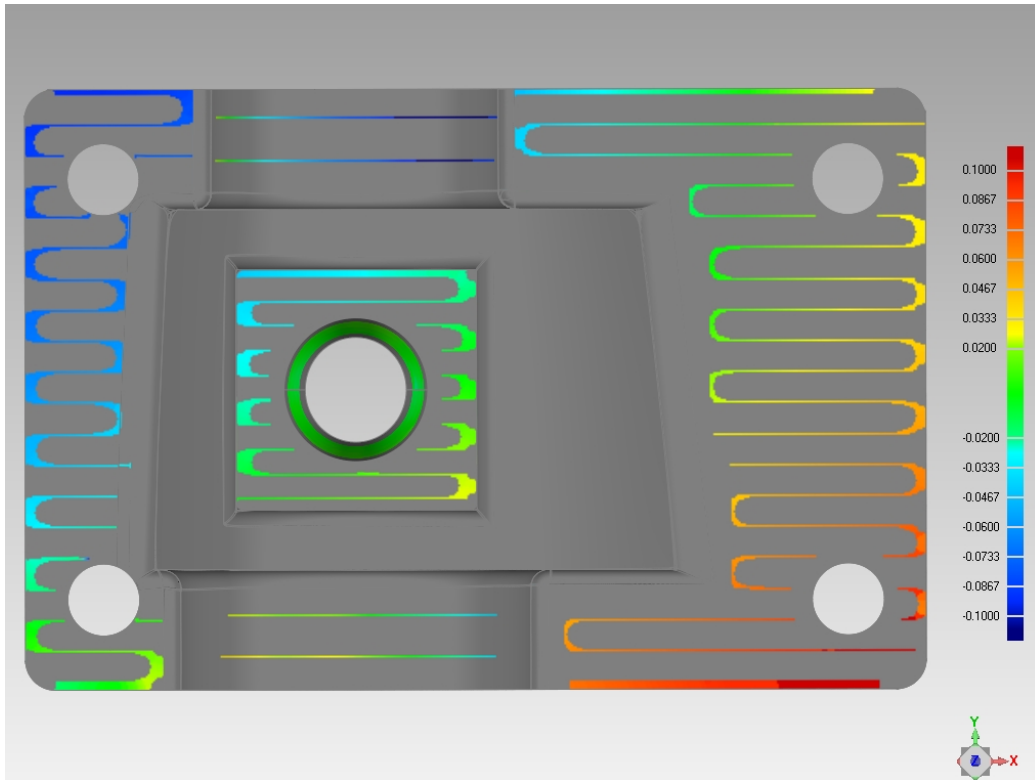
(a) Before compensation
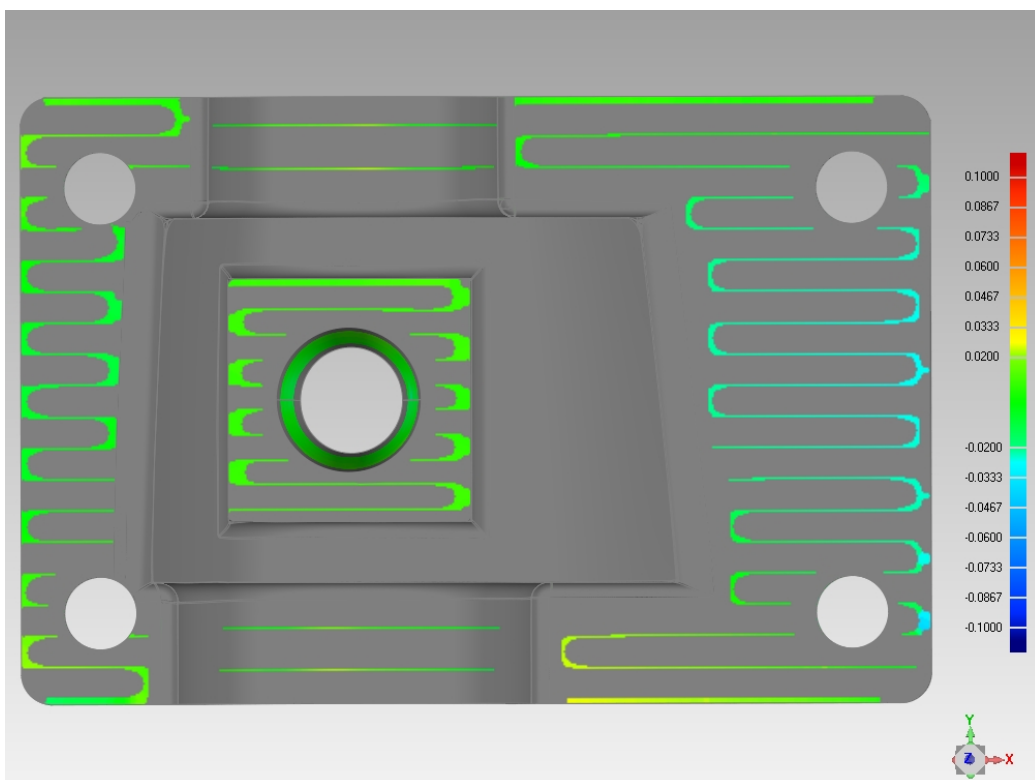
(b) After compensation

Figure 5-13: The comparison of geometric features
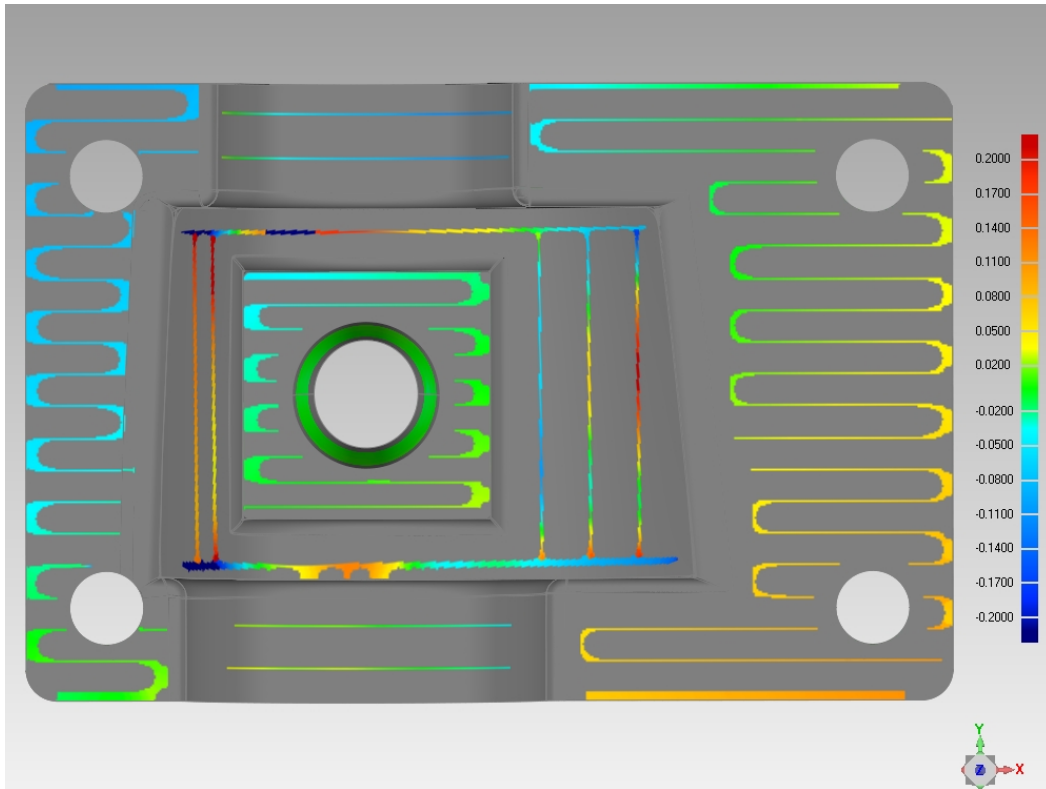
(a) Before compensation
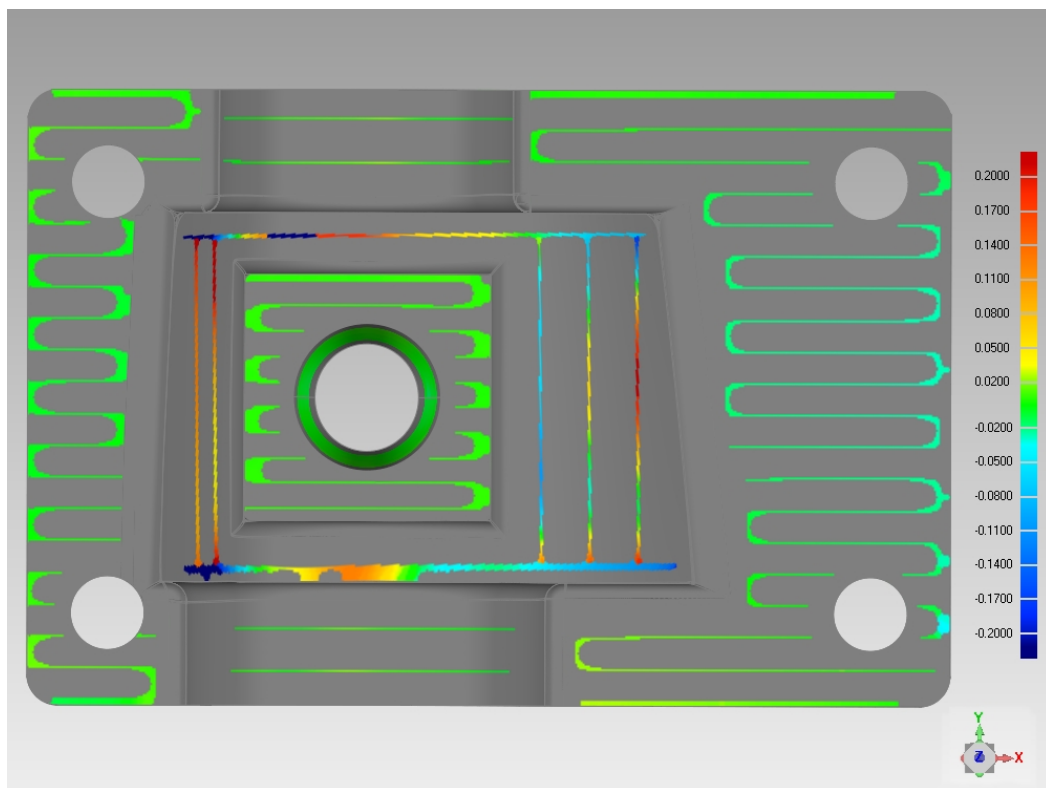
(b) After compensation

Figure 5-14: The comparison of geometric features & freeform

5.5. Summary

This chapter aims to validate the proposed methods in Chapter 4.

Firstly, three different measurement errors - position errors, orientation errors and size errors of the laser line scanner are tested by using a SP25M tactile probe as a reference. Then the feasibility and robustness of the proposed approach are examined.

Secondly, a part with common geometric features is selected to test the introduced method after data segmentation. The workpiece is fully digitized using the multi-sensor system - Nikon LK V 15.10.8 HA high accuracy ceramic bridge CMM. A set of programs, based on Matlab R2011b platform, has been developed for verification of the proposed methods of data fusion based on multiple sensors. The experiment results show that the algorithms provide satisfying performances and the vast amounts of unordered points measured from the optical sensor are converted to ordered and accurate data points after compensation.

Finally a workpiece that contains typical geometric features and freeform characteristics is investigated to further verify the proposed method. The multiple data are acquired by laser scanning and touch probing in both complementary and competitive multi-sensor configurations. First the acquired point data of the workpiece are pre-processed in the commercial software Geomagic Wrap; then the optical scanned data are compensated by using own developed Matlab program; finally the compensated point data are processed in the SolidWorks environment to build the CAD model. The measurement speed using different methods is compared and the accuracy of the reconstructed CAD models is evaluated by an independent high precision CMM. Further improvement of the reconstructed model has also been discussed.

Chapter 6

Conclusions & Future Work

6.1. Summary

In many areas of industry, it is desirable to create geometric models of existing objects for which no such models are available. Reverse engineering (RE) is a rapidly evolving discipline intended to meet these needs. RE typically starts with measuring an existing object so that a surface or a solid model can be deduced in order to exploit the advantages of CAD/CAM technologies. For rebuilding the workpiece, the holistic information of the workpiece as one entity must be known. This includes dimensional and geometrical, macro and micro geometric surface related characteristics with tolerances, and sometimes information regarding the interior structure of the part. At present, no single sensor solution can efficiently provide this information. Multi-sensor data acquisition and fusion is an effective approach to solve this problem.

Multi-sensor data fusion has been shown to be able to realize measurements with holistic, more accurate and reliable information. Applications of multi-sensor integrated systems in 3D measurement are of increasing importance in quality control, RE and many other industrial fields. This thesis investigates a competitive and complementary fusion of integrated tactile-optical coordinate measuring system for RE applications. It is shown to fulfil the increasing requirements for rapid and accurate reconstruction of the CAD model of a workpiece with complex shapes.

A modified calibration method for referencing both tactile and optical sensors in one unified coordinate system is presented. As the contact probe and optical scanner work in their separate coordinate systems, these coordinate systems have to be unified to produce correct result. A sphere-plate artefact with nine spheres is developed for data integration of multi-sensor system and experimental results prove this novel approach is more accurate than the traditional three spheres method. After unification, the combined data from both systems is treated as being from one source. In comparison to using a Iterative Closest Point (ICP) method to register the data captured by multiple sensors, this new approach, presented in Chapter 3 is more robust and convenient.

A new workflow for RE of workpiece based on integrated tactile-optical coordinate measuring system is also developed. The new workflow allows a more reliable source to compensate less accurate information.

A set of algorithms for computing least squares best-fit discrete geometry elements is summarized. Based on the existing methods, the fitting algorithms for the four most common geometric features are detailed and the initial estimates methods for solving nonlinear least-squares problems are presented. In general, laser line scanning and fringe projection are

considered to be less accurate compared with tactile probing. Then the parameterisations of the elements can be obtained through least-squares fitting of a small amount of points probed by a tactile sensor, and then these parameterisations can be used to compensate the vast point cloud data scanned by the optical method. This combination of measuring systems enables the improvement of the measurement performance. A small amount of discrete point data measured by the high accuracy, but relatively slow tactile probe, can be used to compensate the densely scanned data patches that have been measured by the fast, but relatively low accuracy optical method. Unlike most of the other hybrid contact-optical systems based on cooperative configuration, this work focuses on developing a competitive system to ensure the accuracy of measurement results and reduce the measuring time simultaneously.

A new competitive approach for rapid and accurate RE of geometric features from multi-sensor systems based on a geometric algebra approach is proposed. A set of programs based on the Matlab R2011b platform has been developed for the verification of the proposed method. Then the compensated data is processed to rebuild a CAD model in the SolidWorks 2013 environment.

Other existing cooperative multi-sensor configuration approaches only use optical sensors to capture the global surface information of the object and then guide the slower tactile probe to digitize the surface. In the presented method, the multiple data sets are acquired by laser scanning and tactile probing in both competitive and complementary multi-sensor configurations. With the point cloud data acquired using a laser scanner, intelligent feature recognition and segmentation algorithms can be applied to extract and segment the point cloud data. Then the tactile probe is used to re-measure the holes, which are difficult to measure by laser sensor, and tight tolerance geometric features with a small number of sampling points. The obtained information can be subsequently used to compensate the point data patches which are measured by laser sensor, as described in Chapter 4.

The results of the four case-study experiments presented in Chapter 5 show that the algorithms provide satisfactory performance and the vast amounts of unordered points measured from optical sensor are converted to orderly and more accurate point data after compensation. It usually needs several hours to fully digitize a workpiece by using a tactile sensing device. However, in the presented approach the total measurement time is drastically reduced. A case strictly (Part D) would take six hours to digitizing using a tactile probe, but only about 30 minutes using the proposed method, an improvement of 90% which greatly improves measurement efficiency without losing accuracy. In addition, the geometric modelling accuracy in RE applications has been improved from 45 microns to 7 microns.

These results compare well to other competitive methods. In general, the method introduced in this thesis reveals a better accuracy of data fusion than the approach introduced by Huang & Qian [96] and the method presented by Bešić, et al. [97], as described in Section 4.3.1.

6.2. Contributions of this thesis

To conclude, the work undertaken in this thesis has resulted in several contributions to knowledge for multi-sensor integration and data fusion. The following list provides the novel contributions:

1) A modified calibration approach to unify tactile and optical system for form measurement was developed. After system unification, the combined data from both systems is fused into one source. Compared with the classic ICP algorithm for multi-sensor data registration, the new approach is more robust and convenient to register data captured from inhomogeneous sensors with different resolutions (see Chapter 3).

2) A new workflow based on tactile-optical multi-sensor techniques for RE applications has been established. This workflow allows more accurate point data be exploited to compensate less reliable data and take advantage of both separate systems.

3) A set of algorithms for discrete geometric element fitting are summarized, and initial estimates, for best-fitting geometric elements are presented. The estimate for the cone, is highlighted.

4) Based on the above algorithms, a set of programs for geometric elements best-fit and compensation are developed. These programs are based on the Matlab platform and used to test and verify the methods and algorithms presented in this thesis.

5) Finally a competitive configuration of integrated tactile-optical system for fast and accurate RE of complex shape part is proposed. Four workpieces are selected to test and verify the proposed methods.

6.3. Future work

The multi-sensor integration and data fusion for RE of workpiece with complex shapes involve many other interesting topics which haven't been mentioned or addressed in this thesis. Some potential and promising future work is presented below:

1) Automation of RE

The ultimate goal of RE is a fully automatic solution to build a complete and consistent CAD model. There is a long way to go to achieve this objective. However, the reduction of manual intervention is strongly desirable. For example, a cooperative and competitive integration of the proposed multi-sensor measuring system would realize the benefits of

automatic digitization and would be especially valuable for reconstruction of complex surfaces.

2) Freeform surface measurement

In this thesis, the proposed multi-data compensation method has been proven to work for geometric elements. Multi-sensor data fusion for freeform dimensional measurement or RE applications is another promising avenue for research.

References

[1] J. Esteban, A. Starr, R. Willetts, P. Hannah, P. Bryanston-Cross, A review of data fusion models and architectures: towards engineering guidelines, Neural Computing & Applications, 14 (2005) 273-281.

[2] A. Weckenmann, T. Estler, G. Peggs, D. McMurtry, Probing Systems in Dimensional Metrology, CIRP Annals - Manufacturing Technology, 53 (2004) 657-684.

[3] H. Schwenke, U. Neuschaefer-Rube, T. Pfeifer, H. Kunzmann, Optical methods for dimensional metrology in production engineering, CIRP Annals-Manufacturing Technology, 51 (2002) 685-699.

[4] H.-Y. Feng, Y. Liu, F. Xi, Analysis of digitizing errors of a laser scanning system, Precision Engineering, 25 (2001) 185-191.

[5] V.H. Chan, C. Bradley, G.W. Vickers, A multi-sensor approach to automating co-ordinate measuring machine-based reverse engineering, Computers in Industry, 44 (2001) 105-115.

[6] V. Carbone, M. Carocci, E. Savio, G. Sansoni, L. De Chiffre, Combination of a vision system and a coordinate measuring machine for the reverse engineering of freeform surfaces, The International Journal of Advanced Manufacturing Technology, 17 (2001) 263-271.

[7] T.-S. Shen, J. Huang, C.-H. Menq, Multiple-sensor integration for rapid and high-precision coordinate metrology, IEEE/ASME Transactions on mechatronics, 5 (2000) 110-121.

[8] J. Sladek, P.M. Blaszczyk, M. Kupiec, R. Sitnik, The hybrid contact-optical coordinate measuring system, Measurement, 44 (2011) 503-510.

[9] T. Várady, R.R. Martin, J. Cox, Reverse engineering of geometric models—an introduction, Computer-Aided Design, 29 (1997) 255-268.

[10] H. Zhao, Multisensor integration and discrete geometry processing for coordinate metrology, Thèse de doctorat, Ecole Normale Supérieure de Cachan 2010.

[11] A. Weckenmann, X. Jiang, K.D. Sommer, U. Neuschaefer-Rube, J. Seewig, L. Shaw, T. Estler, Multisensor data fusion in dimensional metrology, CIRP Annals - Manufacturing Technology, 58 (2009) 701-721.

[12] T.E. Ollison, J.M. Ulmer, R. McElroy, Coordinate measurement technology: a comparison of scanning versus touch trigger probe data capture, International Journal of Engineering Research & Innovation, 4 (2012).

[13] R. Edgeworth, R.G. Wilhelm, Uncertainty management for CMM probe sampling of complex surfaces, American Society of Mechanical Engineers, Manufacturing Engineering Division, MED, International Symposium on Information Storage and Processing Systems 1996, pp. 511-518.

[14] A. Weckenmann, H. Eitzert, M. Garmer, H. Weber, Functionality-oriented evaluation and sampling strategy in coordinate metrology, Precision Engineering, 17 (1995) 244-252.

[15] N. Vukašinović, D. Bračun, J. Možina, J. Duhovnik, The influence of incident angle, object colour and distance on CNC laser scanning, The International Journal of Advanced Manufacturing Technology, 50 (2010) 265-274.

[16] P.J. Besl, Active, optical range imaging sensors, Machine vision and applications, 1 (1988) 127-152.

[17] C. Mehdi-Souzani, C. Lartigue, Contactless laser plane sensor assessment: toward a quality measurement, Proceedings of IDMME-Virtual Concept, (2008).

[18] N.V. Gestel, S. Cuypers, P. Bleys, J.-P. Kruth, A performance evaluation test for laser line scanners on CMMs, Optics and Lasers in Engineering, 47 (2009) 336-342.

[19] Z. Ji, M. Leu, Design of optical triangulation devices, Optics & Laser Technology, 21 (1989) 339-341.

[20] C.P. Keferstein, M. Marxer, Testing bench for laser triangulation sensors, Sensor Review, 18 (1998) 183-187.

[21] R.A. Jarvis, A perspective on range finding techniques for computer vision, IEEE Transactions on Pattern Analysis and Machine Intelligence, PAMI-5 (1983) 122-139.

[22] R. Tsai, A versatile camera calibration technique for high-accuracy 3D machine vision metrology using off-the-shelf TV cameras and lenses, IEEE Journal of Robotics and Automation, 3 (1987) 323-344.

[23] F. Da, The grating projection three-dimensional precision measurement, Science Press 2011.

[24] J. Weng, P. Cohen, M. Herniou, Camera calibration with distortion models and accuracy evaluation, IEEE Transactions on Pattern Analysis and Machine Intelligence, 14 (1992) 965-980.

[25] Camera Calibration Toolbox for Matlab, http://www.vision.caltech.edu/bouguetj/calib_doc/

[26] Z. Zhang, A flexible new technique for camera calibration, IEEE Transactions on pattern analysis and machine intelligence, 22 (2000) 1330-1334.

[27] C. Che, J. Ni, A ball-target-based extrinsic calibration technique for high-accuracy 3-D metrology using off-the-shelf laser-stripe sensors, Precision Engineering, 24 (2000) 210-219.

[28] Z. Wei, G. Zhang, Y. Xu, Calibration approach for structured-light-stripe vision sensor based on the invariance of double cross-ratio, Optical Engineering, 42 (2003) 2956-2966.

[29] Nikon Metrology, (2014). Retrieved from http://www.nikonmetrology.com/.

[30] Laser Design, (2014). Retrieved from http://www.laserdesign.com/.

[31] FARO, (2014). Retrieved from http://www.faro.com/.

[32] F. Chen, G.M. Brown, M. Song, Overview of three-dimensional shape measurement using optical methods, Optical Engineering, 39 (2000) 10-22.

[33] W. Schreiber, G. Notni, Theory and arrangements of self-calibrating whole-body three-dimensional measurement systems using fringe projection technique, Optical Engineering, 39 (2000) 159-169.

[34] L. Salas, E. Luna, J. Salinas, V. Garcı´a, M. Servı´n, Profilometry by fringe projection, Optical Engineering, 42 (2003) 3307-3314.

[35] Q. Hu, P.S. Huang, Q. Fu, F.-P. Chiang, Calibration of a three-dimensional shape measurement system, Optical Engineering, 42 (2003) 487-493.

[36] R. Legarda-Sa´enz, T. Bothe, W.P. Ju¨ptner, Accurate procedure for the calibration of a structured light system, Optical Engineering, 43 (2004) 464-471.

[37] C.J. Tay, C. Quan, T. Wu, Y.H. Huang, Integrated method for 3-D rigid-body displacement measurement using fringe projection, Optical Engineering, 43 (2004) 1152-1159.

[38] T. Peng, S.K. Gupta, K. Lau, Algorithms for constructing 3-D point clouds using multiple digital fringe projection patterns, Computer-Aided Design and Applications, 2 (2005) 737-746.

[39] J. Pan, P.S. Huang, F.P. Chiang, Color-coded binary fringe projection technique for 3-D shape measurement, Optical Engineering, 44 (2005) 023606.

[40] H. Guo, H. He, Y. Yu, M. Chen, Least-squares calibration method for fringe projection profilometry, Optical Engineering, 44 (2005) 033603.

[41] S. Zhang, X. Li, S.-T. Yau, Multilevel quality-guided phase unwrapping algorithm for real-time three-dimensional shape reconstruction, Applied Optics, 46 (2007) 50-57.

[42] S. Zhang, S.-T. Yau, Generic nonsinusoidal phase error correction for three-dimensional shape measurement using a digital video projector, Applied Optics, 46 (2007) 36-43.

[43] K. Hibino, B.F. Oreb, D.I. Farrant, K.G. Larkin, Phase shifting for nonsinusoidal waveforms with phase-shift errors, The Journal of the Optical Society of America A 12 (1995) 761-768.

[44] B. Pan, K. Qian, L. Huang, A. Asundi, Phase error analysis and compensation for nonsinusoidal waveforms in phase-shifting digital fringe projection profilometry, Optics Letters, 34 (2009) 416-418.

[45] D. Malacara, Optical shop testing, John Wiley & Sons 2007.

[46] S. Zhang, S.-T. Yau, High-resolution, real-time 3D absolute coordinate measurement based on a phase-shifting method, Optics Express, 14 (2006) 2644-2649.

[47] P.S. Huang, S. Zhang, Fast three-step phase-shifting algorithm, Applied Optics, 45 (2006) 5086-5091.

[48] J. Schwider, R. Burow, K.-E. Elssner, J. Grzanna, R. Spolaczyk, K. Merkel, Digital wave-front measuring interferometry: some systematic error sources, Applied Optics, 22 (1983) 3421-3432.

[49] D.C. Ghiglia, M.D. Pritt, Two-dimensional phase unwrapping: theory, algorithms, and software, Wiley New York 1998.

[50] A.V. Fantin, A. Dal Pont, D.P. Willemann, A. Albertazzi, Comparison between temporal and spatial phase unwrapping for damage detection using shearography, Proceedings of SPIE, the International Society for Optical Engineering, Society of Photo-Optical Instrumentation Engineers 2006, pp. 634510.

[51] J.M. Huntley, H. Saldner, Temporal phase-unwrapping algorithm for automated interferogram analysis, Applied Optics, 32 (1993) 3047-3052.

[52] S. Gai, F. Da, H. Li, Fringe image processing based on structured light series, Proceedings of SPIE 2009, pp. 751334.

[53] G. Sansoni, M. Carocci, R. Rodella, Three-dimensional vision based on a combination of gray-code and phase-shift light projection: analysis and compensation of the systematic errors, Applied Optics, 38 (1999) 6565-6573.

[54] H.F. Durrant-Whyte, Sensor models and multisensor integration, International Journal of Robotics Research, 7 (1988) 97-113.

[55] M. Heizmann, F.P. Leo´n, Fusion of image signals, Fusion von Bildsignalen, 74 (2007) 130-138.

[56] M. Heizmann, F.P. Leo´n, Imaging and analysis of forensic striation marks, Optical Engineering, 42 (2003) 3423-3432.

[57] S. Karbacher, G. Haeusler, New approach for the modeling and smoothing of scattered 3D data, Photonics West'98 Electronic Imaging, International Society for Optics and Photonics 1998, pp. 168-177.

[58] I. Budak, J. Hodolic, M. Sokovic, Development of a programme system for data-point pre-processing in reverse engineering, Journal of Materials Processing Technology, 162 (2005) 730-735.

[59] K. Lee, H. Woo, T. Suk, Data reduction methods for reverse engineering, The International Journal of Advanced Manufacturing Technology, 17 (2001) 735-743.

[60] P.J. Besl, N.D. McKay, Method for registration of 3-D shapes, Robotics-DL tentative, International Society for Optics and Photonics 1992, pp. 586-606.

[61] W.D. Blair, T.R. Rice, B.S. McDole, E.M. Sproul, Least-squares approach to asynchronous data fusion, Aerospace Sensing, International Society for Optics and Photonics 1992, pp. 130-141.

[62] J. Tang, J. Gu, Z. Cai, Data fusion with different accuracy, IEEE International Conference on Robotics and Biomimetics IEEE 2004, pp. 811-815.

[63] R. Boudjemaa, A.B. Forbes, Parameter estimation methods for data fusion, National Physical Laboratory. Great Britain, Centre for Mathematics and Scientific Computing 2004.

[64] K.C. Chou, A.S. Willsky, A. Benveniste, Multiscale recursive estimation, data fusion, and regularization, IEEE Transactions on Automatic Control, 39 (1994) 464-478.

[65] Q. Gan, C.J. Harris, Comparison of two measurement fusion methods for Kalman-filter-based multisensor data fusion, IEEE Transactions on Aerospace and Electronic Systems, 37 (2001) 273-279.

[66] I. Gum, Guide to the expression of uncertainty in measurement, BIPM, IEC, IFCC, ISO, IUPAP, IUPAC, OIML, (1995).

[67] I. BIPM, I. IFCC, I. ISO, IUPAP and OIML,"Evaluation of Measurement Data–Supplement 1 to the 'Guide to the Expression of Uncertainty in Measurement'–Propagation of distributions using a Monte Carlo method", Joint Committee for Guides in Metrology, JCGM, 101 (2008).

[68] D.L. Hall, J. Llinas, An introduction to multisensor data fusion, Proceedings of the IEEE, 85 (1997) 6-23.

[69] I. Ashokaraj, A. Tsourdos, P. Silson, B.A. White, Sensor based robot localisation and navigation: using interval analysis and unscented Kalman filter, IEEE/RSJ International Conference on Intelligent Robots and Systems, IEEE 2004, pp. 7-12.

[70] S. Gundimada, V.K. Asari, N. Gudur, Face recognition in multi-sensor images based on a novel modular feature selection technique, Information Fusion, 11 (2010) 124-132.

[71] J. Demongeot, G. Virone, F. Duchêne, G. Benchetrit, T. Hervé, N. Noury, V. Rialle, Multi-sensors acquisition, data fusion, knowledge mining and alarm triggering in health smart homes for elderly people, Comptes Rendus Biologies, 325 (2002) 673-682.

[72] S. De, K. Gupta, R.J. Stanley, M.T. Ghasr, R. Zoughi, K. Doering, D.C. Van Aken, G. Steffes, M. O'Keefe, D.D. Palmer Jr, A comprehensive multi-modal NDE data fusion approach for failure assessment in aircraft lap-joint mimics, IEEE Transactions on Instrumentation and Measurement 62 (2013) 814-827.

[73] A.P. Mangan, R.T. Whitaker, Partitioning 3D surface meshes using watershed segmentation, IEEE Transactions on Visualization and Computer Graphics, 5 (1999) 308-321.

[74] J. Geisler, E. Peinsipp-Byma, M. Litfab, S. Angele, Smart recognition assistance for multi-sensor-image-based reconnaissance, Proceedings of the 6th Joint International Military Sensing Symposium MSS 2004.

[75] P. Baker, Y. Aloimonos, Complete calibration of a multi-camera network, IEEE Workshop on Omnidirectional Vision, IEEE 2000, pp. 134-141.

[76] J. Aguilar, M. Lope, F. Torres, A. Blesa, Development of a stereo vision system for non-contact railway concrete sleepers measurement based in holographic optical elements, Measurement, 38 (2005) 154-165.

[77] K.-D. Sommer, F. Puente León, Informationsfusion in der Mess-und Sensortechnik, TM-Technisches Messen, 74 (2007) 89-92.

[78] B.K. Horn, Obtaining shape from shading information, MIT press 1989.

[79] S. Soll, B. Roither, H. Moritz, H. Ernst, Three-dimensional surface test with" Shape-from-Shading", PHOTONIK-STUTTGART, 39 (2007) 20.

[80] S. Kammel, J. Horbach, Topography reconstruction of specular surfaces, Electronic Imaging 2005, International Society for Optics and Photonics 2005, pp. 59-66.

[81] X. Peng, Z. Zhang, H.J. Tiziani, 3-D imaging and modeling – Part I: acquisition and registration, Optik - International Journal for Light and Electron Optics, 113 (2002) 448-452.

[82] A. Weckenmann, W. Hartmann, J. Weickmann, Model and simulation of fringe projection measurements as part of an assistance system for multi-component fringe projection sensors, Optical Systems Design, International Society for Optics and Photonics 2008, pp. 71020N-71020N-71012.

[83] A. Weckenmann, K. Nalbantic, Precision measurement of cutting tools with two matched optical 3d-sensors, CIRP Annals-Manufacturing Technology, 52 (2003) 443-446.

[84] J.W. Tyrrell, C.D. Savio, R. Kruger-Sehm, H.-U. Danzebrink, Development of a combined interference microscope objective and scanning probe microscope, Review of scientific instruments, 75 (2004) 1120-1126.

[85] D.V. Sokolov, D.V. Kazantsev, J. Tyrell, T. Hasek, H.U. Danzebrink, Combined confocal and scanning probe sensor for nano-coordinate metrology, Nanoscale Calibration Standards and Methods, G. Wilkening, L. Koenders (eds.). Weinheim: WILEY-VCH, (2005) 131-143.

[86] C. Reich, R. Ritter, J. Thesing, 3-D shape measurement of complex objects by combining photogrammetry and fringe projection, Optical Engineering, 39 (2000) 224-231.

[87] R. Schmitt, T. Pfeifer, C. Mersmann, A. Orth, A method for the automated positioning and alignment of fibre-reinforced plastic structures based on machine vision, CIRP Annals-Manufacturing Technology, 57 (2008) 501-504.

[88] M. Nashman, B. Yoshimi, T.H. Hong, W.G. Rippey, M. Herman, A unique sensor fusion system for coordinate measuring machine tasks, Proceedings of SPIE International Symposium on Intelligent Systems and Advanced Manufacturing 1997.

[89] S. Motavalli, V. Suharitdamrong, A. Alrashdan, Design model generation for reverse engineering using multi-sensors, IIE Transactions, 30 (1998) 357-366.

[90] H. Chen, B. Wang, X. Luo, Z. Liu, J. Ding, J. Zhu, Multisensor integrated automated inspection system, Fifth International Symposium on Instrumentation and Control Technology, International Society for Optics and Photonics 2003, pp. 528-531.

[91] C. Bradley, V. Chan, A complementary sensor approach to reverse engineering, Journal of Manufacturing Science and Engineering, 123 (2001) 74-82.

[92] V. Chan, C. Bradley, G. Vickers, A multi-sensor approach for rapid digitization and data segmentation in reverse engineering, Journal of Manufacturing Science and Engineering, 122 (2000) 725-733.

[93] J. Jamshidi, G.W. Owen, A.R. Mileham, A new data fusion method for scanned models, Journal of Computing and Information Science in Engineering, 6 (2006) 340-348.

[94] Z. Xie, J. Wang, Q. Zhang, Complete 3D measurement in reverse engineering using a multi-probe system, International Journal of Machine Tools and Manufacture, 45 (2005) 1474-1486.

[95] H. Zhao, J.-P. Kruth, N.V. Gestel, B. Boeckmans, P. Bleys, Automated dimensional inspection planning using the combination of laser scanner and tactile probe, Measurement, 45 (2012) 1057-1066.

[96] Y. Huang, X. Qian, A dynamic sensing-and-modeling approach to three-dimensional point-and area-sensor integration, Transactions-American Society of Mechanical Engineers Journal of Manufacturing Science and Engineering, 129 (2007) 623.

[97] I. Bešić, N.V. Gestel, J.-P. Kruth, P. Bleys, J. Hodolič, Accuracy improvement of laser line scanning for feature measurements on CMM, Optics and Lasers in Engineering, 49 (2011) 1274-1280.

[98] W. ElMaraghy, C. Rolls, Design by quality product digitization, CIRP Annals-Manufacturing Technology, 50 (2001) 93-96.

[99] T.-S. Shen, C.-H. Menq, Automatic camera calibration for a multiple-sensor integrated coordinate measurement system, IEEE Transactions on Aerospace and Electronic Systems, 17 (2001) 502-507.

[100] S. Liu, K. Peng, X. Zhang, H. Zhang, F. Huang, The study of dual camera 3D coordinate vision measurement system using a special probe, Sixth International Symposium on Instrumentation and Control Technology: Signal Analysis, Measurement Theory, Photo-Electronic Technology, and Artificial Intelligence, International Society for Optics and Photonics 2006, pp. 63574H-63574H-63577.

[101] C. Heinzl, J. Kastner, E. Gröller, Surface extraction from multi-material components for metrology using dual energy CT, IEEE Transactions on Visualization and Computer Graphics, 13 (2007) 1520-1527.

[102] M. Bartscher, U. Hilpert, J. Goebbels, G. Weidemann, H. Puder, H.N. Jidav, Application of computed tomography (CT) in reverse-engineering technology, Einsatz von computer-tomographie in der Reverse-Engineering-Technologie, 48 (2006) 305-311.

[103] R. Christoph, H.J. Neumann, Multisensor coordinate Metrology: Measurement of form, size, and location in production and quality control, Verlag Moderne Industrie 2004.

[104] GOM, (2014). Retrieved from http://www.gom.com/.

[105] ZEISS, (2014). Retrieved from http://www.zeiss.com/.

[106] HEXAGON Metrology, (2014). Retrieved from http://www.optiv.net/.

[107] GFM, (2014). Retrieved from http://www.gfm3d.com/.

[108] Y. Huang, X. Qian, S. Chen, Multi-sensor calibration through iterative registration and fusion, Computer-Aided Design, 41 (2009) 240-255.

[109] G. Welch, G. Bishop, An introduction to the Kalman filter, 1995.

[110] S. Rusinkiewicz, M. Levoy, Efficient variants of the ICP algorithm, Third International Conference on 3-D Digital Imaging and Modeling, IEEE 2001, pp. 145-152.

[111] F. Boughorbel, A. Koschan, M. Abidi, Multi-sensor registration and integration for inspection and navigation, Tenth International Conference on Robotics & Remote Systems for Hazardous Environments 2004, pp. 102-106.

[112] T. Jin, J. Kuang, A 3-D point sets registration method in reverse engineering, Computers & Industrial Engineering, 53 (2007) 270-276.

[113] LMI, (2014). Retrieved from http://www.lmi3d.com/.

[114] R.W. Wedderburn, Quasi-likelihood functions, generalized linear models, and the Gauss—Newton method, Biometrika, 61 (1974) 439-447.

[115] C.M. Shakarji, Least-squares fitting algorithms of the NIST algorithm testing system, Journal of Research-National Institute of Standards and Technology, 103 (1998) 633-641.

[116] S. Motavalli, Review of reverse engineering approaches, Computers & Industrial Engineering, 35 (1998) 25-28.

[117] Geometrical Product Specifications (GPS)-Filtration, ISO 16610 Serire, 2010, (2010).

[118] G. Deng, L. Cahill, An adaptive Gaussian filter for noise reduction and edge detection, Nuclear Science Symposium and Medical Imaging Conference, IEEE 1993, pp. 1615-1619.

[119] J.-S. Lee, Digital image smoothing and the sigma filter, Computer Vision, Graphics, and Image Processing, 24 (1983) 255-269.

[120] H. Hwang, R.A. Haddad, Adaptive median filters: new algorithms and results, IEEE Transactions on Image Processing, 4 (1995) 499-502.

[121] T. Jin, S. Tong, Reverse engineering technology, China Machine Press 2003.

[122] R. Martin, I. Stroud, A. Marshall, Data reduction for reverse engineering, RECCAD, Deliverable Document 1 COPERNICUS project, No 1068, (1997) 111.

[123] B. Hamann, A data reduction scheme for triangulated surfaces, Computer Aided Geometric Design, 11 (1994) 197-214.

[124] D.F. Huber, M. Hebert, Fully automatic registration of multiple 3D data sets, Image and Vision Computing, 21 (2003) 637-650.

[125] A. Almhdie, C. Léger, M. Deriche, R. Lédée, 3D registration using a new implementation of the ICP algorithm based on a comprehensive lookup matrix: Application to medical imaging, Pattern Recognition Letters, 28 (2007) 1523-1533.

[126] F. Boughorbel, M. Mercimek, A. Koschan, M. Abidi, A new method for the registration of three-dimensional point-sets: The Gaussian Fields framework, Image and Vision Computing, 28 (2010) 124-137.

[127] S.J. Ahn, W. Rauh, M. Recknagel, Ellipse fitting and parameter assessment of circular object targets for robot vision, IEEE/RSJ International Conference on Intelligent Robots and Systems, IEEE 1999, pp. 525-530.

[128] M. Franaszek, G.S. Cheok, C. Witzgall, Fast automatic registration of range images from 3D imaging systems using sphere targets, Automation in Construction, 18 (2009) 265-274.

[129] L. Li, N. Schemenauer, X. Peng, Y. Zeng, P. Gu, A reverse engineering system for rapid manufacturing of complex objects, Robotics and Computer-Integrated Manufacturing, 18 (2002) 53-67.

[130] S. Larsson, J.A.P. Kjellander, Motion control and data capturing for laser scanning with an industrial robot, Robotics and Autonomous Systems, 54 (2006) 453-460.

[131] Ø. Hjelle, M. Dæhlen, Triangulations and applications, Springer 2006.

[132] H. Xie, K.T. McDonnell, H. Qin, Surface reconstruction of noisy and defective data sets, Visualization, IEEE 2004, pp. 259-266.

[133] T.K. Dey, S. Goswami, Provable surface reconstruction from noisy samples, Computational Geometry, 35 (2006) 124-141.

[134] P. Alliez, D. Cohen-Steiner, Y. Tong, M. Desbrun, Voronoi-based variational reconstruction of unoriented point sets, Symposium on Geometry Processing 2007, pp. 39-48.

[135] M. Vančo, B. Hamann, G. Brunnett, Surface reconstruction from unorganized point data with quadrics, Computer Graphics Forum, Wiley Online Library 2008, pp. 1593-1606.

[136] P. Stelldinger, L. Tcherniavski, Provably correct reconstruction of surfaces from sparse noisy samples, Pattern Recognition, 42 (2009) 1650-1659.

[137] A. Shamir, A survey on mesh segmentation techniques, Computer Graphics Forum, Wiley Online Library 2008, pp. 1539-1556.

[138] H. Woo, E. Kang, S. Wang, K.H. Lee, A new segmentation method for point cloud data, International Journal of Machine Tools and Manufacture, 42 (2002) 167-178.

[139] M. Yang, E. Lee, Segmentation of measured point data using a parametric quadric surface approximation, Computer-Aided Design, 31 (1999) 449-457.

[140] J. Huang, C.-H. Menq, Automatic data segmentation for geometric feature extraction from unorganized 3-D coordinate points, IEEE Transactions on Aerospace and Electronic Systems, 17 (2001) 268-279.

[141] P. Benkő, T. Várady, Segmentation methods for smooth point regions of conventional engineering objects, Computer-Aided Design, 36 (2004) 511-523.

[142] K. Demarsin, D. Vanderstraeten, T. Volodine, D. Roose, Detection of closed sharp edges in point clouds using normal estimation and graph theory, Computer-Aided Design, 39 (2007) 276-283.

[143] P.J. Besl, R.C. Jain, Segmentation through variable-order surface fitting, IEEE Transactions on Aerospace and Electronic Systems, 10 (1988) 167-192.

[144] C. Chappuis, A. Rassineux, P. Breitkopf, P. Villon, Improving surface meshing from discrete data by feature recognition, Engineering with Computers, 20 (2004) 202-209.

[145] T. Rabbani, F. van Den Heuvel, G. Vosselmann, Segmentation of point clouds using smoothness constraint, International Archives of Photogrammetry, Remote Sensing and Spatial Information Sciences, 36 (2006) 248-253.

[146] A. Alrashdan, S. Motavalli, B. Fallahi, Automatic segmentation of digitized data for reverse engineering applications, IIE Transactions, 32 (2000) 59-69.

[147] Y. Liu, Y. Xiong, Automatic segmentation of unorganized noisy point clouds based on the Gaussian map, Computer-Aided Design, 40 (2008) 576-594.

[148] R. Bénière, G. Subsol, G. Gesquière, F. Le Breton, W. Puech, A comprehensive process of reverse engineering from 3D meshes to CAD models, Computer-Aided Design, 45 (2013) 1382-1393.

[149] P.N. Chivate, A.G. Jablokow, Review of surface representations and fitting for reverse engineering, Computer Integrated Manufacturing Systems, 8 (1995) 193-204.

[150] E. Boender, A survey of intersection algorithms for curved surfaces, Computers & Graphics, 15 (1991) 109-115.

[151] J.D. Foley, A. Van Dam, S.K. Feiner, J.F. Hughes, Computer graphics: Principles and practice, Addison-Wesley Professional 1996.

[152] R. Franke, Scattered data interpolation: tests of some methods, Mathematics of Computation, 38 (1982) 181-200.

[153] A.B. Forbes, Least-squares best-fit geometric elements, National Physical Laboratory Teddington 1989.

[154] N.M. Aziz, R. Bata, S. Bhat, Bezier surface/surface intersection, Computer Graphics and Applications, IEEE, 10 (1990) 50-58.

[155] W.J. Gordon, R.F. Riesenfeld, B-spline curves and surfaces, Computer Aided Geometric Design, (1974) 95-126.

[156] D.F. Rogers, J.A. Adams, Mathematical elements for computer graphics, McGraw-Hill Higher Education 1989.

[157] W. Tiller, Rational B-Splines for Curve and Surface Representation, IEEE Computer Graphics and Applications 1983, pp. 61-69.

[158] L. Piegl, On NURBS: a survey, IEEE Computer Graphics and Applications, 11 (1991) 55-71.

[159] N.V. Puntambekar, A.G. Jablokow, Constrained reconstruction of parametric surfaces for reverse engineering, The 1994 ASME Design Technical Conferences. Part 1(of 2)1994, pp. 315-322.

[160] P. Benkő, R.R. Martin, T. Várady, Algorithms for reverse engineering boundary representation models, Computer-Aided Design, 33 (2001) 839-851.

[161] G. Kós, R.R. Martin, T. Várady, Methods to recover constant radius rolling ball blends in reverse engineering, Computer Aided Geometric Design, 17 (2000) 127-160.

[162] F. Langbein, B.I. Mills, A.D. Marshall, R.R. Martin, Finding approximate shape regularities in reverse engineered solid models bounded by simple surfaces, The Sixth ACM Symposium on Solid Modeling and Applications, ACM 2001, pp. 206-215.

[163] G. Lukács, R.R. Martin, D. Marshall, Faithful least-squares fitting of spheres, cylinders, cones and tori for reliable segmentation, Computer Vision—ECCV'98, Springer 1998, pp. 671-686.

[164] D. OuYang, H.-Y. Feng, On the normal vector estimation for point cloud data from smooth surfaces, Computer-Aided Design, 37 (2005) 1071-1079.

[165] D. Hakala, R. Hillyard, P. Malraison, B. Nource, Natural quadrics in mechanical design, Proc-AUTOFACT West, 1 (1981) 17-20.

[166] J.R. Miller, Analysis of quadric-surface-based solid models, Computer Graphics and Applications, IEEE, 8 (1988) 28-42.

[167] M.E. Mortenson, Geometric modeling, Industrial Press 2006.

[168] RENISHAW, (2014). Retrieved from http://www.renishaw.com/.

[169] A. Contri, P. Bourdet, C. Lartigue, Quality of 3D digitised points obtained with non-contact optical sensors, CIRP Annals-Manufacturing Technology, 51 (2002) 443-446.

[170] T.R. Kurfess, D.L. Banks, Statistical verification of conformance to geometric tolerance, Computer-Aided Design, 27 (1995) 353-361.

[171] F. Li, A.P. Longstaff, S. Fletcher, A. Myers, A practical coordinate unification method for integrated tactile–optical measuring system, Optics and Lasers in Engineering, 55 (2014) 189-196.

[172] F. Li, A.P. Longstaff, S. Fletcher, A. Myers, Rapid and accurate reverse engineering of geometry based on a multi-sensor system, The International Journal of Advanced Manufacturing Technology, 74 (2014) 369-382.